Binder jetting: a microstructural perspective

Sergi Bafaluy Ojea

Tesis depositada en cumplimiento parcial de los requisitos para el grado de Doctor en:

Ciencia e ingeniería de los materiales

Universidad Carlos III de Madrid

Directores:

María Teresa Pérez Prado

Federico Sket

Directora industrial:

Rocío Muñoz Moreno

Tutor:

José Manuel Torralba

Setiembre 2023

To Antonio,

you were nothing but care and love.

Acknowledgements

I would like to thank my supervisors, Rocío Muñoz, her guidance, implication, and contributions to this project were key since the very first week. Many thanks to María Teresa Pérez, her positivity and interest made a huge difference. Last, but not least, my supervisor, Federico Sket, to whom I owe most of the things I have learnt during these three years.

I am grateful to the HP Metal R&D team, from Barcelona and Corvallis, it has been a pleasure to work with you. A special thanks to Ariadna Marin who dedicated a lot of time and passion to this project and to Vladek Kasperchik for his contributions. I would also like to mention Vanesa Fal and Trini Carrasco, both were truly understanding and helpful.

I would like to thank IMDEA colleagues and staff, each one of them provided a meaningful piece to complete this puzzle. A warm thank you to the HP technicians, Miren, Eric, Camilo, Alicia, and Sergi R., who did not only provide their help in the course of this work but also offered me their friendship.

To my parents, Maria José and Pepe, who supported me through every decision, gave me valuable advises, and encouraged me by expressing their pride. Also, to my uncles, Jaime and Belen, they showed me a whole new world filled with curiosity and sensitivity.

I would like to acknowledge my closest friends Marta, Karen, Noe, Irene, Lourdes, Pol, Gerardo, Mónica, Nacho and Javi, the time shared with you has been irreplaceable.

Finally, I would also like to express my deepest gratitude and love to Olga, your empathy, support, and affection have been an endless source of joy throughout these years.

Published and submitted contents

The following scientific publication has been included and extended in the present thesis in **Chapters 2, 4** and **Chapter 5**.

- Sergi Bafaluy Ojea, Jordina Torrents-Barrena, María Teresa Pérez-Prado, Rocío Muñoz Moreno, Federico Sket, "Binder jet green parts microstructure: advanced quantitative analysis", *Journal of Materials Research and Technology*, 2023, vol 23, 3974-3986, doi: https://doi.org/10.1016/j.jmrt.2023.02.051.

Table of contents

List of figures

List of tables

Abbreviations

AM	Additive Manufacturing
ASME	American Society of Mechanical Engineers
ASTM	American Society for Testing and Materials
BJ	Binder Jetting
BSE	Backscattered Electron
CAD	Computer Aided Design
CIJ	Continuous Ink Jetting
CSI	Coherence Scanning Interferometry
DED	Directed Energy Deposition
DM	Digital Metal
DOD	Drop On Demand
DS	Double Smoothing
EBM	Electron Beam Milling
FD	Fourier Descriptor
FEG-SEM	Field Emission Gun Scanning Electron Microscope
FFT	Fast Fourier Transform
FIB	Focused Ion Beam
GA	Gas Atomized
GE	General Electric
HIP	Hot Isostatic Pressing
HP	Hewlett and Packard
IMDEA	Instituto Madrileño De Estudios Avanzados
IMTS	International Manufacturing Technology Show
L-PBF	Laser Powder Bed Fusion

MIM	Metal Injection Molding
MIT	Massachusetts Institute of Technology
MPIF	Metal Powder Industries Federation
PCA	Principal Component Analysis
PM	Powder Metallurgy
PR	Packing Ratio
PSD	Particle Size Distribution
ROI	Region Of Interest
SD	Standard Deviation
SEM	Scanning Electron Microscopy
SFF	Solid Free-form Fabrication
SLM	Selective Laser Melting
SLS	Selective Laser Sintering
SPJ	Single Pass Jetting
SS	Stainless-Steel
TGA	Thermogravimetric analysis
TIJ	Thermal Inkjet
TRS	Transverse Rupture Strength
US	United States
UTS	Ultimate Tensile Strength
WA	Water Atomized

1
INTRODUCTION

Additive manufacturing (AM) technologies stand out by their ability to produce complex and customized geometries compared to traditional processes. The knowledge transfer from fields like powder metallurgy, welding, topography, or prototyping has facilitated the spread of AM metals in the medical, aerospace, energy, and automotive industries and into consumer goods [1], [2]. Nowadays, there is a wide range of AM techniques available for the manufacturing of metal parts. Laser or electron beam-based techniques such as Selective Laser Melting (SLM), Selective Laser Sintering (SLS) or Electron Beam Melting (EBM) demand very high energies during processing, leading to a complex thermal history in the part and therefore, to a very heterogeneous and anisotropic microstructure. For that reason, these techniques usually require post-processing or development of new alloys to reach improved final material properties, i.e., more homogeneous, isotropic and dense parts [3]–[5].

Binder jetting (BJ) raises as an alternative which allows the use of commercial metal alloys such as stainless steel, copper or traditional aluminum alloys. BJ added value in comparison to traditional Metal Injection Molding (MIM), is that it does not need molds for production, which becomes expensive when several geometries must be manufactured, and that it requires a significant less binder, which derives in minimum debinding times [6], [7].

BJ was firstly developed by Massachusetts Institute of Technology (MIT) researchers in the early 1990s [8]. Posteriorly, ExOne, Digital Metal, Desktop Metal and HP found an opportunity in this AM process to lead the 4th industrial revolution thanks to its characteristic high productivity and part quality. Therefore, current BJ objective is to disrupt the manufacturing [9]. This technique consists in successively jetting binder droplets on previously spread layers of powder (metal or ceramic) to consolidate a part. After printing, the binder is cured to strengthen the green parts, thus making possible to

handle them. Once cured, the printed parts are extracted from the loose powder, which can be reused, and they are finally post-processed through a sintering step in which the binder is burned out and the part is consolidated [6].

BJ challenges are related to a balance between the part quality and productivity rates. Highest qualities use to imply larger manufacturing times, while medium qualities would allow fastest rates. When in high-speed scenarios, medium parts density could give rise to more limited mechanical and dimensional properties, which would require focused investigation to enhance better balances. Sintered and green parts density are influenced by powder properties, as powder chemical composition, particle size distribution, powder morphology, powder internal porosity or powder flowability, among others. In addition, printing parameters, as layer thickness, spreading speed, printing temperature or contone level, together with depowdering, curing, debinding and sintering process steps impact on final part quality and price

In September 2018, HP published a new BJ technology named Metal Jet [10]. The mission was and is to disrupt the metal manufacturing to enable BJ production mass, by an automatic and digital process, with higher print speeds and the ability to process commercial metals. During the following 4 years, a beta program of prototype to product development, in close collaboration with industrial partners as GKN, was developed to finally, in September 2022, launch the HP BJ product: Metal Jet S100. This thesis has been performed with the beta test printer in collaboration between HP Printing and Computing Solutions SL. and IMDEA Materials Institute. The objective of the present work is to analyze with advanced techniques the green parts microstructures and allow sinter part properties prediction for stainless-steel parts with the HP Metal Jet printing process. For that purpose, the comprehension of fundamental mechanisms behind BJ is performed, together with the aim to develop more optimized print modes and adapted to a wide range of application requirements. Within the industrial context of this work, the request for automated, fast and reliable characterization methods has been the driver.

2 LITERATURE REVIEW

Binder jetting has been available already for three decades, but it has not been until now, after the expiration of its patent in 2018, that the interest on this technology has begun to rise, directly impacting the knowledge on the topic. This chapter comments on the current state of the technology, compares it to other additive manufacturing techniques and discusses its current challenges by addressing all the influential factors of BJ, including raw material, sub-processes and resulting properties and microstructures. A section concerning the usage of X-Ray Computed Tomography (XCT) on additive manufacturing (AM) is included given its importance in the frame of this work.

2.1 Metal additive manufacturing

Additive manufacturing is defined as a process by which a part is built through the deposition of material layer by layer. A computer aided design (CAD) of the part that will be produced is required. The 3D design will be transformed into a triangle mesh, normally a .stl file that can be processed by the printer or equipment. The range of available technologies for metal AM has rapidly increased in the last decade. Among them, Laser-Powder Bed Fusion (L-PBF), Directed Energy Deposition (DED), and Binder Jetting (BJ) have received a significantly higher attention in the scientific community and currently have a larger presence in a variety of industrial sectors. However, each of these techniques

is better suited for different applications. A diagram summarizing the three processes mentioned above is shown in **Figure 2.1**.

L-PBF is an AM process by which a metal powder layer is spread using a recoating system, generally consisting either on a blade or a roller. Next, a laser is employed to melt and consolidate the particles together within each spread layer. Once solidification has occurred, a new layer is built on top of the previous one. The repetition of this process will form a whole part. The main disadvantage of this technology is the elevated thermal gradient originated upon powder bed lasing. Such thermal gradient limits the printability of high melting point materials. Furthermore, the resulting microstructure will likely present a high degree of anisotropy and residual stresses, and thus, final parts employed for demanding applications will generally require additional heat treatments and/or post-processing to enhance their final properties [11]. The critical parameters in L-PBF include the spreading process (layer thickness) and the energy deposition (hatch distance, laser power, scanning speed). However, a focus on the scanning strategy has gained importance over the past years thanks to its ability to tune the material microstructure [12].

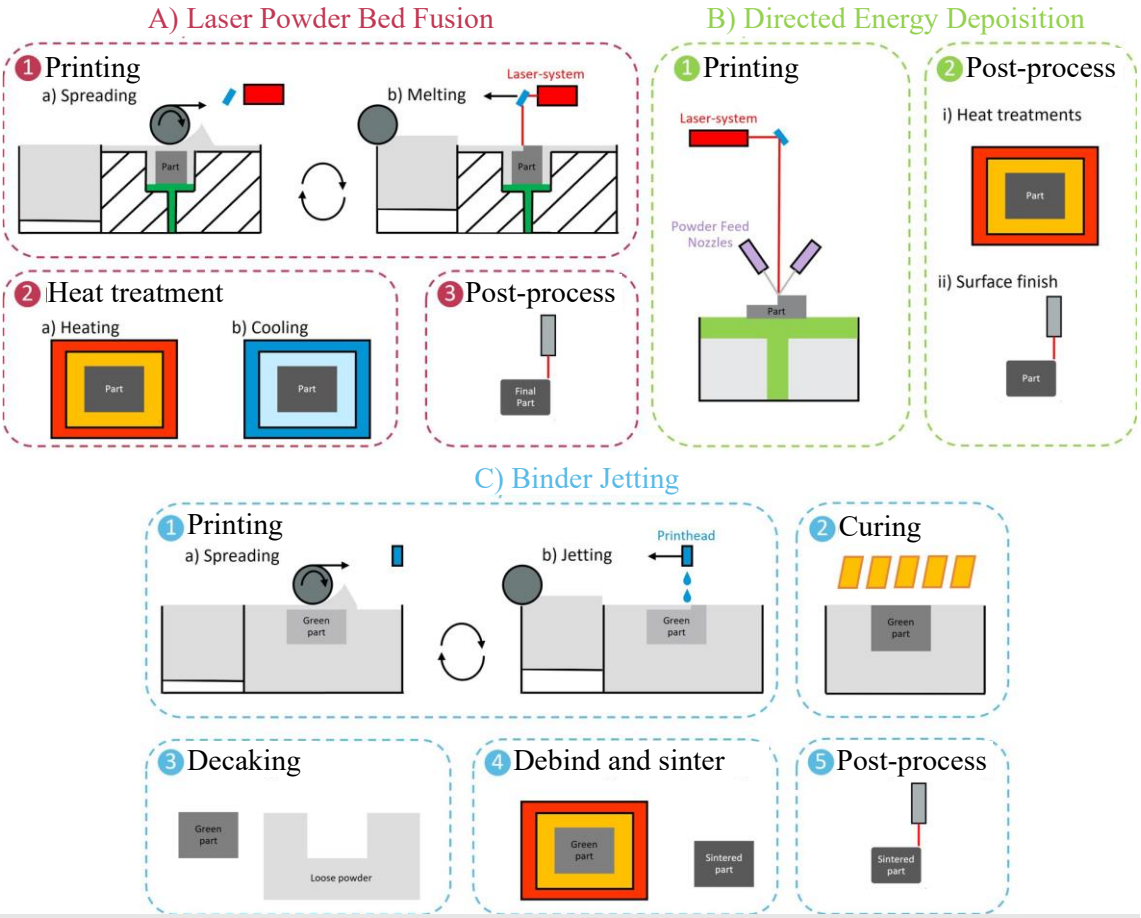

***Figure 2.1**: Process diagram for AM technologies: a) L-PBF: b) DED; c) BJ.*

In DED technologies, the material is melted while it is being fed. The molten pool is then cooled and solidified and thus, by repetition, a part is created. This process generally involves an energy beam (laser, electron beam or electric arc) aligned with a powder or wire feed. DED can reach a higher production rate than LPBF processes. However, the achievable feature size, layer thickness and surface roughness are larger [13], [14]. As-printed parts show a high level of anisotropy and low dimensional accuracy related to high energy gradients, which is the reason why post-processing techniques like

hot isostatic pressing (HIP), or surface finishing are usually required [15]. One of the benefits of DED is its capability to print multi-material parts thanks to the availability of multiple feeding systems. The main process parameters in DED processes are those controlling the energy dosage (power, scan speed), the powder feeding (feed rate, thickness), material and stage/part motion [15].

In BJ, the powder layer can be spread similarly to L-PBF, but the particles are, instead, bonded through a binder jetted by a printhead. This gives the part enough strength to be extracted from the powder bed. Then, additional curing, debinding and sintering steps are usually performed in order to obtain a final part with a competitive density and robust mechanical properties. A final increase of the sintered density can be achieved through HIP. Another post-processing alternative is metal infiltration, where a low melting point metal is employed to fill the pores present on the green part [16]. While BJ allows a higher printing rate than the other technologies, the need for post-processing can increase process time considerably [6]. Also, due to the low relative density achieved during printing (50-60 %), the sintering process will produce a shrinkage on the final part that needs to be considered in the design stage [17]. This is generally done by simulating the expected shrinkage and developing print modes through reverse engineering. The main parameters explored in BJ include the layer spreading process (roller/blade speed, layer thickness, etc.) and the binder deposition (binder saturation, binder deposition strategy, etc.). The powder bed target temperature employed during printing is also studied since it may interfere on the infiltration kinetics of the binder [18]. **Table 2.1** summarizes the main advantages and drawbacks of the discussed AM technologies.

***Table 2.1**: Advantages and disadvantages of AM technologies.*

Technology	Advantages	Disadvantages
L-PBF	Complex geometries	Alloy design expensive materials
	No support needed	Post densification processes
	Good surface finish	Multi-material
DED	Fully dense parts	Low resolution
	Control over microstructure	Slow process
	Multi-material	Distortions and inhomogeneities
BJ	Fast print rate	Need for post-processing
	Commercial alloys	Dimensional control
	Complex and small size parts	Green part control

2.2 Binder jetting

BJ, originally referred to as 3DP, was invented in 1993 by Sachs and collaborators in the Massachusetts Institute of Technology (MIT) [8]. It is defined within the ASTM F2792 standard as “an AM process in which a liquid bonding agent is selectively deposited to join powder materials” [19]. In the first step of the process, a layer of powder is spread. The powder can be supplied from a feeding platform or through a metering device (hopper). A roller or a blade is generally employed to flatten the layer surface. The

spreading process can be defined by the employed speed and the chosen layer thickness. The balanced speed is limited by the ability to spread a homogeneous layer.

The binder is then supplied in the form of droplets by a printhead furnished with several nozzles. There exist two mechanisms for the generation of droplets. In continuous inkjet jetting (CIJ) a vibration is created through a piezoelectric material which breaks the polymer solution into droplets. The control of the jet is done by selecting the jetted droplets that will be deposited on the layer with an external deflection mechanism [20]. Alternatively, in the drop-on-demand (DOD) technology a pressure pulse is originated on the printhead, causing a single droplet to be jetted. Hence, the control of deposition will depend on the ability to generate fast and stable pulses. The issued pulse can be initiated by a thermal signal or by an electric one, in the so-called thermal (TIJ) and piezoelectric printheads, respectively [21]. Piezoelectric printheads are considered more precise since they allow the formation of drops as small as 1.5 picolitres. Also, the polymer systems employed are not limited by the need of high temperatures, as in thermal printheads. However, piezoelectric printheads are more expensive and larger than thermal printers. In addition, TIJ printheads are cheaper and more flexible to changes and replacements. **Figure 2.2** presents a schematic view of the two types of DOD printhead systems with an example of their specifications.

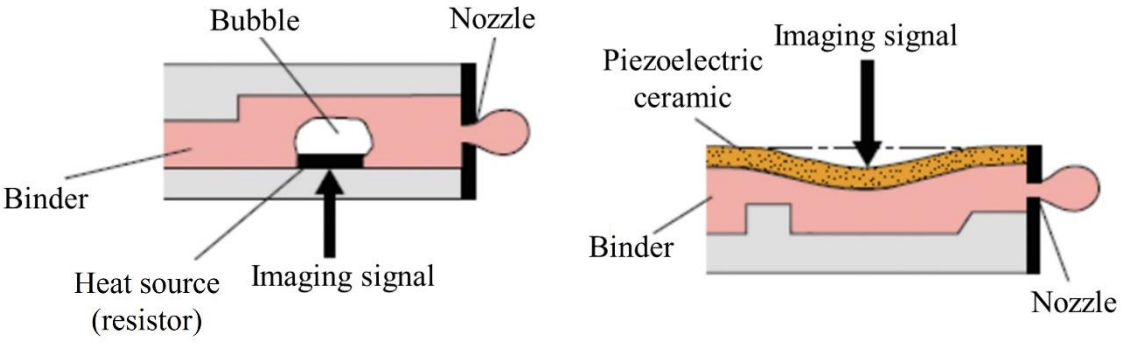

***Figure 2.2**: Schematic view of: a) Thermal printhead; b) Piezoelectric printhead* [21].

During printing, several subsystems can be used to increase the process control during printing. This will be discussed in more detail in the **Section 2.2.2**. However, a commonly built-in system is the thermal delivery. Mostly, the deposited binder is in liquid state to allow infiltration. Posteriorly, printing temperatures makes the binder more viscose and less movable, distributing homogenously layer by layer. Binder partial evaporation of solvents during printing is expected and strengthening happens during curing. For this reason, most BJ solutions include a thermal system consisting on several lamps and thermocouples positioned along the printing chamber. Curing can happen both

in the printer or in a furnace. Finally, binder burn out and parts densification occurs through debinding and sintering, respectively.

2.2.1 Materials

The feedstock of BJ consists of the atomized metal powder and the binder or polymer solution. Due to the similar nature between this process and MIM, many of the materials employed could be adopted from this technology.

BJ is widely employed for ceramic and metals, but printer solutions are often directed to either one or the other material family. Metal BJ's most common materials include stainless steels 316L, 17-4PH and 420. These materials were initially prioritized due to their market request and versatility. Later on, added value materials such as Ti6Al4V were introduced to enlarge the scope of lightweight and biomedical applications. More recently, precious metal like gold or silver have been also added, including the jewelry and consumer goods market in the BJ portfolio. The following table covers the main printer manufacturers and the materials certified for their printers (**Table 2.2**)) [22].

***Table 2.2**: Supported metal powders for BJ 3D printing.*

Company	Metals
Digital Metal	SS 316L, SS 17-4PH, Ti6Al4V, DM 625, DM 247, DM Cu
Desktop Metal (including former ExOne)	SS 316L, SS 304L, SS 17-4PH, SS420, steels 4140, 4340, 440C, 4605, A2, D2 and H13 tool steel, Al 6061, bronze, cobalt chrome, copper, gold, silver, Inconel 625, Inconel 718, etc.
HP[1]	SS 316L, SS 17–4PH
Sinterjet	SS 316L. CoCrMo, CoNi
GE[2]	SS 316L, SS 304L, SS 17-4PH, SS 441, copper C18000, tungsten carbide

[1] HP Printing and Computing Solutions S.L.
[2] General Electric Additive, not commercially available yet.

The binder formulations have a large number of requisites to properly function in BJ technology. First, binders´ viscosity needs to be low to allow it to flow in small quantities through the printhead nozzles. Additionally, it also has to be stable at operating temperatures to avoid nozzle clogging issues. Finally, after printing, viscosity has to evolve fast enough to avoid part distortion during printing, but slow enough to ensure that a correct amount of infiltration occurs [23]. For this reason, the employed binder formulations are generally very complex and need to be tailored to each technology.

The formulation constituents can be split into three classes, namely binder, solvents and additives. The binder is commonly a polymer that crosslinks adhering metal

particles together. Some examples of common binders are butyral resins, polyvinyls, polysiloxanes, polyacrylic acids, starch, dextran, maltodexterins and latex [24]. The solvents need to be low evaporation point liquids that can be easily removed during printing and curing. A common solvent employed in many binder formulations is water. The additives can be included to the formulation for many reasons. For instance, they can be employed to improve the binders' viscosity or to enhance diffusion during sintering, as boron nitrides or boron carbides [25].

Currently, the addition of metal nanoparticles to the binder formulation has gained a lot of interest as this solution has the potential to enhance diffusion processes during sintering and to increase the final sintering density [26], [27].

2.2.2 Technologies and products

BJ was initially adopted in the industry by Extrude Hone Corporation owing to the obtention of a license from the MIT, who patented the technology in 1993. Later on, in 2005, ExOne, a spinoff from Extrude Hone Corporation, was the only available printer maker in the BJ market [27]. The patent did not expire until 2018, a time when several companies developed their own solutions, expanding the market for this technology. The **Table 2.3** summarizes the current main BJ printer developer companies and their solutions.

***Table 2.3**: BJ technology providers.*

Company	Solution	Build volume (mm)	Resolution (dpi)
Digital Metal	P2500	250 x 217 x 70/186	725
	DM/Pro Series	250 x 217 x 70/186	725
Desktop Metal	X160Pro	800 x 500 x 400	1200
	P50	490 x 380 x 260	1200
HP[1]	Metal Jet S100	430 x 309 x 140	1200
Voxeljet	VX1000	1000 x 600 x 500	600
	VX200	300 x 200 x150	254
Sinterjet	M60	160 x 60 x 60	1200
GE[2]	BJ Line Series 3	500 x 500 x 500	600/900
XYZPrinting	PartPro 350 xBC	225 x 350 x 200	1600

[1] HP Printing and Computing Solutions S.L.
[2] General Electric Additive, not commercially available yet.

Many subsystems that have been developed or modified to address some of the biggest challenges of BJ. Concerning the spreading process, high-technology rollers and blades have been developed to add vibrations and heat during the process. This allows for a more uniform powder distribution across the layer and a higher compaction. As an example, in 2021 Desktop Metal patented a method to employ the roller after spreading to further compact the powder bed and to thus increase the resulting density of the green parts [28].

Using the very same patent, Desktop Metal also introduced Single Pass Jetting (SPJ). This technology consists of a combination of subsystems integrated on the printer carriage that work simultaneously to deliver the powder, spread the layer and print within a single carriage pass, thus reducing the layer formation time to just 3 s. However, it may

limit the control over some relevant parameters. As an example, a common strategy when jetting the binder is to increase the number of passes in order to reduce the distortion that it may cause to the powder layer. By delivering all the binder in a single pass, the quantity and the weight of the droplets may significantly alter the uniformity of the layer. In order to reduce this effect, an additional subsystem was added [29]. The technology consists on a delivery of a vapor phase, prior to printing, that prevents the spread particles from moving during the binder deposition phase. It claims to reduce particle ejection and thus, layered porosity and printhead clogging.

BJ printing accuracy and achievable resolution depends mainly on the ability to deliver the binder with small and localized droplets. To this regard, HP provided their well-known knowledge on TIJ printheads architecture design, leveraged from years of work in the 2D printing industry, to the current need in BJ.

Another common challenge of BJ printer manufacturers has been the shrinkage produced during sintering. This limited the achievable dimensional accuracy of printed parts and, thus, applications demanding high tolerances could not be covered or required certain post-processing. To this regard, several manufacturers have developed their own software solutions to predict the dimensions reduction that will take place during final densification (GE Additive, Desktop Metal, HP, etc.). In general, the software would compensate the original CAD design based on these predictions, increasing significantly the resulting dimensional accuracy [30]–[32].

Recent advances in metal BJ technology are exemplified by the latest solution from HP. This solution includes several modular stations that cover the entire green part manufacturing process, from a powder management station to an automatic depowdering module. By integrating the various stages of the manufacturing process, these systems reduce the gap between AM and serial production, enabling the production of high-quality metal parts at scale [33].

2.2.3 Applications

The ability of BJ to produce parts with a wide range of relative densities, its design freedom, productivity and quality, makes it applicable to many industrial sectors. Its customization capabilities have attracted significant interest in the medical field, particularly for applications such as dental frameworks or implants (**Figure 2.3a)** [34].

BJ is capable of producing parts that meet the requirements of demanding applications, such as tooling, which require a good balance between light weight and robust mechanical properties (**Figure 2.3b**). However, the high specifications of this sector can sometimes limit BJ applications to prototyping or necessitate further post-processing to achieve the desired properties [35]. BJ finds additional use in a variety of fields, including electronics (for producing capacitors, piezoelectric devices, etc.), mold fabrication, and drug delivery [6].

A good example of the extent to which BJ allows for geometric freedom and complexity is the recent application by Schneider Electric and HP Metal Jet S100 depicted in **Figure 2.3c** It consists of a circuit breaker with a complex molecular lattice structure that provides the desired level of heat transfer. To conclude, the addition of new materials

has also widened the applications of BJ, reaching amongst others the luxury goods sector. **Figure 2.3d** illustrates a gold-plated stainless-steel jewel.

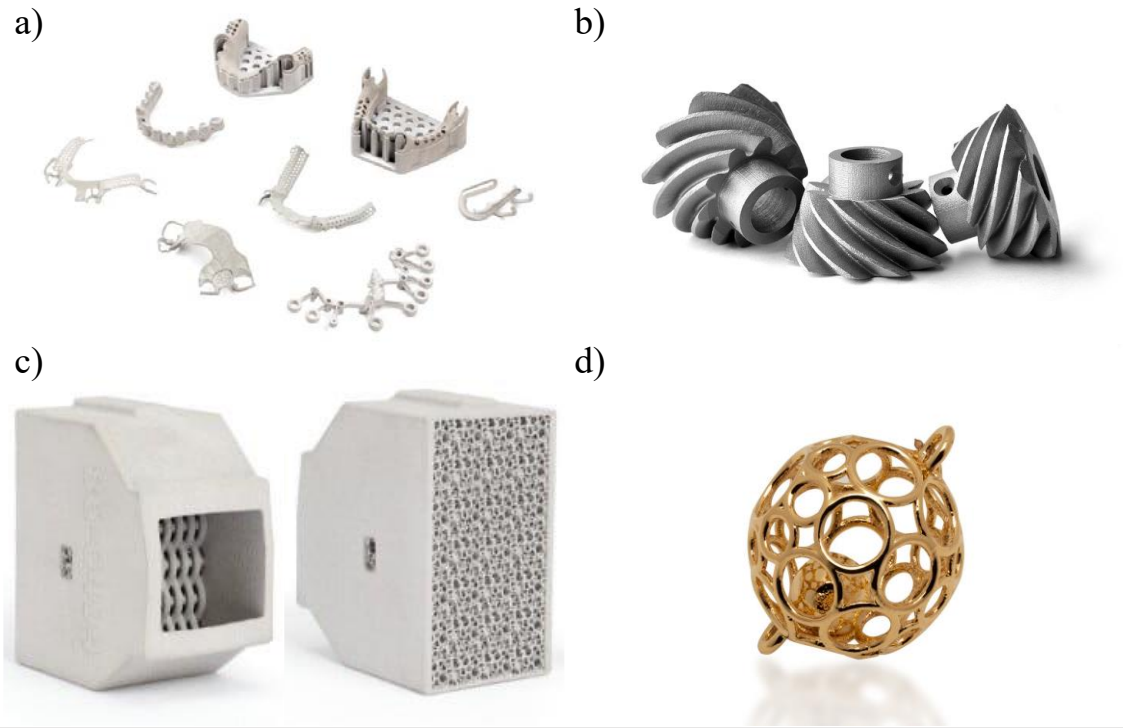

Figure 2.3*: BJ printing applications: a) dental prothesis* [36]*; b) turbines* [37]*; c) circuit breaker of 690 V* [38]*; d) jewelry* [39].

2.3 Raw material

The raw material employed for BJ generally consists of the binder and the metal powder with a wide range of particle sizes. For particle sizes smaller than 10 μm, and generally for ceramics, the slurry-based deposition method is required to improve powder flowability given the high cohesivity between particles. This procedure is common for other AM processes as well, e.g., SLM [40].

Powder properties critically influence the printing and sintering processes, and they will impact the quality of the produced part. In their work, Spiering et al. presented an Ishikawa diagram that summarizes the powder characteristics that must be evaluated for AM (**Figure 2.4**) [41].

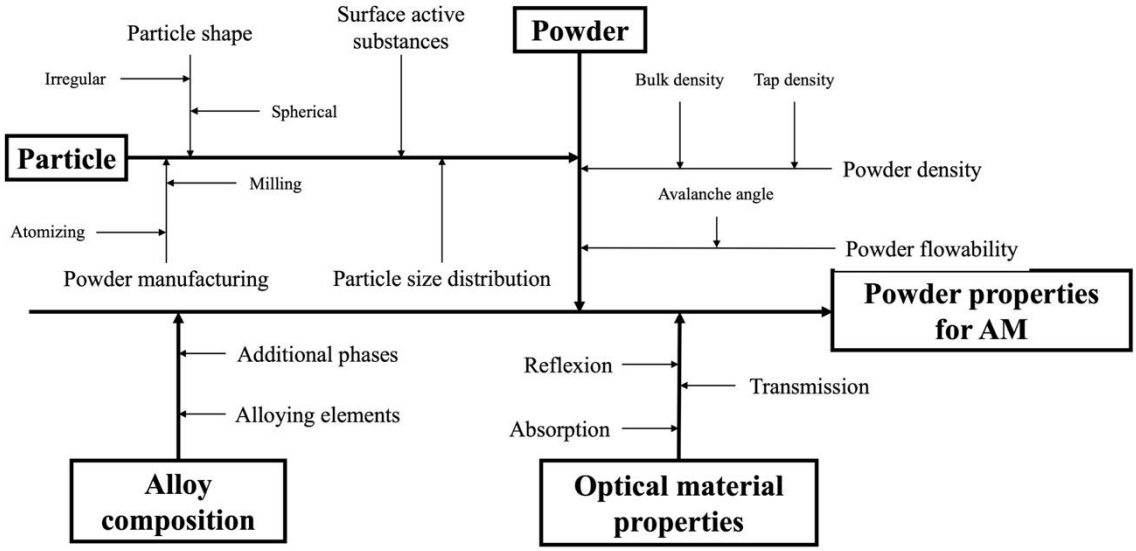

***Figure 2.4**: Ishikawa diagram with influencing parameters for metal powders. Adapted from [33].*

In addition, the outcome of BJ is directly dependent on the powder-binder system employed. Currently, there are several studies focusing on the determination of the occurring interactions and the mitigation of the defects provoked by these interactions. In the following, the main powder properties will be discussed, and the literature on their influence on binder jet process is reviewed.

2.3.1 Powder physical properties

Mean particle size and morphology

The powders (ceramic or metal) used in BJ have a particle size ranging from 0.2 μm to 200 μm [35]. In particular, the mean particle size in stainless steel powders typically ranges between 15 μm and 150 μm. Coarse particles have better flowability, but they also present poor sintering behavior due to a smaller specific surface. Large particle sizes have also a detrimental effect on surface roughness and on the minimal size of features that can be built [42].

Miyanaji et al. studied three different stainless steel 316L powders with mean particle sizes of 14, 31 and 78 μm and reported the influence on material properties [43]. In their study they followed the evolution of density throughout the BJ printing process, the results are shown in **Figure 2.5**. The packing and green densities increase with the mean particle size while the sintering density decreases. This is due to an improved spreadability which allows to form a denser powder bed during spreading. The powder with the smallest mean particle size gives rise to the largest sintering density due to the higher overall surface area, allowing improved diffusional densification during sintering, even though the green and packing density values are smaller than in the powders with higher mean particle sizes.

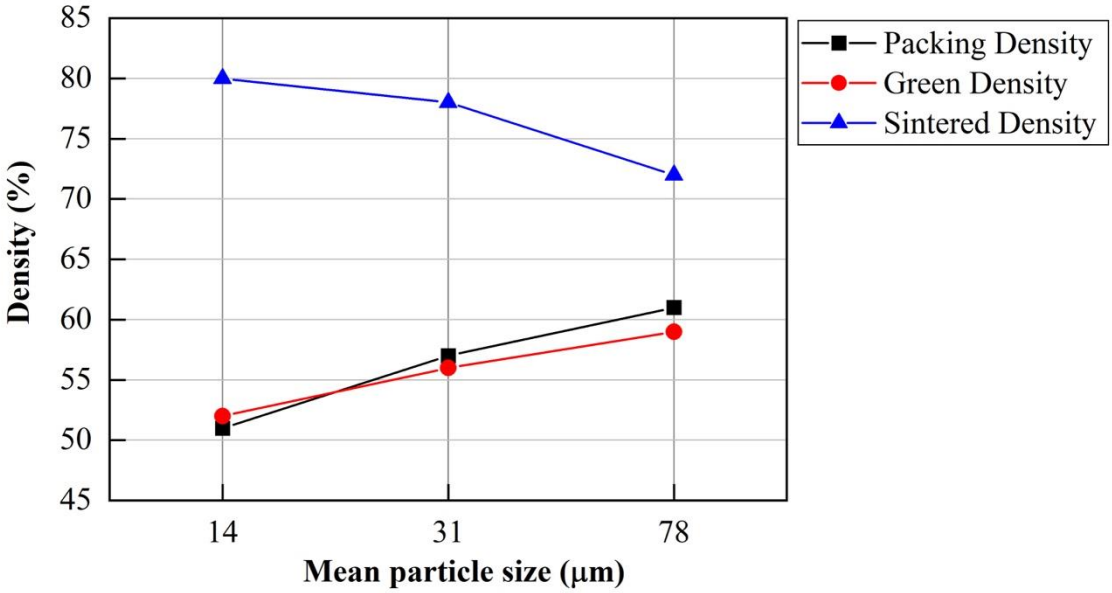

***Figure 2.5**: SS 316L powder size effect on material density through BJ printing process. Graph adapted from Miyanaji et al.* [43].

Dimensional accuracy results manifested higher deviations in the Z axis for larger particle sizes, but lower inaccuracies for the X and Y axis. This was reported to be due to an excessive vertical penetration of the binder for a powder bed with larger particle sizes. The opposite behavior was observed for smaller particles. Tuning of printing parameters such as layer thickness or printing temperature would help reducing these deviations by optimizing lateral and vertical spreading of the binder for a given particle size [43]. Finally, roughness increased as the mean particle size increased, which is consistent with what is expected from larger particles forming a greater peak-to-valley range [44].

The powders employed in AM are in most cases fabricated via gas atomization (GA). Contrary to water atomization (WA) this process produces highly spherical particles while maintaining a relatively reasonable manufacturing cost compared to more advanced production methods [45]. Having said that, water atomization remains to be the cheapest option, which is why researchers are putting an effort on investigating the possibility of using powders fabricated through this procedure. The irregular shape of water atomized particles, contributing to a poor flowability, and their higher oxygen content, are highly detrimental for BJ produced parts. Mostafaei et al. compared the performance of both GA and WA powders with similar particle sizes [46]. Relative densities achieved with WA powders were about a 10% smaller in green and sintered state, leading to worse mechanical properties. Also, visualization of the micrographs of WA produced parts manifested a larger presence of oxide and carbide precipitates. In summary, even though WA irregular particles can be used for BJ, the derived part properties restrain considerably the range of applications in which it might be used today [47].

Particle size distribution

The particle size distribution (PSD) is an important property in any 3D printing process as it affects powder flowability, packing density and densification of a printed part. Mostafaei et al. divided a nitrogen gas-atomized Inconel 625 alloy powder sample of sizes 16-63 μm into three different samples, one containing the whole particle size range, a

second one with a range of 16-25 µm, and the last one with a range of 53-63 µm [48]. Fine particles with a small PSD range exhibited an enhanced sintering behavior at low temperatures, but high linear shrinkage. The broader PSD powder achieved the highest density for temperatures above 1255 °C. Therefore, wider PSD ranges are desired because they provide higher green densities and consequently higher sintered density [49]. Nonetheless, wide PSD ranges are also more prone to powder segregation during handling. Recent research has shown that as a powder batch is cycled through different print jobs there is a coarsening of the PSD, reportedly due to the loss of fine particles, which might make the process harder to control and cause significant variability between the properties of parts belonging to different jobs [50].

PSD mixture strategies have proven useful in overcoming the disadvantages of monomodal distributions in 3DP. Ye et al. developed a model to predict the packing density of powder mixtures and showed that, for bimodal combinations, the ratio of the powders in the mixture can be optimized to obtain a higher packing density [51]. Bai et al. reported a 9.4 % increase in green density by using bimodal distributions of copper powders, which also resulted in additional improvements in sintering shrinkage and sintering conditions sensitivity, allowing a reduction of the energy required for part consolidation. They also reported a 12.3 % increase in the sintered density in comparison with monomodal powders[52]. Similar results were achieved by Do et al. with stainless steel 316L, they also studied mixtures of three different powder sizes. **Figure 2.6** shows the achieved enhancement of green density, greater in the case of trimodal distributions [25].

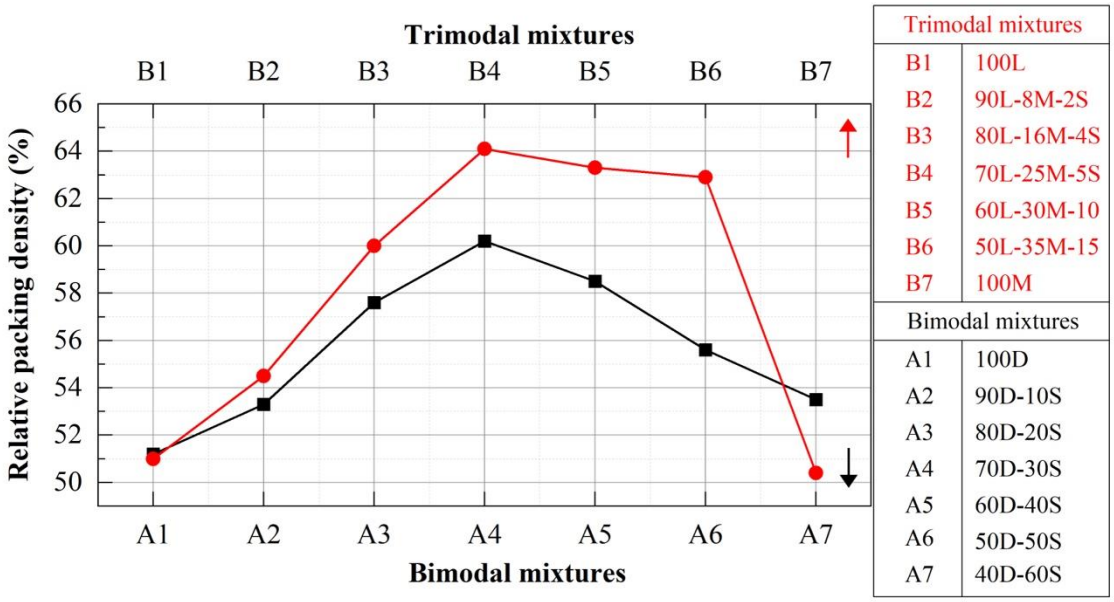

***Figure 2.6**: Effect on packing density of powder mixtures of 2 (A1 to A7) and 3 (B1 to B7) different powder sizes (S, M, D and L account for 4, 14, 30 and 82 µm mean particle size respectively)* [25].

Surface finish is also improved by bimodal powder distributions. According to Lanzetta et al., there is a redistribution of finer particles towards the part surface when printing powder mixtures, which allows a reduction of the surface roughness. Nevertheless, these results were drawn only from printed lines and more complex geometries should be investigated to understand this mechanism [53].

Powder flowability

Powder flowability is directly linked with the formed layer density and is essential for any 3D printing process. Many methods are available to characterize powder flowability (shear cell test, Hall flowmeter, tapped density testing, avalanche test, etc.). The Metal Powder Industries Federation (MPIF) recommends using the angle of repose and of Hall flowmeter tests as it is already standardized for AM powder characterization [54]. The agreement in the scientific community is that the method used has to be representative of the stress state that the powder will suffer during the process. For 3D printing, this corresponds to a dynamic state, for which the avalanche test would be more suitable [41], [55]. However, better correlations between powder flowability and actual spreading performance in the bed are still necessary [56]. The development of new techniques directly measuring powder spreading would ease the powder validation for a specific printing system. To this purpose, new systems are being built with promising results [57].

Powder flowability is a function of several traits of the particles. A high mean particle size and a spherical morphology highly contribute to make powder more flowable [35]. Butscher et al. evaluated seven different calcium phosphate powders with different sizes and production methods and related them to BJ printability [58]. Their investigation concluded that powders with a mean particle size of 24-32 μm allowed an optimal spreading while maintaining a good packing density, as the high cohesivity between particles below this threshold complicated powder flow due to Van der Waals forces becoming predominant [59]. Powder processing methods such as plasma atomization provided a smother particle surface finish which is translated in an improvement of the flowability, which nevertheless proved insufficient for small particle sizes. Similar results were reported by Miyanaji et al. who observed an increase of green density of SS 316L powders as particle sizes increased from 18 to 80 μm. This is directly linked to a better spreading and distribution of the particles related to their good flow properties [43]. However, as previously discussed, a large PSD, containing also small particles, will also be beneficial in terms of achievable packing density. Therefore, both powder properties should always be considered.

Chemical composition

The powder chemical composition has a strong influence on the final sintering step. The typical composition of SS 316L and the role of each of the alloying elements is shown in the **Table 2.4**. Slight changes from this composition may result in a different densification outcome, with the formation of unwanted precipitates like oxides or carbides due to segregation of alloying elements and thus, an uncontrolled process [60]. Contrarily to what is seen in conventional SS 316L, AM SS 316L contains austenite and ferrite, which provides the material higher yield and ultimate tensile strengths and hardness but a lower ductility and corrosion resistance [61]. SS 316L contains a small amount of molybdenum to increase crevice and pitting corrosion resistance. To counteract the ferritizing effect of molybdenum a larger amount of nickel is employed [62]. Additionally, the higher content of nickel also benefits the powders´ compressibility, making it ideal for BJ applications.

***Table 2.4**: Stainless steel 316L composition* [60].

Element	Composition (wt. %)	Function
Fe	Balance	Main component
Cr	16-18	Increase corrosion resistance
Ni	10-14	Stabilize the austenite phase, increase compressibility
Mn	2.0[a], 0.12[b]	Austenitize and enable machining at elevated temperatures
Si	1[a], 0.8[b]	Deoxidizer, control viscosity of the melt during atomization
S	0.03[a], 0.01[b]	Enable machining
C	0.03[a]	Form austenite, L grades have lower content to minimize sensitization
P	0.04[a], 0.01[b]	Control viscosity of the melt during atomization
Mo	2.0-3.0	Enhance crevice and pitting corrosion resistance
N	0.0-0.03	Improve strength and ductility, stabilize austenite at high temperatures

[a] Maximum
[b] Typical

Tracking the amount of carbon and oxygen during the process is critical, as carbon residues left from the binder during sintering may trigger the formation of chromium carbides, depleting the Cr present at the grain boundary and hence making the steel more susceptible to corrosion [63]. Oxygen content can also have a negative impact on part density and mechanical properties of stainless steels [60]. A recent study on the recyclability of metal powder during the BJ process mentioned an increase of the oxygen quantity through powder cycling due to oxygen pickup from the atmosphere or water-based binder [50]. Nevertheless, this increment was negligible when compared to oxygen percentage of fresh powder and no effects were noted. In a study by Zissel et al. the oxygen content and humidity of SS 17-4 PH powder was evaluated for several printing cycles [64]. A 20 % of oxygen pickup was found after the fifth print cycle, this was linked to the worsening of powder properties and thus, to a detrimental effect on the printed parts dimensional accuracy. An inert atmosphere (Ar or nitrogen-hydrogen) during curing significantly improved their results with a limited oxygen pickup.

Given the nature of this technique, the specific binder compositions, and the possible reaction of binder residue with particle alloying elements, further research is required to understand and improve the sintering behavior. E.g., Nandwana et al. analyzed the effect of binder residue in different particle sizes of Inconel 718 and hypothesized that finer powder particles contain more carbon per unit area per particle than larger ones resulting in carbides after sintering, while a mix of carbides and Laves phase where present in sintering of larger particle [65].

2.3.2 Powder-binder interaction

The adequacy of a binder formulation is very dependent on how it interacts with a given powder. Powder-binder interaction takes place during the nucleation process, which can be divided in five steps: droplet formation, impact and breakage, droplet coalescence, penetration, and dispersion [66].

Some studies have shown how the impact of the binder droplets on the powder bed causes metal particles to be ejected, modifying the packing obtained during spreading and creating a less dense layer below the bed surface. This phenomenon is known as ballistic ejection. Two properties govern the particles´ ejection: flowability, which makes it easier to displace the particles after collision, and gravity, that makes larger particles requiring a bigger momentum for ejection. Parab et al. used in-situ X-ray radiographic imaging to show how the combination of both mechanisms contributed to eject particles indistinctly of their sizes [67]. The number of ejected particles was analyzed for two SS 316L powders with particle sizes 9 μm and 30 μm as well as for Si and Al_2O_3 powders. The two former ones exhibited a larger number of ejected particles than Si and Al_2O_3, the reason being the irregular shape of the particles of the last two getting interlocked and hindering their movement (**Figure 2.7**). A wider variety of outcomes was observed in the case of SS316L with 30 μm particle size than in the case of the 9 μm owing to a wider PSD.

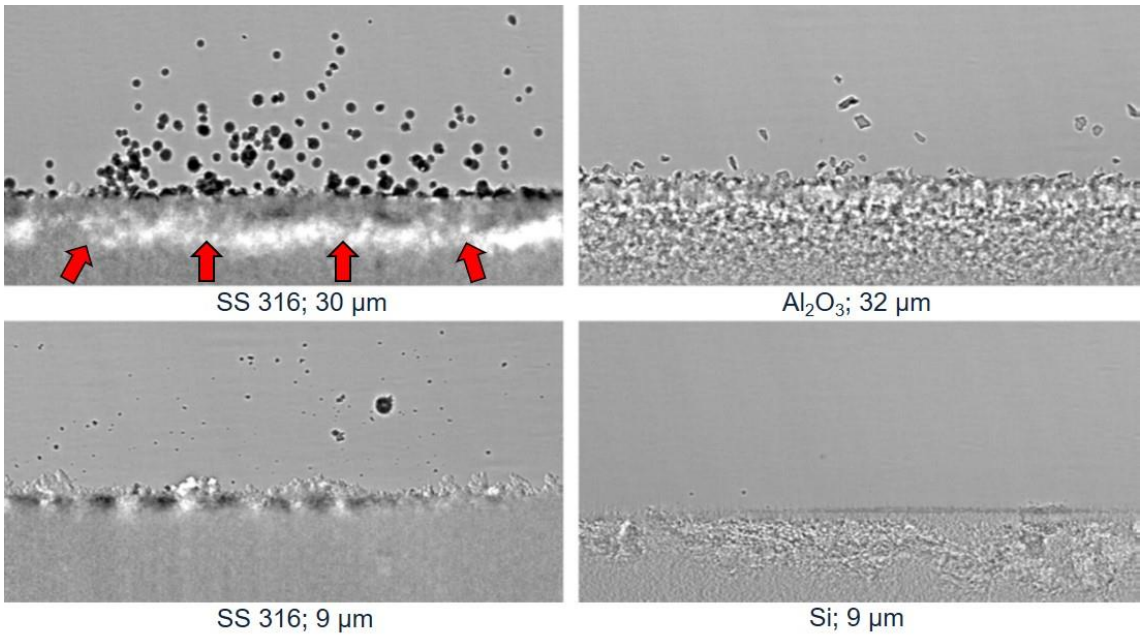

***Figure 2.7**: Snapshots of high-speed x-ray radiography videos from representative experiments at t = 18,8 ms showing ejection behavior of different powders. Red arrows indicate the depletion zone left in the powder bed* [67].

An additional interaction feature to examine is the binder penetration into the powder bed. Binder penetration is governed by two competing mechanisms, horizontal spreading, and vertical imbibition [66], [68]. These mechanisms depend on viscosity, surface tension, initial droplet diameter, impact velocity, powder bed density and wettability. Some studies aimed at characterizing these mechanisms through examination of a printed primitive (powder agglomerate formed with a single binder droplet) and

printed lines [18], [69]. From these primitives the spreading and imbibition lengths for a given powder-binder system are measured and can later be used to choose the adequate printing parameters for an optimal interface. Lanzetta et al. printed lines to evaluate binder penetration and the subsequent particle rearrangement [69], and Bai et al. could use their goniometry analysis on printed primitives to assess the optimal binder saturation for printing with a nanoparticles-based binder [18]. Even though these experiments are valuable for understanding the fundamentals of the interaction process, ideally, characterization should be performed in-situ to account for all the factors included on a real print job.

Researchers have also attempted to make use of simulation models to quantify binder spreading in a powder bed. For example, Tan et al. used such models to observe the final shape of a primitive for different binder impact velocities. However, the required complexity of the model is very high and assumptions for simplification were required, thus making it unpractical for a real 3D printing case [70].

2.4 Sub-processes

As previously explained, to reach a final BJ part, there are several sub-processes to go through. Each one has a strong impact on the resulting final properties and on the microstructure of the part. In this section, the processes are described and the most influential factors for the step optimization are discussed.

2.4.1 Powder transport and spreading

Control of powder transport to the printer and subsequent feeding is necessary for a robust process. Although powder transportation subsystems differ for each technology, they are usually pneumatic systems which minimize vibration to avoid powder segregation [71]–[73]. Some practices also include a mixing step before spreading, that further homogenizes the powder and which can also be used to recirculate the unused powder from previous print jobs [74]. Variations of sizes between particles leading to different flowing behaviors could potentially lead to segregation during spreading. Nonetheless, several studies have proven this segregation to be negligible unless particle sizes differ a lot like when using bimodal powder mixtures [74]–[76]. Other than powder segregation, transportation might also modify powder surface properties through mechanical erosion due to collision between particles or with the subsystems. There is little information available on this issue and on how it modifies powder flowability. However, powder cycling studies suggest that it might not be significant enough compared to other problems related to powder cycling such as coarsening [50].

Powder spreading is typically carried out with a rotational roller or with a blade. Vibration mechanisms are sometimes applied during spreading to decrease inter-particle shear force and increase powder flowability [6], [77]. The spreading speed, which is defined as the velocity at which the recoating system moves the powder forward, is very influential on the quality of the spread layer. Small speeds are desired for a uniform layer formation, still, this is detrimental in terms of printing time, thus, the aim is to maximize

speed while maintaining a considerably uniform layer [78], [79]. One more parameter related to the layer formation is the feed-to-powder ratio (thickness of feed layer/layer thickness). This parameter was investigated by Shrestha et al. together with other printing parameters using a Taguchi experimental design, with the goal of maximizing the transverse rupture strength [78]. The feed-to-powder ratio was found to be a critical parameter, increasing powder bed density as the parameter increased up to a ratio of 3.

Different strategies have been studied to increase the formed layer density, as the one proposed by Cao et al. [75]. They used the Double Smoothing (DS) method, introduced by Lee Sang-Joon in 1992, by which, firstly, a thick layer of powder is created with the usual counter-clockwise rotating mode of a roller, followed by a second smoothing step retiring part of the powder previously deposited on the layer [80]. This mechanism allowed them to obtain green densities as high as 70%.

The usage of powder spreading simulation tools has given a lot of information on the spreading process and is very valuable to explore different spreading setups effect on layer quality, roughness and density while saving up time and costs related to experimentation [81]–[83]. These simulations though, are not often complemented with real tests. This last step should be carried out with each particular system to ensure that simulation is as accurate as needed.

2.4.2 Printing

BJ´s main advantage with respect to other 3D printing techniques is that it does not require heat during printing to melt the powder, avoiding the high temperature gradients on the build which are detrimental for the material properties [5]. Most of the parameters involved in the BJ process differ from those impacting in SLM or EBM AM technologies, making it unique and not comparable [2], [84]. The use of a binder adds complexity to the system and forces the redefinition of the principal variables. Because of the existing large interactions between printing parameters, complete studies should make use of a systematic approach, analyzing several combinations of these parameters to dig into all possible outcomes. In this section, the controlling factors of the BJ method are discussed and their effect on part quality and material properties is summarized.

Layer thickness

The layer thickness is a common parameter in most of the AM processes and it is described as the distance by which the build plate is lowered after each printed layer. The layer thickness determines the minimum printable feature size and it constitutes a trade-off between material properties and building time. Thinner layers provide better mechanical properties but significantly increase process time [24], [84].

Typical layer thickness values in BJ range between 50 and 150 μm, in general, layer thickness of 2 to 3 times the particle size or larger than the bigger particle will maintain good flow and spreadability [35], [85]–[87]. Simulations of the spreading process executed by Meier et al. further confirmed these values (**Figure 2.8**) [83]. Their study was focused on a powder size of 17 μm which have considerable cohesive forces. Different surface energies of the bed were also analyzed, indicating that the powder layer quality further decreases if the adhesion between powder and substrate is weakened.

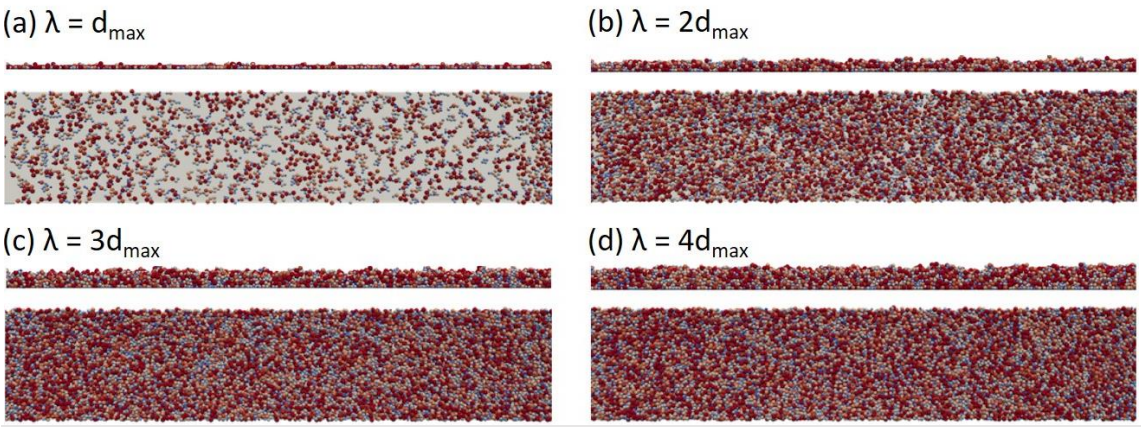

***Figure 2.8**: Side and top views of the resulting powder layers for different layer thicknesses λ, and a specific surface energy γ_0* [83]. *Particles are colored according to their size from smaller (gray) to bigger (red).*

Most of the layer thickness studies are coupled with other important printing parameters. This is expected since, as it was previously stated, parameter interactions in the process are notable. Enneti and Prough reported that just by increasing the powder layer thickness from 50 μm to 70 μm, there was a reduction of the green strength of WC-12% Co samples from 1.56 MPa to 1.32 MPa in the case of a binder saturation of 75 % and from 4.22 MPa to 2.25 MPa for a 90 % binder saturation [88]. Other studies on SS420 also showed that surface roughness also significantly improved upon lowering the layer thickness [54]. Sheydaeian et al. measured the porosity of printed Ti samples through μ-XCT and the Archimedes method [86]. Part density was linked to the chosen layer thickness, and it revealed a higher porosity for thicker layers, which is in accordance to the observed relation with mechanical properties. Interestingly, they leveraged this finding to print parts with varying layer thickness which resulted in a tailored part density progression.

Printing temperature and drying time

Despite the fact that BJ does not require high amounts of heat during the printing process, a certain temperature has to be applied to partially remove the solvents present in the binder formulation. This leads to an increase of the binder viscosity which is in conflict with obtaining an adequate binder infiltration. The drying time is highly linked to the printing temperature since it will define how long is this temperature applied before spreading the following layer. Generally, while the current layer is drying, the printhead is moved towards a cloth where the nozzles are automatically cleaned, as this step helps to minimize clogging and sets the minimum drying time of the printer [89].

The printing temperature plays an equivalent role to what is referred in the literature as the heater power ratio (R_{HP}), which is calculated with the equation ***(2.1)***, where P_C is the current-heater-power, and P_M is the maximum heater power [89].

$$R_{HP} = \frac{P_C}{P_M} \times 100 \qquad \textbf{(2.1)}$$

Results from Chen and Zhao indicate that an excessive amount of heat might not only increase energy consumption but also resulted in part distortion and shrinkage, whilst too low energy might be insufficient to dry the binder [89]. For all the found

optimal combinations of parameters, they deduced that a heater power ratio of 70% could maximize dimensional accuracy and surface quality.

The effect of the drying time or of the printing delay on the mechanical properties of plaster powder was studied by Farzadi et al. with special attention on resistance under compression [90]. Drying times of 50, 100, 300 and 500 ms were applied to print scaffolds. Compression properties including Young modulus, strength and toughness increased with increasing delay time until the 300 ms, and remained constant afterwards, indicating the complete penetration of the binder at this point. Enneti and Prough´s research clearly manifest how dependent on the binder-powder system this parameter is [88]. In their case, the material used was WC-12%Co and drying times employed were 7 and 14 s. Regardless of the fact that delay times were an order of magnitude larger than the ones of the previously mentioned study, green strength showed to still increase for larger delay times, revealing that longer binder settling times were necessary in this case. For this reason, each particular powder and binder combination should be optimized according to their interactions.

Binder saturation

Binder saturation is defined as the percentage of the binder infiltrated in the volume not occupied by powder particles, it is estimated with the following equation ***(2.2)***:

$$S = \frac{V_{BINDER}}{V_{AIR}} = \frac{V_{BINDER}}{(1 - PR) \times V_{SOLID}} \qquad \textbf{(2.2)}$$

where, V_{BINDER} is the volume occupied by the binder, PR is the packing ratio (%) and V_{SOLID} is the volume of the powder particles. Saturation values are typically between 50-70 % [35]. Too low saturation will result in insufficient binder to join the powder layers, while an excessive saturation will bind more powder than desired and cause bleeding, decreasing dimensional accuracy and final surface quality (**Figure 2.9**) [89], [91].

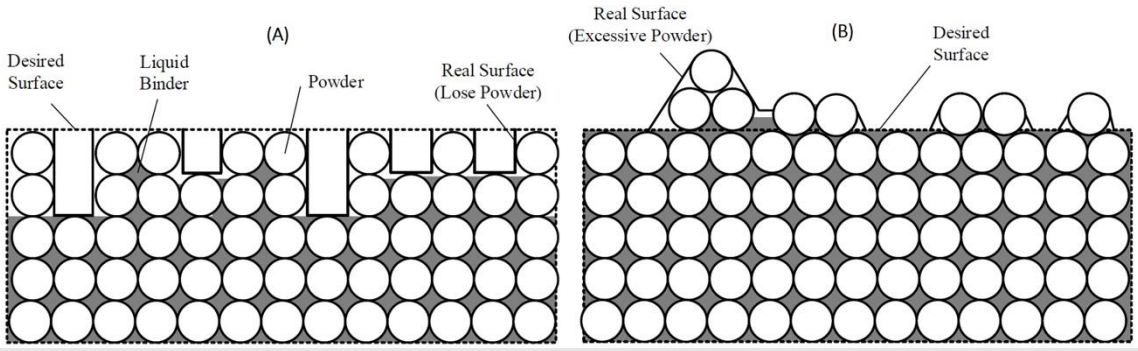

Figure 2.9*: Binder saturation effect on layer surface quality (A) The lower-level printing saturation leads to lose powder (B) The higher-level printing saturation leads to excessive powder bond* [89].

Many studies reported that an increase of binder saturation highly improves mechanical properties of the green part [85], [88], [91]. Vaezi analysis of green flexural and tensile strength with ZP102 plaster powder manifested that these properties practically doubled by increasing binder saturation from 90 to 125 % (saturations above 100 % indicate a larger volume of binder than the available space in the printable area is jetted) [85]. Enhancing mechanical resistance of the printed parts is desired to facilitate

further handling and avoid cracking. However, it may also affect the debinding step complexity and the remaining porosity of the sintered sample. More studies should be carried on this topic in order to fill the current knowledge gap.

An interesting approach for setting the best binder saturation level is the one provided by Miyanaji et al. [92]. The researchers built a model based on capillarity effect to determine the equilibrium saturation in a specific binder-powder system, i.e., the point at which the binder stops migrating due to the balance of capillary pressure and surface tension (**Figure 2.10**). Experimental analyses were also conducted to validate the model. In particular, two different materials were tested, Ti-6Al-4V and SS 420. The model successfully established the required binder saturation for equilibrium in the Ti-6Al-4V sample. However, the binder saturation was overestimated in the case of SS 420. This was attributed to internal microscopic surface areas being considered in the model which, in reality, do not contribute to the wetting of the powder [93].

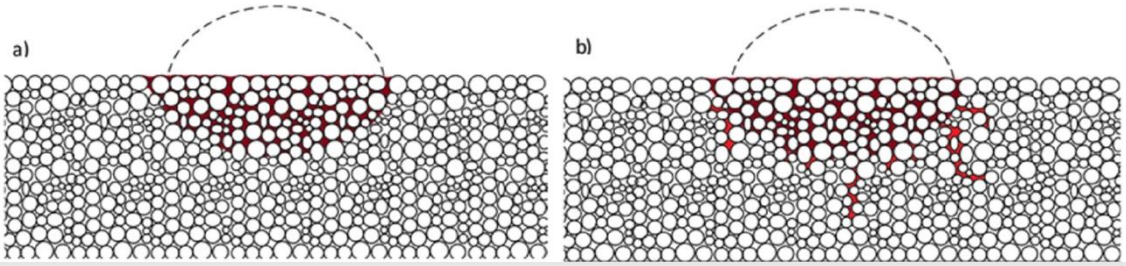

***Figure 2.10**: Schematic presentation of a binder droplet pattern inside powder bed (binder droplet after reaching equilibrium state); a) assuming small pore size, b) assuming large pore size* [93].

Further improvements of this model were developed by Colton and Crane [94]. In their model they included the effect of the printing parameters like droplet size, velocity, and spacing on printed lines effective saturation. While smaller drop and powder size provided less variation in saturation a large droplet spacing contributed to destabilize line formation, i.e., blocking consecutive drops to bind together. Future work should focus on extending this knowledge from lines to layers, and finally, to printed parts, going through the control of the binder's viscosity along the process.

Part orientation and location

Given the anisotropic nature of the process, where the powder is spread in a specific direction whilst the binder is dropped vertically in the powder bed, it is convenient to consider part orientation as an influential factor. In addition, the location of the heating system and the extraction of the solvents may also interact differently with powder located at different build positions. However, this is very specific of each 3D printing equipment and thus, no public information has been found in this regard.

The impact of the X (printhead movement direction) and Y (spreading direction) orientations on mechanical properties of printed SS 420 was analyzed by Oh et al. [95]. The bending strength dropped from 10 MPa to 4 MPa as the angle between the Y axis and the main orientation of the part decreased. The given explanation was the asymmetrical spreading and the penetration of the binder, due to the Y component of the drop speed, as it is jetted from the moving printhead. This was further verified by Miyanaji [96]. Doyle et al. demonstrated that infiltration can be used to overcome X and

Y anisotropy. Their research on SS 420 bronze infiltrated parts revealed that mechanical properties differences coming from part orientation were insignificant compared to the effect of varying layer thickness [87].

As a consequence of green part anisotropy, linear shrinkage due to part sintering differs from axis to axis. Wang and Zhao designed an experiment, following the Taguchi methodology to minimize dimensional distortion due to shrinkage considering the three axes in the build. The determined shrinkage rates in the X and Y axes for the studied sintering parameters particularly diverged from the observed in the Z axis, which made the optimal choice of sintering parameters sit in between both extremes [17]. The shrinkage behavior in the print direction (Z) was assumed to be due to the formation of a depletion layer as the binder collides with the powder bed [67].

2.4.3 Curing and depowdering

The curing step is crucial to ensure the binder cross-links and sticks to the metal powder as this will give enough strength to the part to avoid cracking during depowdering and allow further handling before sintering. There is little literature available on the curing process, and practically no information on its effect on green part mechanical performance and density.

Normally, curing is carried out in the same build box used for printing. The build box is then introduced in a curing oven where temperature is applied for a certain amount of time, depending on the binder used and on the size of the box [97]. Curing temperatures typically range between 120-200 °C and time needed is in the order of 3-6 h [17], [98], depending on the plot dimensions and part's density within the powder bed. The curing process is generally easy to optimize by leveraging the knowledge already available from fields like conventional powder metallurgy or MIM. However, some binder formulations make use of volatile solvents to transport the binder, which need to be removed through a vacuum pump during curing. No public studies are available on the effectiveness of this process even though it is critical to evaluate powder recyclability and carbon content.

Once the build box is cured, the parts need to be extracted from the powder bed. In general, this is performed under air pressure and manually, using different brushes and with extra care in order not to distort the printed parts, which seriously prevents production technique´s automation. Technology providers are putting a lot of effort on the development of affordable and efficient solutions to this problem in order to automate the use of BJ in the industry [99].

2.4.4 Sintering and debinding

Debinding and sintering can be performed in the same furnace consecutively to minimize production time. The process usually involves two isotherms, one for debinding and a second one maintained for sintering [97]. During debinding, no residual carbon must be left since it may alter the part properties and composition by production of carbides, also, oxidation of the metal has to be avoided since it would impede further densification [47]. The impact of carbides has been widely studied for MIM parts [100], [101], as they can cause porosity gradients along the piece, which are detrimental for mechanical properties.

Still, the amounts of binder used in BJ are much smaller than in MIM, and thus translating the conclusions of these studies might not be entirely possible. Moreover, there are many binder-powder systems available using BJ technology, which may respond differently to a specific heat treatment. A parameter optimization for each one of these systems is required to ensure a maximum yield.

Sintering time and temperature are amongst the most studied variables of the sintering process as they contribute a lot to the results of the final consolidation [47], [52], [61], [102]. As a general rule, the sintering temperature has to be high enough to promote neck formation, growth and subsequent diffusion but it must not exceed the melting point to restrain shape distortion (liquid phase sintering). Verlee et al. studied how parts built with different SS 316L powder sizes reacted to a wide range of sintering temperatures and times [102]. Their results clearly manifest the direct relationship between the applied temperature and the density, as well as the better performance of smaller particles due to a higher specific area. The sintering time followed a linear trend with density for each given temperature until reaching a 90 % of relative density. At this stage, porosity was fully closed, and densification mechanisms changed, leading to a reduction of the effect of time on consolidation.

The most common atmosphere used during debinding and sintering is Ar mixed with hydrogen, and processing is also often carried out in vacuum. Do et al. showed that sintering in vacuum helps to obtain up to 10 % higher final densities compared to argon [103]. Similar results were shared by Juan [104]. The reason for this density enhancement is that the vacuum maintains pores on the grain boundaries, where they can further shrink and be eliminated through evaporation/condensation processes. Ar on the contrary, is unable to remove gas pores entrapped within grains [35]. However, Ar is key to ensure the elimination of oxygen during the process, which cannot be guaranteed by vacuum sintering, leading to a worse surface condition [103].

A strategy worth mentioning for increased final part density is the so-called shell-printing. It consists of jetting the binder only on the surface of the built part and leave the core as a compact of loose and packed powder without binder [61]. This derives in a fragile green part that requires a smaller amount of energy to be fully debound and consequently exhibits a noticeable increase of density once sintered (**Figure 2.11**). More efforts should be put on studying this sort of procedures to fully squeeze BJ´s versatility.

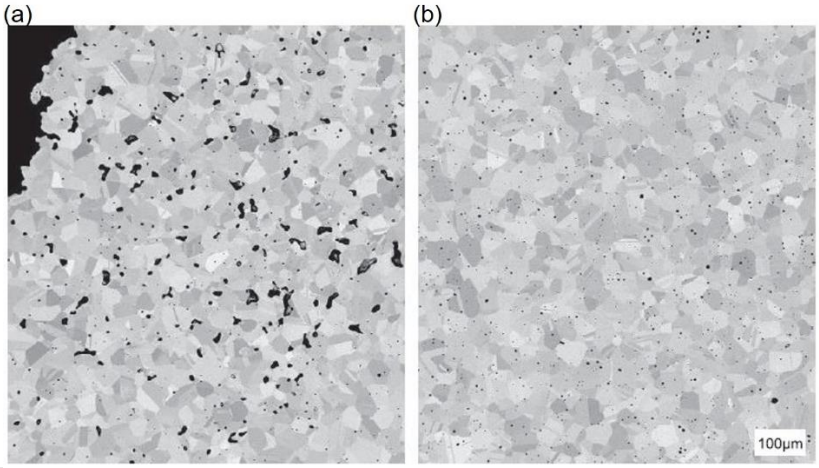

***Figure 2.11**: Porosity and microstructure of bulk after shell-printing and sintering (a) shell; (b) core* [61].

One of the main challenges that BJ faces is the uncontrolled shrinkage produced as a consequence of densification [47]. This has a negative impact on the dimensional accuracy (**Figure 2.12**). The effect of sintering time, temperature and heating rate on the dimensional accuracy was studied by Wang et al. Their conclusion led to different temperatures being optimal for the different axis considered (X, Y and Z). The sintering time and the heating rate proved less influential on shrinkage [17]. There exist many models to predict sintering shrinkage and to consequently modify part design [105]–[107]. Nonetheless, the geometries studied are either too simple or they are used in very specific applications. Further improvement of these models for a wider range of geometries and features would help to address this matter and to reach more demanding tolerances. Finally, the shrinkage effect might also be mitigated by achieving a higher green density during printing by using, for example, bimodal powder distributions [52].

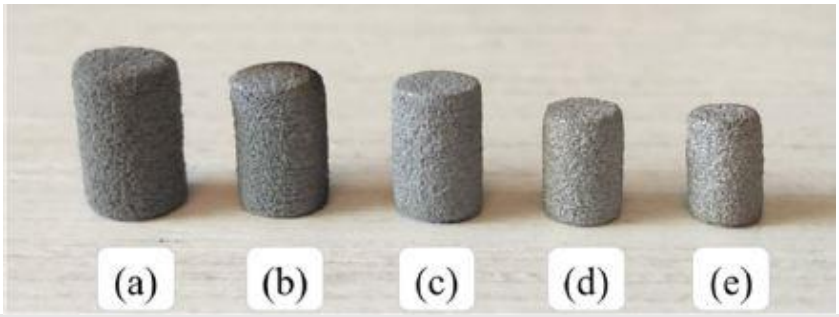

***Figure 2.12**: Dimensional shrinkage of iron due to sintering under 95% Ar – 5% H_2. Sample A in (a) green state, and sintered at (b) 1390 °C, 2 h, (c) 1390 °C, 6 h, (d) 1490 °C, 2 h and (e) 1490 °C, 6 h.* [47].

Other attempts to increase sintered density of stainless-steel printed parts examine the use of boron and Si_3N_4 compounds as sintering additives. These additives promote grain boundary diffusion upon densification, helping to attain almost full part density with lower sintering times and temperatures needed. Nevertheless, elevated percentages of additives (> 0.5 %) can drive to a high distortion of the original part geometry [11], [25].

2.4.5 Additional post-processing

The resulting porosity of a BJ printing sample is generally not negligible, and thus post-processing is necessary for applications requiring net-shape and robust mechanical properties. The most common post-treatment strategy in BJ is sintering, although there are a wide variety of options that can be applied additionally or as an alternative to sintering depending on the application of the printed components (e.g., infiltration, HIP, surface or heat treatment) [6].

Compared to sintering, metal infiltration is highly beneficial to control dimensional shrinkage, although it also changes the composition of the final parts. For this reason, infiltrated parts are generally treated as composites [108]. Cordero at al. applied simultaneously tin bronze infiltration and sintering on ferrous green parts fabricated via BJ process and compared mechanical properties of the components after both treatments. Infiltration specimens yielded a significantly lower porosity of 2 % compared to the 33 % of the sintered, consequently, transverse rupture strength, increased from the 130 MPa of the sintered sample to 570 MPa of the infiltrated one [16].

Lu et al. combined both treatments on BJ printed stainless steel 420 by performing a pre-sintering step between 1000 °C and 1400 °C followed by bronze infiltration [108]. The aim of pre-sintering was to induce neck formation between powder particles, thus, to improve material strength, facilitate handling, increase mechanical properties after infiltration and control the preform porosity. Their studies showed that infiltration was non-uniform across the samples and three possibilities were given for this fact, firstly, the presence of large voids impeding infiltration by capillarity, secondly, the acceleration of the densification of the wells at the outer region due to the bronze melt during infiltration and lastly the erosion of the wells by the melt changing in time its composition. Nonetheless, pre-sintered temperatures of 1300 °C and 1350 °C remarkably improved this behavior by reducing the channel size while maintaining open porosity, this resulted in an enhancement of the tensile properties of the bronze infiltrated SS420 composite up to a 60 % (UTS of 1053 MPa).

HIP is a common post-processing step in powder metallurgy, its aim is to reduce remaining porosity after sintering, nonetheless, to have a significative impact it requires closing spherical pores with a previous part relative density of 90-92 % at least [6], [61].

The analysis of BJ printed copper parts carried out by Zhu et al. provided more insights into the extend of HIP impact on final densification [109]. They applied 1075 °C under an argon pressure of 207 MPa for 2 h on a sintered sample. Archimedes measurements of the sintered and HIPed samples gave an increase of relative density from 95.5 % to 99.2 %. Samples were also examined through XCT at the different stages of the processing chain and porosity morphology was evaluated from the 3D scans. HIP showed to decompose remaining reticulated porosity of the sintered sample, favoring the creation of more isolated pores with isotropic shapes [109]. Kimes et al. studied the impact of different HIP treatments on fatigue behavior. They applied different temperatures (1130 °C, 1165 °C) during 75 minutes at a pressure of 150 MPa. According to their results, HIP provided a more homogeneous porosity in the samples, thus, an improved isotropy. Nonetheless, none of the HIP treatments had an impact on fatigue life over as-sintered parts. They claim these results to be inexact due to the high surface roughness and amount of defects present near the surface, which led to crack initiation there. To further quantify the impact of HIP on fatigue strength, the contribution of the internal structure should be separated from the effect of surface condition by previous mechanical polishing [110].

Yegyan Kumar et al. further investigated the effects of HIP on mechanical and physical properties of printed copper parts with varying powder sizes. HIP procedure was followed with the same parameters used by Zhu et al. [109]. Bimodal distributions of printed powders showed to benefit the density increase, achieving a 90.5 % for as-sintered and a 97.3 % for HIPed samples. Sintered samples printed with a monomodal particle´s distribution of 25 μm and 17 μm average diameter powders did not reach the minimum of 90 % density, leading only to a 4 % increase of density after HIP. As expected, material properties increased with density (**Table 2.5**), nonetheless, tensile strength for the highest density HIPed part was about an 80 % of the strength of wrought copper, thermal conductivity was also lower than the expected, and this was attributed to differences in copper microstructure and grain sizes as well as to the presence of residual carbon [111].

***Table 2.5**: Mechanical and physical properties of BJ copper parts* [109], [110], [112].

Powder size (µm)	Processing	Density (%)	UTS (MPa)	Thermal conductivity (W/m·K)
25	Sintered	77.7 ± 1.2	82.0 ± 5.3	245.7 ± 4.7
	HIPed	82.4 ± 0.3	129.3 ± 0.9	256.5 ± 4.4
17	Sintered	83.6 ± 0.4	115.8 ± 9.2	262.3 ± 8.2
	HIPed	85.8 ± 0.2	135.3 ± 13.7	266.3 ± 18.5
Bimodal	Sintered	90.5 ± 0.3	144.9*	293.5 ± 5.5
	HIPed	97.3 ± 0.1	176.4 ± 6.5	327.9 ± 7.1
Wrought	Wrought	100	414	385

* Only one sample measured.

Additional post-processing might include heat treatments or surface finishing. Their use is very uncommon, and it is limited to applications where a high performance is required, such as in the aerospace industry [113], [114].

2.5 X-ray Computed Tomography for AM

XCT has become increasingly interesting for manufacturing over the years due to the three-dimensional information that it provides and its non-destructive testing nature [115]–[117]. It stands out over 2D techniques such as scanning electron microscopy (SEM) or optical microscopy (OM) when used to obtain more detailed and reliable data about internal defects or about shape and porosity of powder feedstock. Also, it facilitates the detection of heterogeneities within a sample, e.g., of specific zones of a volume which present higher porosity, and which may go unnoticed by using 2D techniques.

Thompson et al. highlighted the significance and versatility of XCT in AM [117]. They underlined the relevance of this technique in reverse engineering, especially for medical applications, and focused on the evolution of its application in pore measurements and in dimensional metrology. As mentioned in the review, XCT is highly practical for measuring porosity and pore morphology distribution and linking them with mechanical performance. Du Plessis et al. successfully correlated pore sizes with strength and ductility of materials produced through L-PBF, concluding that small pores up to 0.5 mm or an extend of porosity up to a 1 % do not significantly contribute to mechanical properties. Additionally, they noted how irregular pores are more detrimental for mechanical properties than other forms of porosity, creating a preferential site for crack initiation [118].

Information about the shape and orientation of pores is also very valuable for predicting mechanical behavior. Ziólowski et al. produced three specimens by SLM with different orientations with respect to the printing direction. Using XCT they were able to build a 3D defect map of each sample according to their orientation (**Figure 2.13**). This

information could be used to forecast crack initiation and propagation without the need of mechanical testing [119].

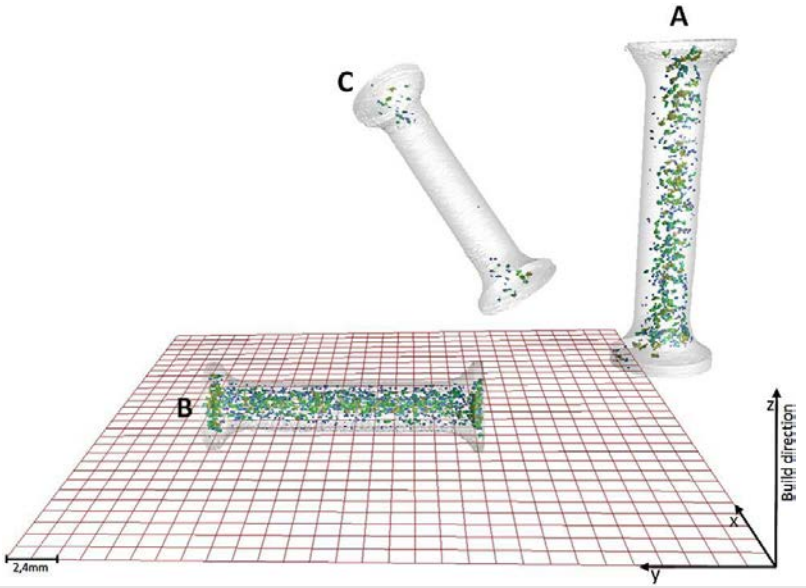

***Figure 2.13**: 3D visualization of specimens´ defects maps according to their orientation in the SLM chamber* [119].

Zhu et al. studied and developed a pipeline for quality control of BJ copper samples by using XCT for characterization, machine learning algorithms to reduce scanning time and principal component analysis (PCA) for a deeper study of porosity evolution [109]. They characterized samples at three different stages of the BJ process (green state, sintered state and after HIP), obtaining detailed information about pore size (volume, volume ratio), shape (eccentricity, compactness, solidity) and orientation (altitude angle) at each one. By applying PCA, they were able to condense all the information in 4 different groups of pores (quasi-spherical pores, small-elongated pores, large-elongated pores and reticulated defects). Following the population of the 4 groups of pores at each step allowed them to comprehend the physical insights behind each process stage (**Figure 2.14**).

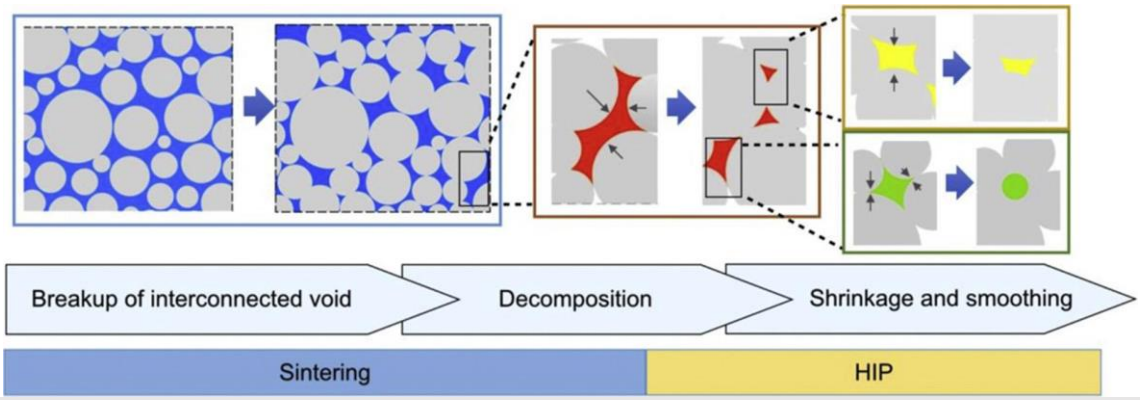

***Figure 2.14**: Porosity morphology evolution mechanisms throughout the BJ post-processing of copper parts, blue, red, yellow and green colors represent the four pore evolution patterns of 1) pore segmentation due to densification of loose particles, 2) decomposition of interconnected pore due to necking, 3) pore shrinkage and 4) pore smoothing* [109].

A recent study by Sperling at al. shared in the WorldPM2022 conference employed an XCT-based method to compare several print jobs and their resulting porosity distribution [120]. In their approach, a directional analysis of the scanned volumes was conducted and compared to other samples. This allowed for a deeper characterization of the porosity and the layering pattern, usual in BJ technologies.

One more benefit of XCT in 3D printing is that it can provide accurate dimensional metrology data of complex shapes with inner structures and multi-material parts that can´t be examined through conventional methods [86]. However, because of the material attenuation coefficient, there is a limit on the part dimensions that can be scanned, this is generally not a problem in AM, where we are dealing with pieces of several centimeters [117].

X-ray Computed Tomography can also be used to obtain surface topography measurements. Thompson et al. investigated the influence of the measurement setup parameters over accuracy by comparing with coherence scanning interferometry (CSI) results and deduced that geometric magnification had a bigger impact in the quality of the topographic reconstruction than sampling resolution, establishing a magnification 20× as the optimal [121]. Zanini et al. emphasized the potential of the technique to acquire information about re-entrant features, and to obtain deviations lower than a 10% when compared to the actual surface morphology for most of the surface texture parameters [122], this makes X-ray Computed Tomography a very capable technique for surface measurements although the use of additional analysis such as CSI is recommended.

Another field for which XCT can be valuable within AM is in the characterization of metallic powders. Chen characterized Ti-6Al-4V powders through SEM and synchrotron XCT, leveraging the advantages of both techniques [123]. While SEM gives more insights about powder surface morphology thanks to its high resolution and magnification, XCT can better define internal defects like porosity and particle shape through 3D geometrical features (sphericity, eccentricity, etc.). Thiede et al. also took advantage of synchrotron XCT to analyze particle size and shape, employing this information as an input in powder bed simulations for setting the appropriate layer thickness of the LPBF process. Their results demonstrated the role of small particles on compensating for defects of the powder bed and that the layer thickness should be smaller than the D90 value to obtain an acceptable packing density [124].

Finally, in-situ XCT can be further applied on the dynamic characterization of AM materials, e.g., to investigate printing and sintering mechanisms in thermal treatments or crack nucleation and growth during mechanical testing [125], [126]. Lame et al. studied the densification mechanisms of copper and steel compact powders and their work yielded new insights on the origin of the anisotropic shrinkage observed during sintering of powder compacts. According to them, neck formation facilitates small displacements and rotations of particles leading to local rearrangements for which some pores in a preferential orientation decrease in size while others increase (**Figure 2.15**) [127].

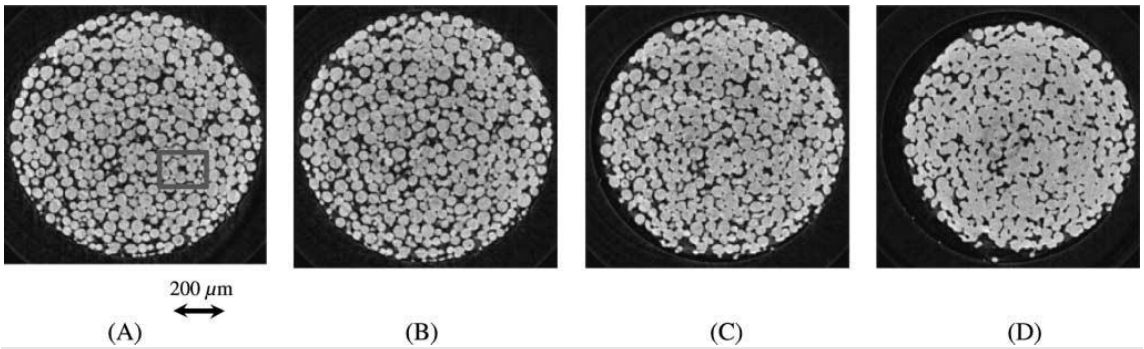

***Figure 2.15**: 2D reconstruction of Cu powder during densification. (A) Initial stage, (B) After achieving sintering temperature of 1050 °C, (C) Half of the total sintering time, (D) After cooling down* [127].

3
MOTIVATION AND OBJECTIVES

The commented literature on BJ 3D printing shows that a big effort has been made to increase the available knowledge on the topic. Most of the investigations focus on the study of the printing process parameters and the relation of these parameters to the sintered part properties as well as to process input (powder properties). A gap has been noticed regarding the characterization of green parts microstructure, a crucial step in the process that has a lot of potential to further understand the mechanics of the printing process. Such characterization should include all the phases present in a green part, i.e., porosity, particles, and binder. In addition, as it is desired that BJ advances towards industrialization, the automation and ease of use, as well as standardization, of such a complex characterization would be necessary. This, would in turn, lead to a more sustainable process by an early identification of defects and consequent rejection of the parts before sintering.

Also, there is a lack of literature available considering the impact of part size and geometry on the printing outcome. The geometry of a part and its features has a significant impact on the local properties of the part due to binder infiltration differences. This is of critical importance regarding the near net shape AM technology definition and in front of the controversy regarding testing final geometry parts against ingots. Investigations addressing this matter study primitives (a single droplet interacting with powder) and line formation [69], [128]. To date, these differences have been tackled through the distinction of shell and core materials during printing, which is insufficient to overcome the complexity of the relationship [61]. Furthermore, most of the presented studies employ relatively simple shapes, generally chosen to perform standard mechanical testing. Nevertheless, one of the commonly shared advantages of AM is the possibility to print

complex geometries. This being considered, print modes should be dynamic and evolve according to the local geometry or position of the sample being printed for geometries for which the printing conditions impact part quality.

Finally, surface defects and roughness are key properties of the final part. These properties define the accessibility to additional post-treatment technologies (e.g., milling, machining, HIP, etc.) and thus, influence the range of applications available for the printed parts. BJ directional nature frequently leads to gradients along the part, thus, significant differences in terms of surface quality and defects appear as we get closer to the surface edge and between each part border. In the literature, it is common to see porosity gradients within a part border, yet little investigations consider the impact of these gradients [120], [129].

Based on these findings, the objectives of this thesis are defined as follows:

Objective 1: Develop automated characterization methods that enable the subtraction and comparison of novel metrics between BJ green part.

Objective 2: Contribute to the existing knowledge of BJ printing process providing a comprehensive characterization of green parts and their resulting sintered parts.

Objective 3: Investigate the impact of part geometry, size, and features on the resulting microstructure with control from their macrostructural properties.

Objective 4: Advance the understanding of the relationship between surface defects, printing recipe, and machinability.

4
MATERIALS AND METHODS

In this chapter, the materials employed for the investigation are described. Next, an exploration of the utilized BJ system is shared. A detailed description of the employed printing parameters and builds for each experiment are exposed in their respective chapters. The sintering process for densification is also reported. In addition, the analytical tests for powder, green and sintered part characterization are described. Finally, novel methodologies developed in this research work with the aim to quantify the microstructural data are explained.

4.1 Materials

Given the length of the investigation and its scope, multiple stainless steel (SS) powders were employed. In this section, the details of their respective compositions and properties are discussed together with the used binder.

4.1.1 Stainless steel powders

The presented investigation was mainly focused on stainless-steel 316L powder. However, some experiments were conducted with SS 17-4PH aimed for a wider variety of applications.

The chemical composition of the three powders included in the investigation are shared in **Table 4.1**. A certain amount of oxygen is commonly present in gas atomized powders [45]. However, a limited quantity of oxygen can contribute to get rid of the carbon content during debinding.

Table 4.1: *Elemental composition of SS powders.*

Elements	SS 316L (wt. %)	SS 17-4 PH (wt. %)
Iron	Balance	Balance
Chromium	17	16.7
Nickel	10.75	4.34
Carbon	0.012	0.02
Molybdenum	2.24	0.16
Nitrogen	0.081	0.1
Sulfur	0.004	0.01
Oxygen	0.07	0.17
Silicon	0.72	1
Manganese	1.02	0.69
Phosphorus	0.015	0.02
Copper	-	4.06
Cobalt	-	-
Niobium	-	0.2

The morphology of the selected powders is shared in **Figure 4.1**. The typical nearly spherical shape from gas atomized powders can be observed. Some particle satellites are present, and a very limited amount of surface defects can be detected for SS 316 L powder. On the contrary, the SS 17-4 PH powder shows rougher particle surfaces that can have a significant impact on the powder flowability and spreadability.

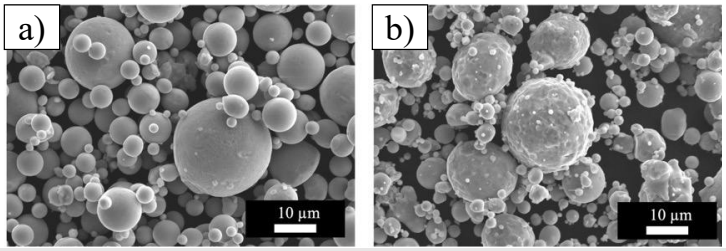

Figure 4.1*: SS powders morphology. (a) SS 316 L; (b) SS 17-4 PH.*

The particle size distribution provided by the vendor of the powders is compared in the **Table 4.2** with the D10, D50 and D90 values corresponding respectively to the 10, 50 and 90 percentiles of the particle´s diameters. The selected particle size range was chosen to attain a high packing density and enhanced sintering behavior due to a high surface area. A wider PSD range is noticed for SS 17-4 PH powder.

***Table 4.2**: Particle size distribution of SS powders.*

Powder	SS 316L (µm)	SS 17-4 PH (µm)
D10	5.3	4.6
D50	12.8	14.2
D90	24.8	31.4

4.1.2 Binder

The binder employed in this investigation was formulated by HP Printing and Computing Solutions SL.

4.2 Printing process

An HP 3D MetalJet S100 machine prototype was employed to print all the samples from this research. MetalJet was firstly introduced in 2018. It was originally built by leveraging the acquired knowledge in the company with the 3D polymers printer (MultiJet Fusion), and the widely known expertise on printhead production for 2D printing, printhead and inks development. MetalJet S100 was finally launched on the market on September 2022, including a full solution for the printing and processing of BJ green parts (**Figure 4.2**).

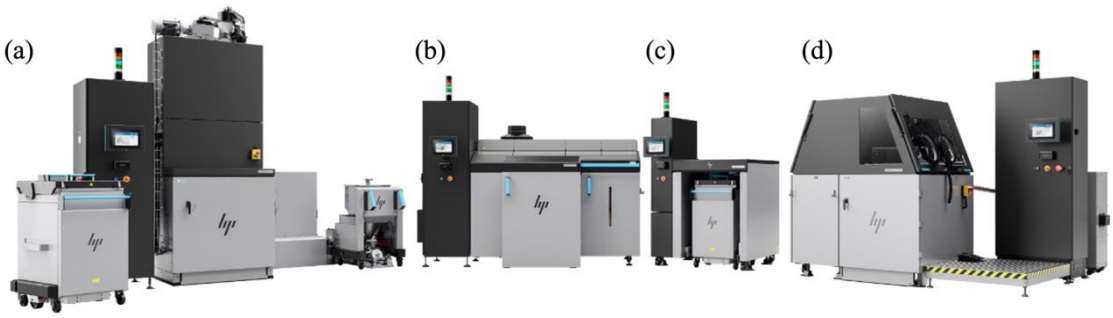

***Figure 4.2**: MetalJet S100 BJ solution. (a) Powder management station; (b) Printer; (c) Curing station; (d) Automatic decake module (provided by HP Printing and Computing Solutions S.L.).*

4.2.1 Powder management

A usual step followed by HP Inc. once the powder is received is to precondition it for stability. This process consists in a heat treatment in air. Then, it is placed in the feeding plat- form where it will be dragged by the recoating system in the course of printing to form the layers. Afterwards, the remaining powders from the feeding platform and the overflow are saved for future jobs. The powder separated from the printed parts during decaking is sieved to reject agglomerates and stored.

During the print cycle, three different powder samples of 50 g were collected with a spatula to track the evolution of its physical properties throughout the process. First, a sample is taken from the remaining powder of the feeding platform after printing. A second specimen is grabbed from the unused powder present in the center of the build bed exposed to the printing test and finally a sample is collected after the cycled unused powder is sieved. This gathered samples are respectively referred to as Load, Unpacked and Sieved. With the purpose of analyzing the general effect of powder cycling on its properties, the results shared in the mentioned section include powder collected in parallel investigations that also used this powder batch.

4.2.2 Recoating

The spreading system is formed by a recoater that moves in the Y direction, allowing a highly controlled spreading process.

Furthermore, two powder feeding platforms are located at each side of the Y axis, enabling bidirectional recoating. This significantly enhances productivity.

4.2.3 Printing

MetalJet printer beta prototype has a build bed of 430 x 309 x 140 mm. The equipment operates with three HP thermal inkjet printheads to deliver the binder. This drop-on-demand printheads work through thermal pulses that allow for a good control of the jetted droplets and are capable to print with a 1200 × 1200 dpi resolution. Details of the printhead structure showing the print bars and the nozzles in each of them are visualized in **Figure 4.3**.

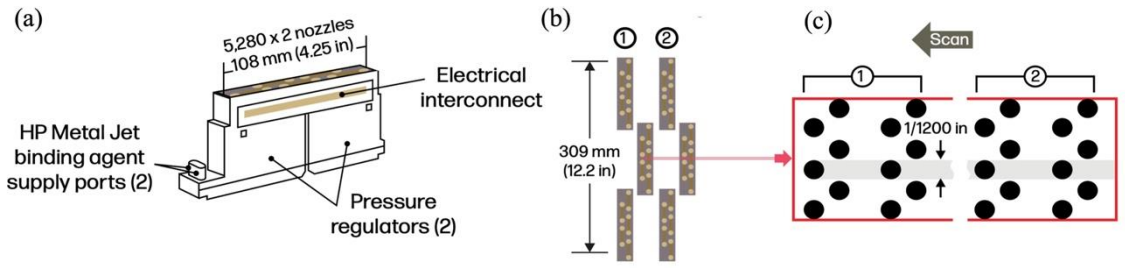

***Figure 4.3**: HP Thermal Inkjet Printhead. (a) Printhead; (b) Print bars disposition; (c) Nozzles disposition and spacing (provided by HP Printing and Computing Solutions S.L.).*

During printing, a set of heating top lamps uniformly heat the powder bed to remove the binder vehicles, through an extraction system.

In this research, the contone level will be discussed. Contone, or continuous tone, is a term employed in the printing industry and it refers to the ink (in the current case, binder) quantity employed in each printing position within a continuous range, typically from 0 to 256. The positions at which binder is jetted are determined by the contone matrix. This matrix translates the part information from the CAD or STL file to an image formed by ordered dots with variable sizes (or contone levels). Contrarily to the commonly used binder saturation, the contone level is a direct measurement of the binder jetted onto the powder bed. The advantage of using this parameter is that it does not

depend on the printing process (packing rate, powder bed perturbation, particle agglomeration or infiltration mechanisms), which makes it a better candidate for different materials or systems comparisons. Overall, the contone level is measured as the percentage of the created contone matrix covered by the binder. Assuming a packing rate of 40 % and a static powder bed, a 100 % contone level would translate to a 66 % binder saturation.

4.2.4 Curing and decaking

The curing takes place after the green parts have been produced. It consists on a thermal process that confers an additional strength to the parts. After curing, the parts are separated from the powder bed during the decaking step.

4.3 Sintering

All green parts in this work were fully densified in a furnace (MIM3045, Elnik Systems) under H_2 atmosphere. The sintering profile included a previous step of debinding to eliminate the binder present in the samples. The profile was chosen based on HP recommendations.

4.4 Characterization

In this section, the characterization techniques employed are discussed. The section is subdivided into the analysis of the powder properties, the green and sintered parts macro-properties and finally, their microstructure.

4.4.1 Powder properties

Each investigation included an initial analysis of the powder properties. First, morphology was characterized by SEM (JSM-IT100, Jeol). The powders´ skeletal density was measured with a pycnometer (AccyPyc II, Micrometrics Instruments Corporation) and compared to the theoretical density calculated from its composition. Also, in the larger investigations including several print jobs, the powder properties were tracked along the powder management cycle. Measurements of the particle size distribution along the process were carried out using a laser diffractometer (LA-960, Horiba), aiming to detect any possible shift.

The appropriate technique to characterize flowability should provoke the same stress state as the one under which the powder will be processed. For 3D printing, this is a dynamic state [55]. For this reason, the avalanche test (Granudrum, Granutools) was applied for flow behavior characterization. The results were also combined with tapped

density test (GranuPack, Granutools), as well as with shear cell tests (Powder Flow Tester, Brookfield) to be able to compare with the current available literature.

The powder cleanliness was evaluated by surface tension tests (Force Tensiometer K100, Krüss) and hydrophobicity tests.

4.4.2 Macroscopic properties

After printing, each part was inspected visually. Any external defect was noted and compared to a previously existing library of common HP MetalJet printing visual defects.

Dimensional accuracy was determined from transverse rupture strength (TRS) geometries with the help of a 3D scan robot (GOM ScanCobot, GOM) which makes use of an ATOS Q sensor to produce 3D files of the analyzed geometry. The measurements of interest are those corresponding to the X, Y and Z build directions. The obtained values for these dimensions were then subtracted to the nominal, set in the original CAD file, to obtain the dimensional deviation. To further reduce variability from different nominal lengths and parts orientation, only the largest length was considered for the analysis and only TRS bars with same main orientation were compared between them.

The green flexural strength of TRS bars printed in the build direction (Z direction) was characterized following the ASTM B312-14 standard with a Universal Testing Machine (Zwick AllAround Z050, ZwickRoell) [130].

To conclude, density measurements of green parts were performed by combining the 3D scan data with the weight of the samples (Mettler Toledo Scale Density). For more complex parts like the cylinders, the 3D scan data was combined with caliper measurements. However, the results will focus on the TRS bars density to avoid unwanted differences coming from varying shape factors. The Archimedes method was employed following the ASTM B962-13 standard for the measurements of sintered density (Mettler Toledo Scale Density) [131].

4.4.3 Microstructure

Microstructural characterization was performed using a set of complementary techniques, which are described in detail below.

Optical Microscopy (OM)

OM is a common and fast visualization technique. In metallurgy, it is used to examine features like porosity, grain size or, by combining with etching, phase analysis. OMs work by emitting light onto a specimen, and then capturing the reflected or transmitted light to create a sample image [132]. Several objective or ocular lenses are used to magnify the object, reaching a resolution in the micrometer range. In this work, an MM-400 OM (Nikon) microscope was employed to characterize the porosity of sintered samples (**Figure 4.4**).

***Figure 4.4**: OM apparatus used in the present work (MM-400, Nikon).*

Imaging was performed on cross sections of the manufactured parts that were prepared by diamond wire cutting followed by grinding and polishing with an automatic polisher (Tegramin-25, Struers). The **Table 4.3** summarizes the sample preparation steps.

***Table 4.3**: Sintered sample preparation steps for OM visualization.*

Step	**1**	**2**	**3**	**4**
Description	Grinding	Polishing	Polishing	Polishing
Surface	SiC paper	MD-Largo	MD-Dac	MD-Chem
Abrasive	#220	Diamond, 9 µm	Diamond, 3 µm	Silica, 0.04 µm
Suspension	Pure water	DiaPro Largo	DiaPro Dac	OPS non-dry
Speed (rpm)	300	150	150	150
Force (N)	40	30	30	15
Time (min)	3.5	5	4	8

Scanning Electron Microscopy (SEM)

SEM is an advanced microstructural characterization technique that allows to achieve a resolution up to the nanometer scale, permitting a more detailed description of the microstructures under investigation than OM.

The SEM working principle is based in the interaction between electrons and the sample. To begin, an electron beam needs to be formed. To this purpose, SEMs can employ two different sources. The first, thermionic sources, are based on the application of heat to release electrons from a material. This is the case of the commonly employed tungsten filaments. The second, field emission sources, also known as field emission gun (FEG) use an electrostatic field to produce the electrons. The electrostatic field is applied to a tungsten tip or wire, which, consequently, releases high-energy electrons. The electron emission areas of thermionic sources are in the order of the micrometer scale while for the field emission sources, they can reach the nanometers. This translates into a significant enhancement of the achievable image resolution in FEG-SEMs [133].

Once the electron beam is generated, a magnetic system is utilized to direct the beam towards the sample. As a result, several interactions take place between the generated beam of electrons and the electrons present in the sample. As a result of these

interactions, electrons with different energies and X-rays are emitted. These emissions are, in turn, collected by different detectors, which provide images with contrast related to surface relief, atomic number, composition, etc. The **Figure 4.5** summarizes the different signals emitted by the sample following the electron beam impact.

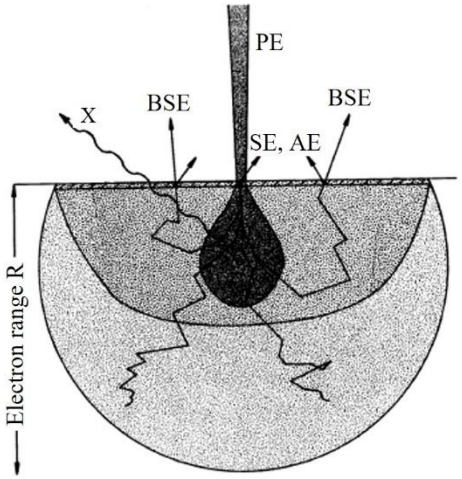

***Figure 4.5**: Principal electron (PE) interaction with matter taking place in an SEM. Secondary electron (SE), backscattered electron (BSE), Auger electron (AE) and X-rays (X) interaction depths* [133].

The current work focused on the information provided by SE and BSE electrons. SE are produced by inelastic interactions. Such interactions happen when an electron of the incident beam excites an electron in the atoms of the sample, and as a result, the electrons lose energy.

BSE are formed by the elastic interaction of the incident electrons with the atoms present in the sample. Such interaction depends significantly on the atomic number of the element interacting. Heavier atoms contain a stronger positively charged nucleus, thus, there is a higher probability of electron backscattering. This is translated to the obtention of phase-contrast micrographs in multi-material samples with a significant difference between the atomic numbers of the existing elements. This feature had a major impact in the present work, allowing the detection and quantification of the binder in green samples.

Three different SEM microscopes were employed in this work. The imaging parameters used to obtain good contrast between particles and binder were adjusted to the achievable image resolution in each one of them. **Table 4.4** lists the SEMs models as well as the corresponding imaging parameters.

***Table 4.4**: SEMs used in this work, their respective emission source, and the imaging parameters for the binder characterization.*

Equipment	Emission source	Imaging parameters
IT 100, Jeol	Thermionic	5 kV, 0.60 nA, 100 x
Helios NanoLab 600i, FEI	FEG	5 kV, 0.69 nA, 150 x
Apreo 2S, Thermofisher	FEG	2 kV, 0.10 nA, 150 x

In the current work, SEM was mainly utilized for the characterization of green parts. The specimen´s cross sections were prepared by cutting with a diamond wire saw

followed by grinding with P500 abrasive paper during 5 s. The **Figure 4.6** illustrates the three SEMs employed in the course of this work.

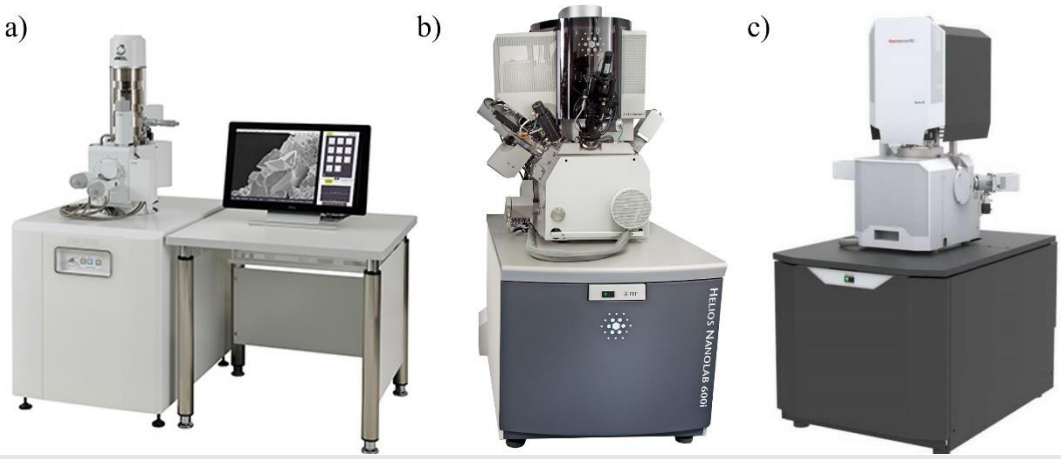

***Figure 4.6**: SEM equipment employed in the current work; a) IT-100, Jeol; b) Helios Nanolab 600i, FEI; c) Apreo S2, Thermofisher.*

X-ray Computed Tomography (XCT)

XCT is an advanced characterization technique that is used to characterize internal defects, like porosity, and complex part´s dimensions.

XCT technology is built on the interactions occurring between an X-ray beam and the sample under investigation. The X-ray beam is generated by focusing an electron beam on a target, generally made of tungsten or molybdenum and it is later redirected towards the specimen. The energy of the X-rays going through the sample will be reduced based on the specific material attenuation coefficient. The transmitted X-rays are captured by a flat panel detector which generates a grayscale image [134]. The resulting intensity after the interaction between the X-rays and the sample (I) can be calculated following the Beer-Lambert law **(4.1)**.

$$I = I_0 e^{-\mu x} \qquad \textbf{(4.1)}$$

Where I_0 is the initial intensity of the photons, μ is the attenuation coefficient of the material and x, the distance travelled by the beam in the sample or depth of the material. One of the reasons for the high complexity of XCT technique is the large amount of variability sources within this formula. Amongst others, the initial X-ray beam intensity depends on several parameters such as the filament and target material conditions. Also, complex geometries with varying thicknesses will result in larger number of photons going through thinner regions. For this reason, a cylindrical geometry is generally preferred [135].

In radiology, only a single projection is required. On the contrary, XCT employs multiple projections from different material angles that can later be reconstructed into a 3D volume of the scanned specimen. To this end, tomographs have a rotating platform between the beam source and the detector, where the sample is positioned.

Volume reconstruction algorithms use the 2D information obtained in the projections from the attenuated X-rays to calculate the 3D position of each pixel of the

sample by back-projecting and integrating the Beer-Lambert equation. There exist several algorithms to perform XCT reconstruction, however, filtered back projection continues to be the most commonly used [134].

In this work, two different XCT systems were used. The corresponding imaging and reconstruction parameters ¡ were adapted to optimize the resulting grayscale image of each equipment and resolution (**Table 4.5**). A 0.2 mm thick Cu filter was used in all cases to remove low energy X-rays.

***Table 4.5**: XCT equipment used in this work, resolution and imaging and reconstruction parameters.*

Equipment	Resolution (µm/pixel)	Imaging parameters	Reconstruction parameters
Phoenix Nanotom S, GE	1.63	130 kV, 60 µA, 500 ms	8.5 BH* correction Inline median filter
	4 – 5	130 kV, 60 µA, 500 ms	8.5 BH* correction Inline median filter
XTH 225, Nikon	1.70	130 kV, 50 µA, 0.707 Hz	3 BH* correction Inline median filter
	5.50	130 kV, 23 µA, 0.707 Hz	3 BH* correction Inline median filter

*Beam hardening

In the present work focused XCT was utilized to characterize the porosity of green samples. Initially, 4 different resolutions were employed in 4 different sample sizes to determine the optimum resolution and size for different purposes (**Section 4.5.1**). The sample´s size had to match the required resolution; thus, bigger samples were prepared by choosing a representative volume and cutting it with a diamond wire saw. **Figure 4.7** shows the two tomographs employed.

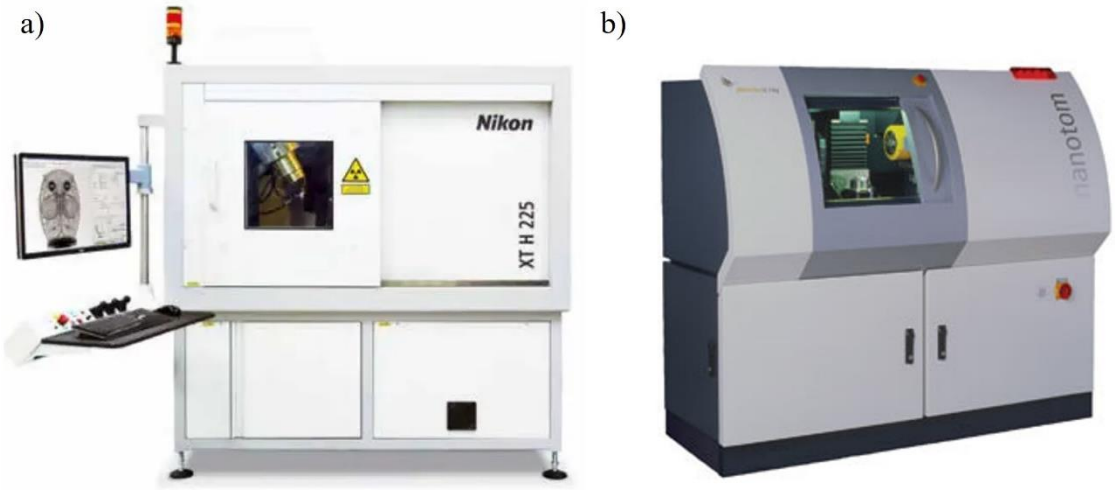

***Figure 4.7**: Tomographs utilized; a) XTH 225, Nikon; b) Phoenix Nanotom S, GE.*

4.5 Quantitative microstructural methods

Binder jetting microstructural characterization supporting serial parts production requires a quantitative and robust methodology, which is currently underdeveloped. Nevertheless, as the binder jetting industry grows, the need of scalable and automated methodologies becomes more evident. In this work, three novel methodologies have been developed to enable the quantitative characterization of an elevated number of samples. These approaches headed to agile methods to draw significant conclusions in this research, impacting the print mode development. Next, each one of the advanced procedures is explained in detail.

4.5.1 Porosity metrics development from XCT volumes

XCT-sampled volumes contain relevant information of the sample´s porosity. However, extracting this information is very complex due to the involvement of advanced image treatment algorithms and to the gray-scale variability of the original slices [134]. Consequently, a generalized and automated method facilitating the obtention of porosity data is preferred. In this section, an image treatment methodology is suggested to address this matter. The proposed method is subdivided in three parts: choice of resolution to scan a given volume, volume preparation procedure, and porosity analysis.

Size and resolution trade-off

Several cylinders with varying diameters were scanned in order to clarify how the extracted volume information depends on the utilized geometry and hence, on the achieved resolution.

Figure 4.8 shows four scanned and aligned volumes of green parts, pending to be further densified through sintering, printed with the same printing parameters. Resolution of the volumes increases from left to right with the decrease of the analyzed parts diameter. As it can be stated, the usage of high resolutions in XCT is valuable not only to obtain more precise global porosity information, but also to collect data about the particle distribution across the specimen.

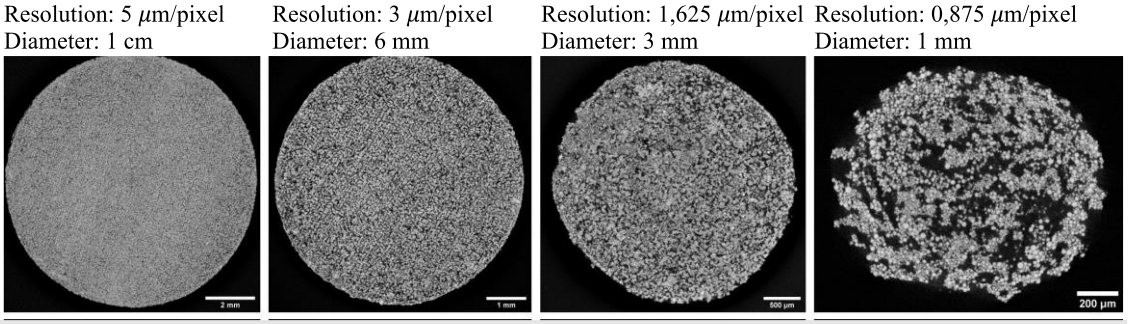

***Figure 4.8**: Size and resolution trade-off in XCT scanned BJ green parts. XY planes.*

There are drawbacks when using such a high resolution. First, the required amount of scan time practically doubles, this would suppose an inconvenient when this analysis

is coupled with production and there is a necessity to obtain results in a quick manner. Secondly, the analyzed volume is restricted to a very small size which might not be representative of more commonly printed parts or of a whole volume in a case where the sample was cut. For this reason, cylinders with a diameter of 3 mm and an achievable resolution of 1.63 µm were preferred to carry out deeper characterization through XCT. However, lower resolutions of 5.5 µm/pixel were also employed for faster investigations linked to industrial parts production.

Volume preparation

After scanning and reconstructing the volumes, the gray level histogram is homogenized by applying a brightness and contrast conditioning, followed by a volume alignment. The brightness and contrast homogenization serves to overcome the gray-scale differences generated by the X-ray intensity variation between measurements. The employed homogenization algorithm (developed at IMDEA Materials) relocates the initial 16-bit range of gray values to a new 8-bit range based on user input. To determine the input, an initially acquired volume is turned from 16-bit to 8-bit. The 8-bit volume is used to resolve the peaks corresponding to material and void and the deviation of each peak. A region of interest (ROI) is created for each component to apply the selected homogenization values.

The volume alignment is a useful step in binder jet XCT volumes for correctly identifying the XY, XZ and YZ build planes, in which most of the process related features can be detected. This procedure can be performed through visualization of the volume and manual orientation. However, an automation of the alignment is desired to minimize operator time and reduce the user- dependency of the procedure. To this end, the Fast Fourier Transform (FFT) is employed to detect a 2D repeated defect, e.g., layering, which existence is a requirement for running an automated alignment. The steps followed for the procedure are visualized in the **Figure 4.9** and are the following:

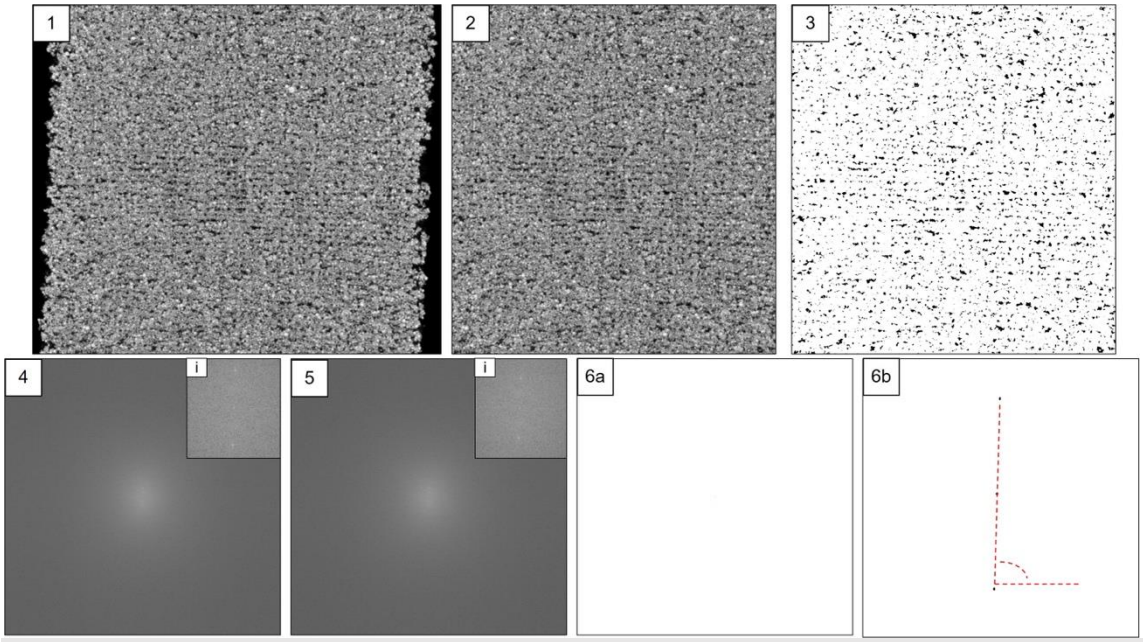

***Figure 4.9**: Volume alignment methodology in a not yet densified green part (1) XZ slice of the volume; (2) Cropped slice without background; (3) Segmented slice through Sauvola filtering; (4) FFT processed image with 4(i) detail of the peaks in the center; (5)*

FFT processed and scaled image with 5(i) detail of the peaks in the center; (6a) Segmented image through percentile thresholding (6b) Detail of the center of the segmented image showing the peaks.

1. Slices of the planes showing the 2D pattern are obtained from the volume at different heights to account for variability along the part. In the case of interest, these are the XZ and YZ planes.

2. The obtained images are cropped to remove background that could affect the subsequent segmentation and FFT processing.

3. The cropped image is converted to 8 bit and a local thresholding segmentation of the images is performed. The Sauvola filter is applied with radius 50 and parameters 1 and 2, 0.7 and 128 respectively. This segmentation contributes to limit the results from the FFT to pore and material patterns.

4. The FFT is applied. The resulting image is a grey scale figure in the Fourier domain with peaks corresponding to the angles and frequencies of the layering.

5. Next, the FFT is scaled from 2048 x 2048 to 8192 x 8192 to increase the achievable resolution of the angle formed between the peaks. This requires a bicubic interpolation to calculate the values of the added pixels.

6. A percentile thresholding is applied to detect the maximum values of the grey image. The analysis of the remaining points leads to the extraction of the angle of rotation necessary to align the volume.

The acquired angle is employed to rotate the original image in the perpendicular direction (Y) to the observed plane (XZ plane). To align the sample a second direction independent from the first one was rotated following the previous procedure. In this case, the second plane employed to extract the angle was the YZ plane, where layering was also noticeable, thus, its corresponding rotation direction was X.

The **Figure 4.10** exhibits the three planes of an analyzed volume before and after automatic alignment.

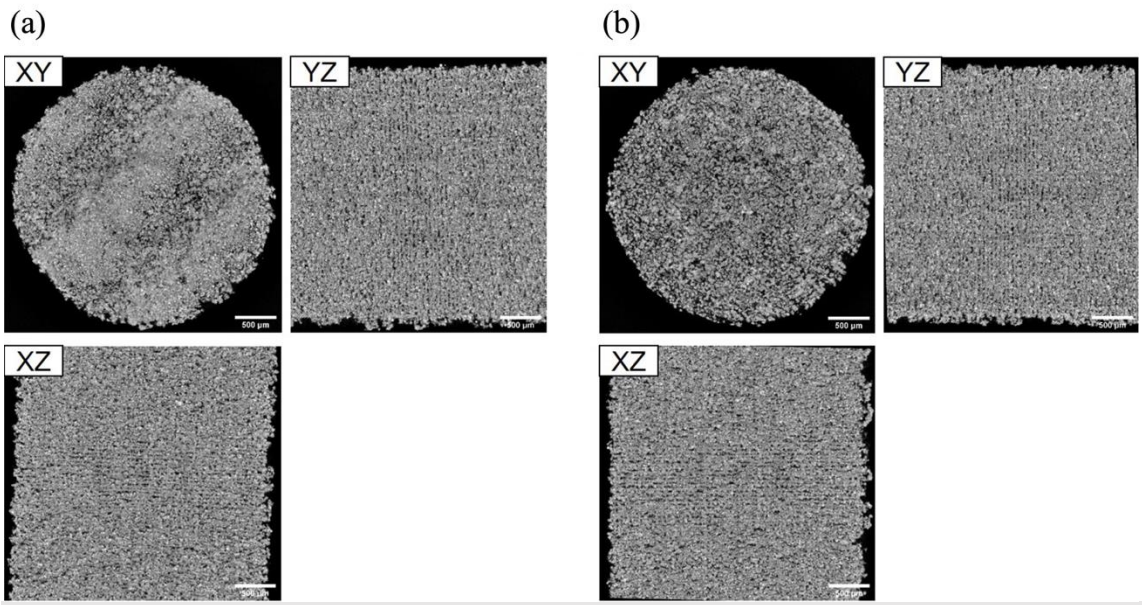

***Figure 4.10**: XCT volume with 2D pattern automatic alignment (A) Volume without alignment; (B) Volume after alignment.*

After the volume pre-treatment, a local thresholding Sauvola algorithm implemented in Fiji was employed to segment the material and porosity [136]. The Sauvola algorithm employs the equation **(4.2)**:

$$pixel = pixel > mean \times \left[1 + k \times \left(\frac{standard\ deviation}{r - 1}\right)\right] \quad \textbf{(4.2)}$$

Where pixel is the original gray-scale pixel value, mean and standard deviation are the statistical measurements of the surrounding pixels within a selected local radius, k is the parameter 1 and r the parameter 2. A radius of 30 pixels was defined, and a k and r values of 0.7 and 128 respectively, based on the existing features sizes.

Porosity analysis

After segmentation, porosity can be visualized and analyzed. Two types of analysis are suggested, a Z-directional analysis and a pore channel size distribution analysis. The Z-directional analysis has the objective to quantify the impact of the layering defect on the sample. The porosity percentage is evaluated in the printing direction, taking advantage of the previously aligned volume and the layering pattern observed. An example of this analysis is shown in the **Figure 4.11**.

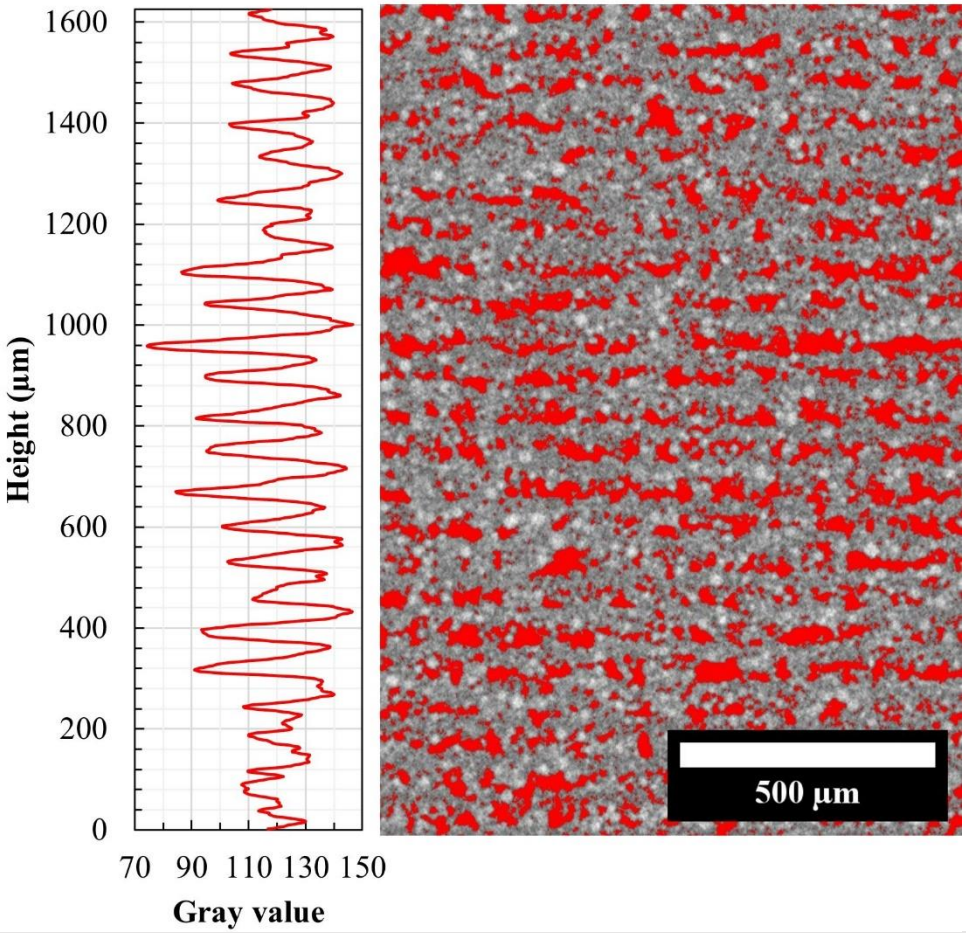

Figure 4.11: *XCT volume directional analysis.*

The analysis of the observed oscillating pattern of porosity can provide quantitative metrics that can further be compared to other volumes. These metrics can easily be extracted with a Fourier analysis of the resulting porosity pattern along the Z-axis. The **Table 4.6** describes the obtained metrics in more detail.

Table 4.6*: Porosity distribution metrics.*

Metric	Definition
Porosity amplitude	Amplitude of the sinusoidal pattern of porosity. Quantifies the severity of the layering defect.
Porosity period	Period of the sinusoidal pattern of porosity. Relates to the layer thickness and to the porosity formation origin.
Interconnectivity (%)	Fraction of the total porosity occupied by the biggest pore.
Porosity (%)	Global porosity percentage of the segmented volume.

A common examination performed on XCT porosity data is the pore size distribution analysis [109], [129]. Such analysis brings information on the distribution of pores sizes in the volume and their individual morphologies. A strategy to acquired similar information is the utilization of wall-thickness analysis over the pore´s channels of the volume. The wall-thickness analysis is generally employed for the dimensional characterization of complex parts [137], [138]. VGStudio software from VolumeGraphics

was used to run this evaluation [139]. For the analysis, each individual pore is considered as an entity, thus, a distribution of the pores channels sizes is obtained [140]. The wall-thickness analysis method fits many maximum circumscribed spheres inside and along the pore walls and returns the porosity volume colored according to the spheres´ diameters fitting the channel (**Figure 4.12**). Additionally, a data file containing a histogram of the sphere´s diameter is provided.

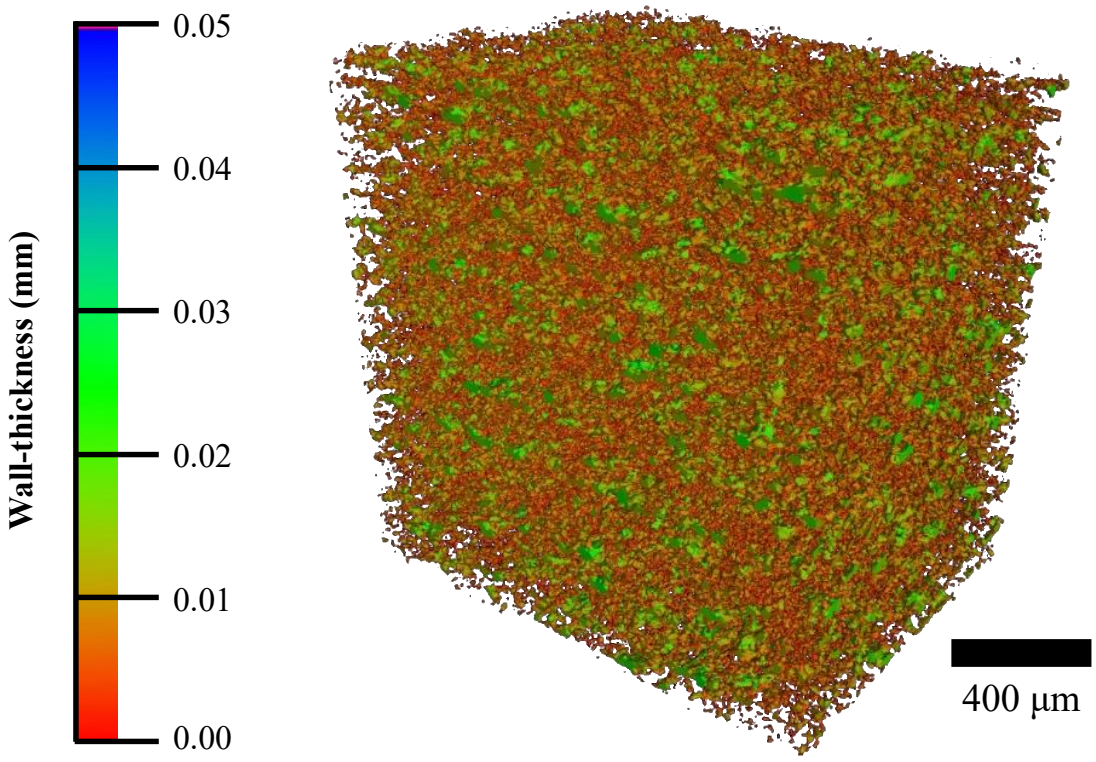

***Figure 4.12**: Porosity wall-thickness analysis of an XCT segmented volume.*

4.5.2 Binder characterization through machine learning classification

Binder is responsible for the BJ green part properties since it confers strength to the parts. Its distribution on the part will define the resulting quality and can define the printing process outcome. In this section, a method for quantifying and evaluating the binder distribution in green parts is explained in depth.

The initial step is the acquisition of SEM micrographs with the BSE detector as described in **Section 4.4.3**. **Figure 4.13** shows an example of the resulting image, containing information about the three phases present in the green part, binder, metal particles and porosity.

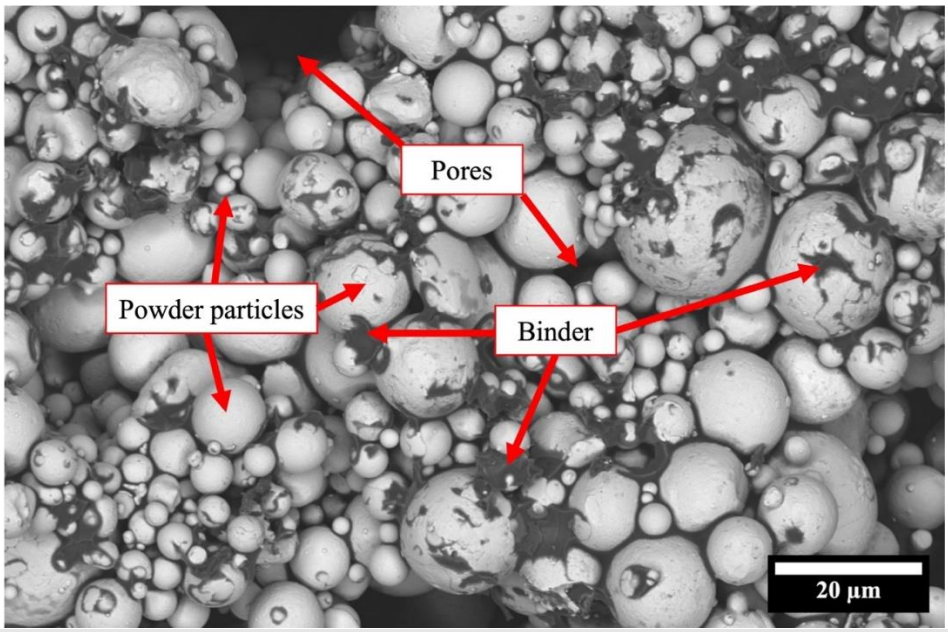

***Figure 4.13**: SEM micrograph taken with a BSE detector showing the three phases distribution in a green part.*

The attained contrast between the phases in the micrographs opens the window for further analysis methods, including the automatization of the binder distribution characterization. The followed strategy for this purpose consisted of the utilization of a pixelwise classification algorithm. Pixelwise classification is a type of machine learning algorithm consisting of the detection of image features through the information of the pixels and their surroundings, included in the analysis through several image filters [141]. First, two images containing the ground truth were manually classified to train and validate the model.

Next, the strategy to build an image classification and treatment was conducted. Initially, an image pre-treatment consisting of contrast and brightness normalization was considered. Image normalization involves rescaling the existing gray scale values of an image to the whole available range. To do so, a reassignment of each pixel gray level value is ran based on the surrounding pixels information and the selected process inputs [142]. In this specific case, a local contrast normalization was employed with a box size of 30 x 30 pixels and a 2.5 standard deviation. As it can be observed, the existing differences between the non-treated images contrast and brightness are considerably higher. Therefore, the normalized images are better suited for classification tasks.

Following, a selection of the appropriate image filters is done to include the relevant information in the classification algorithm. The selected filters considered the contribution of texture, noise, and edges between image features to the classification model [143]. They were subdivided into the following classes: first-order statistic (mean), second-order statistic (standard deviation), third-order statistic (skewness), and fourth-order statistic (kurtosis). A bank of Gabor filters was firstly convolved with the acquired SEM images through multiple kernel sizes (*e.g.*, 5x5, 7x7) using a sliding window approach. A Gabor filter is essentially a sinusoidal signal with a given frequency and orientation, modulated by a Gaussian, which boosts the texture content analysis due to its local frequency responses [144]. Afterwards, the statistical features were extracted from each convolved region. Additionally, common features including Gaussian, Median, Grey Homogeneity, Scharr, Sobel or Prewitt were also included. The sigma values

employed for these features ranged from 1 to 13, corresponding to the size range of the observable features in the micrographs.

Feature importance allows to establish which of all the selected features contributes to the model explanation in a larger extend. A pre-selection of these features allows faster computation of the classification while maintaining the classification accuracy results. Feature importance is calculated as the decrease in node impurity weighted by the probability of reaching that node [143]. The node probability is computed by the number of samples that reach the node, divided by the total number of samples. The higher the value the more relevant the feature is in the model. **Figure 4.14** shows the top 10 optimal features selected to accurately categorize porosity, binder, and particles and their relative importance. Although Gabor features did not get the highest feature importance value, it was noted that subtracting these features, result in a significant loss of the model accuracy. The values after the features indicate their specific parameters, e.g., s3 specifies a sigma value of 3 was employed. Median Gabor filter 5 was built with a $\theta = 0$, $\sigma = 1$, $\lambda = 3\pi/4$ and $\gamma = 0.05$, median Gabor feature 17 was formed with a $\theta = \pi/4$, $\sigma = 1$, $\lambda = 3\pi/4$ and $\gamma = 0.05$.

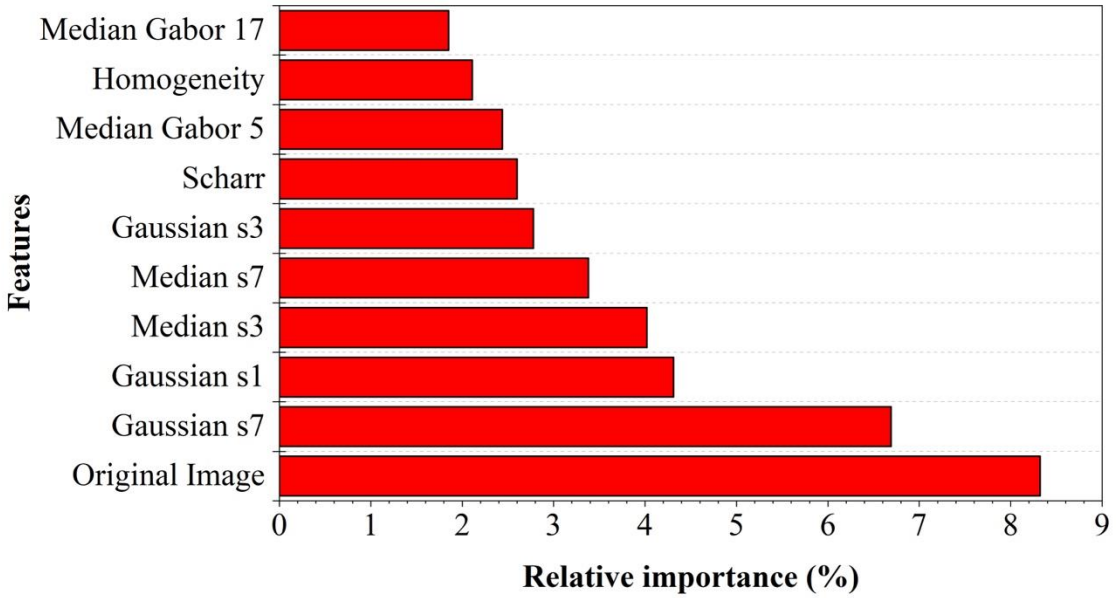

***Figure 4.14**: Selected features importance.*

The most suitable statistical features and the LightGBM classifier (implemented in Scikit-learn library of python) built the main core of the proposed algorithm. LightGBM consists of a gradient boosting framework that uses tree-based learning algorithms. LightGBM was chosen as it can handle a large amount of data, needs less memory usage, the training is fast and efficient, and the testing accuracy is usually remarkable [145], [146].

Prior to classification, oversampling was employed for the two less common classes (binder and porosity). Oversampling is a technique applied to those imbalanced datasets where there is a severe skew in class distribution. This bias in the training dataset can influence many machine learning algorithms, leading to ignore or wrongly predict the minority class. One approach to addressing the problem of class imbalance is to duplicate examples from the minority class, called oversampling. If this duplication is randomly performed is called random oversampling. A total of 250,000 data points per class were included in the training. The LightGBM classifier was then employed to

uncover the optimal features. The fine-tuned parameters for the classifier were: boosting_type = ´gbdt´, objective = ´multiclass´, is_unbalance = True, metric = ´multi_logloss´, n_estimators = 1000, reg_alpha = 0. and reg_lambda = 0.

As specified previously, the model was trained with two manually classified images of size 1536 x 225 pixels. An image window containing an 80 % of subsequent pixels (to avoid similarities between test and train data) was used to train the model, the remaining 20 % of the pixels were used to conform the validation test of the model. The final classification accuracy reached for each class is shared in **Table 4.7**. Precision is the ratio between correctly predicted positive observations and the total predicted positive observations. Recall, also known as sensitivity, is the ratio between correctly predicted positive observations and all the observations in the class. Finally, F1-score is a weighted average of the other two metrics which considers false positives and false negatives. It was experimentally noted that F1-score values can be increased by adding more heterogeneous training data to the model, i.e., more images of different samples. Binder results showed the lowest F1-score. The large majority of the misclassified pixels were found in the interphase between binder and porosity. This is expected given the low contrast attained in such locations. However, the resulting accuracy was sufficient to detect the layered pattern of the binder distribution and extract the related metrics.

Table 4.7: *Pixel-wise classification results of LightGBM algorithm.*

Class	Precision	Recall	F1-score
Binder	0.71	0.78	0.74
Porosity	0.76	0.83	0.79
Particles	0.98	0.94	0.96
Macro avg.	**0.81**	**0.85**	**0.83**
Weighted avg.	**0.90**	**0.90**	**0.90**

To finish, the classified image is used to calculate each class percentage. Also, the same procedure that was employed for the segmented volume, based on the FFT analysis, was employed to align the micrographs, and to determine the binder distribution amplitude and period.

4.5.3 Porosity of sintered parts

The porosity of sintered parts can be easily extracted from optical micrographs as stated in **Section 4.4.3**. Nevertheless, given the complexity of the printed geometries there may be a porosity gradient within the part. An image analysis method was developed to analyze such gradient.

5

PRINTING PARAMETERS OPTIMIZATION THROUGH GREEN PART CHARACTERIZATION

In this chapter the results published in a the scientific article: “Binder jetting green parts microstructure: advanced quantitative analysis” are shared. A wider version of such results is shared in the confidential version of this thesis, available on demand.

The developed characterization methods described in **Section 4.5** are employed to compare four combinations of printing parameters through the green microstructural metrics. In addition, green density measurements and porosity results from XCT were analyzed for their use in sintered density predictions.

Jobs were printed with several combinations of layer thickness and binder saturation values, which are detailed in **Table 5.1**, and at printing temperatures (temperature reached by the lamp during printing) in the range of 45-65 ^{o}C. Note that, intentionally, not optimized print modes were run in order to enable enough sensitivity for the novel methodology to identify features and develop metrics. Parts included TRS parallelepipeds (38 x 15 x 8 mm) and cylindrical bars (8 mm height 3 mm diameter). The first ones were used for the characterization of the macro-properties and SEM analysis, while the cylinders were employed for the XCT green part microstructural characterization.

***Table 5.1**: Selected combination of printing parameters.*

Part Name	Layer Thickness (λ)	Binder Saturation
A	35 µm	< 100 %
B	35 µm	> 100 %
C	70 µm	< 100 %
D	70 µm	> 100 %

5.1 SEM analysis: Binder fraction and amplitude

The local binder percentage and binder amplitude along longitudinal XZ plane sections of green parts printed with a variety of parameters is shown in **Figure 5.1**. Each point in this figure is calculated as the average of 5 images per sample in at least 2 samples per condition. In the range of temperatures studied (*45-65 ºC*) it is observed that the local binder fraction is independent of the λ, varying in between 8-19% according to the binder saturation employed. In contrast, the binder amplitude increases with the λ. Amplitudes from 0.5 to 0.9 % are associated to 35 µm and amplitudes of 0.9 to 1.1 % are associated to 70 µm. The binder amplitude is a measure of the green microstructure homogeneity and, thus, shorter amplitudes are expected in more homogeneous microstructures, which usually are associated to shorter λ [147]. The analysis also confirmed that the binder period is of the order of magnitude of λ, with values and standard deviations of 36,06 ± 3,43 µm for 35 µm layer thickness and 69,76 ± 1,11 µm for 70 µm layers.

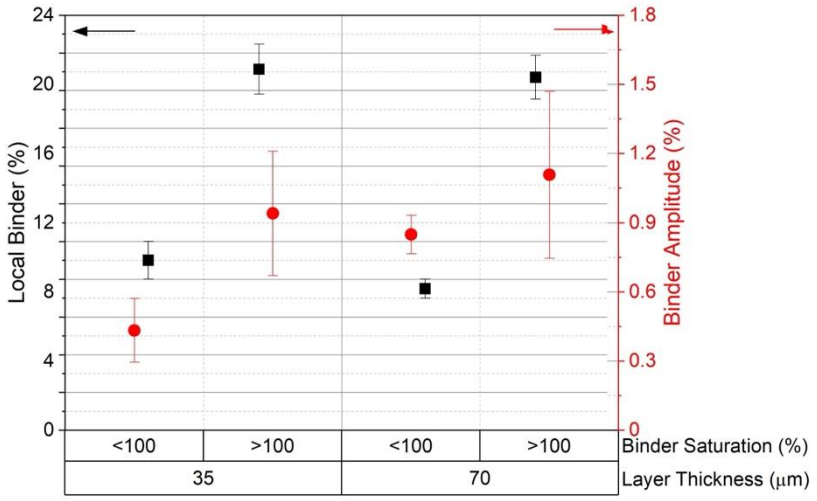

***Figure 5.1**: Local binder percentage and binder amplitude of green parts with a variety of printing parameters.*

While deviation of the binder local fraction is maintained at low values for all conditions, the amplitude deviation shows a dependance on the binder saturation

employed. Higher saturations above 100 % lead to bigger deviations near 0.4 % binder amplitude.

Figure 5.2 shows SEM green part cross sections and the corresponding segmented counterparts used to extract the microstructural metrics. A homogeneous microstructure is observed for the 35 µm λ irrespective of the binder saturation level. Similar binder amplitudes were observed for 35 µm, >100% (*Figure 7b*) and 70 µm, <100% binder saturation (*Figure 7c*). However, the observed binder fraction on the micrographs clearly differs. The layering pattern of the binder can also be identified in the case of 70 µm and >100% binder saturation, which is an exaggerated print mode example to allow microstructural metrics differences and thresholds. This particular printing parameter combination also presents pores larger than 50 µm (meso-pores).

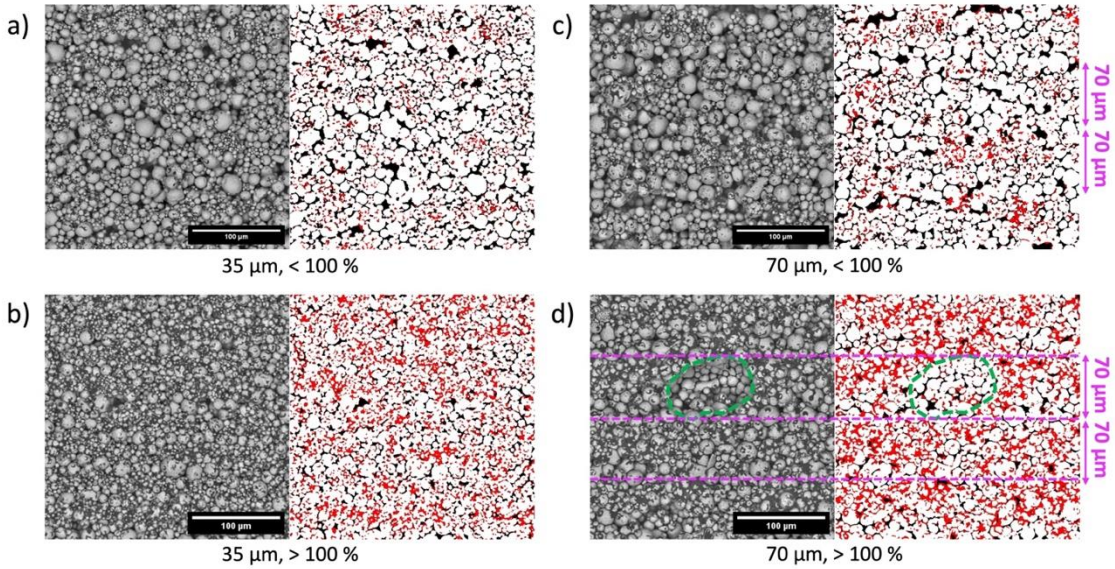

***Figure 5.2**: SEM micrographs of green parts printed in gray scale and their respective classification output in black and white contrast. Samples layer thickness and binder saturation: (a) 35 µm, < 100 %; (b) 35 µm, > 100 %; (c) 70 µm, < 100 %; (d) 70 µm, > 100 %, layering defect shown in violet dashed lines, meso-pore shown in green.*

It must be noted that the methodology allowed the identification of the binder location along a variety of particle sizes distributed along microstructure cross section. Thus, by quantifying the binder percentage along the printing direction (vertical in *Figure 7*), it is possible to identify regions of higher binder concentrations (referred to as amplitude in *Figure 3*) that are related with regions of segregation of fine particles. Moreover, the use of higher binder saturation leads to higher green densities (see *Figure 12*) but at the expense of meso-pore formation, as highlighted in *Figure 7d* in green, probably due to powder disturbances from the binder.

5.2 3D XCT analysis: Porosity fraction and distribution

Figure 5.3 illustrates the porosity percentage as a function of λ and binder saturation. The porosity is observed to increase with λ. In particular, a relative porosity of 8-11% is observed for 35 μm and of 15-28 % for 70 μm. The porosity was observed to increase as well with binder saturation, particularly for the larger λ, where it reaches values close to 30 %. The SEM micrographs of **Figure 5.2**, suggest that this might be related to the presence of meso-pores. The porosity amplitude, also depicted in **Figure 5.3**, shows analogous bimodal trends as the ones noted for the binder amplitude (**Figure 5.1**). The porosity amplitude at 35 μm is stable around 13%, irrespective of the binder saturation level. At 70 μm the porosity amplitude decreases with increasing binder saturation from 12 to 9 %. The large porosity fraction at a saturation higher than 100%, combined with a comparatively lower amplitude, is positively expected to reduce the part anisotropy.

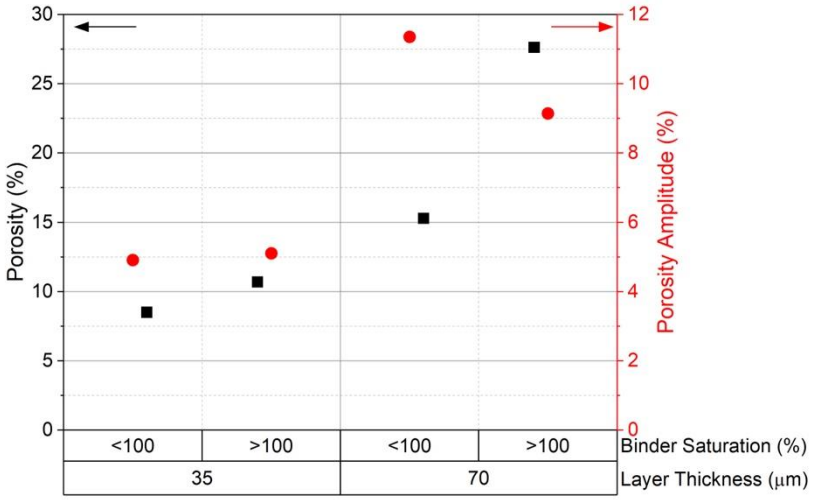

***Figure 5.3**: Porosity percentage of green parts with a variety of printing parameters.*

The XCT slices shown in **Figure 5.4** confirm qualitatively the previous quantitative analysis. A more homogeneous microstructure is noted for 35 μm (**Figure 5.4a-b**), while 70 μm layers parts (**Figure 5.4c-d**) showed very dense layers but with interlayer porosity. Secondly, for a constant λ the degree of layering increases with higher binder saturation in thin layers (**Figure 5.4a-b**), while the opposite is observed for thicker layers (**Figure 5.4c-d**).

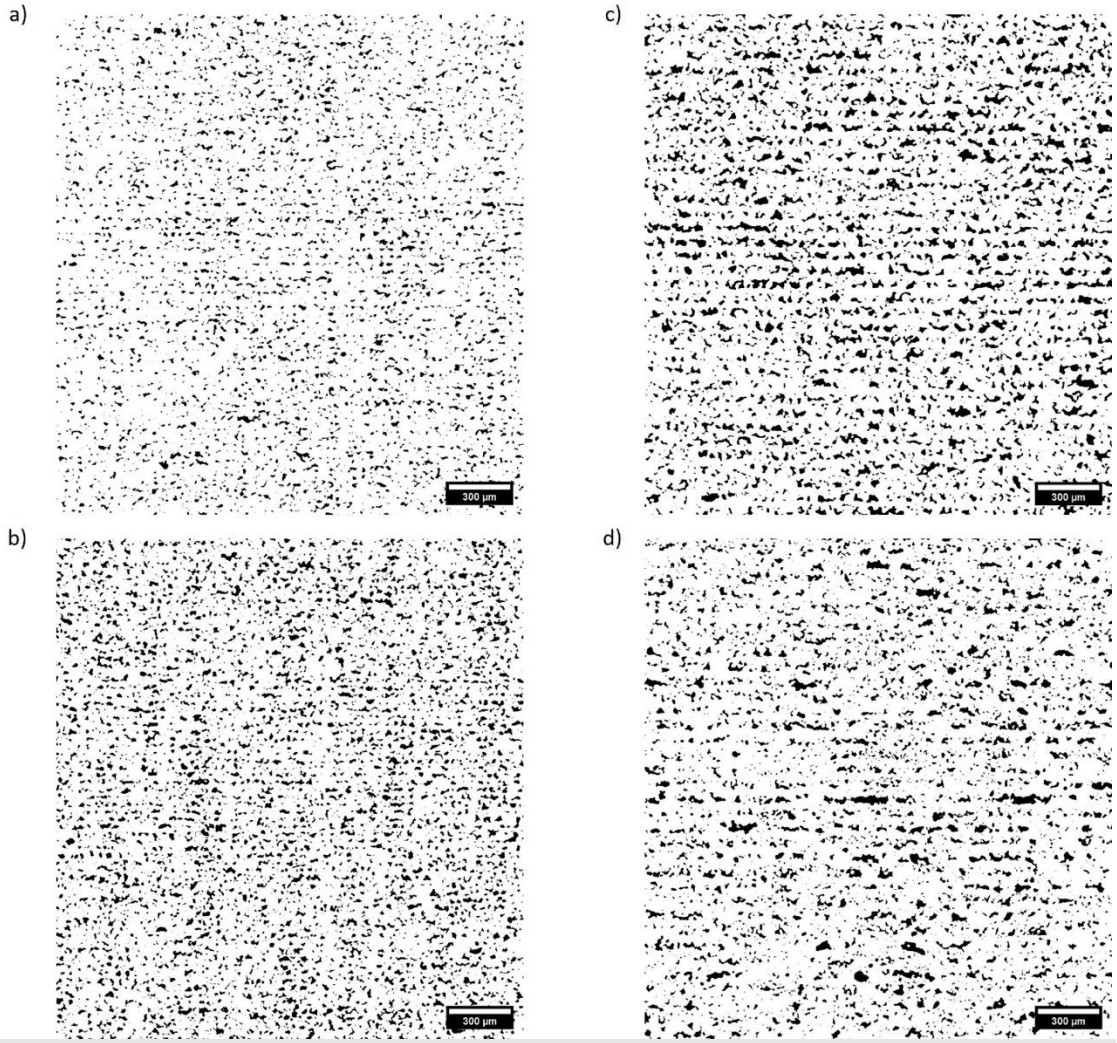

***Figure 5.4**: XCT XZ plane micrograph slices of samples layer thickness and binder saturation: (a) 35 µm, < 100 % (b) 35 µm, > 100 % (c) 70 µm, < 100 % (d) 70 µm, > 100 %.*

A 3D analysis of the pore interconnectivity reveals that it is below 50% for 35 µm parts and above 80 % for 70 µm parts (**Figure 5.5**). Thus, a pore size distribution analysis is not sufficient to characterize and compare the porosity of the samples, since most of the pore's information will be contained in a single pore.

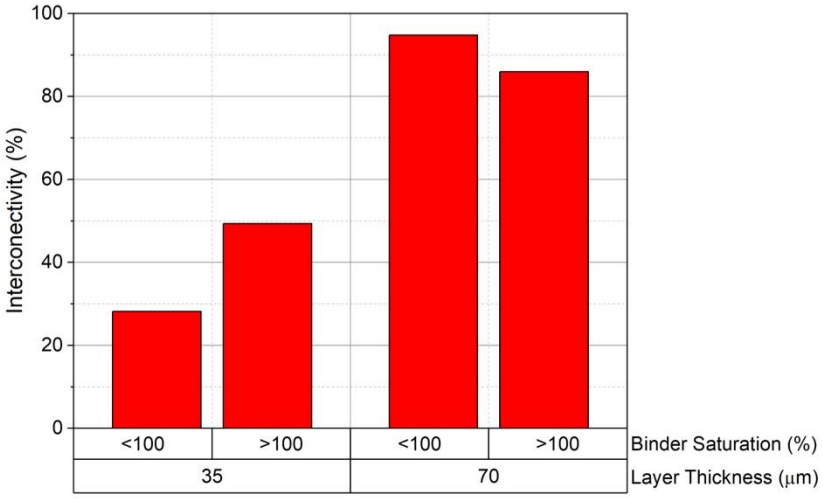

***Figure 5.5**: Interconnectivity of pores in printed green parts.*

A wall-thickness analysis of porosity was carried out (**Figure 5.6***)*. It can be observed, first, that higher relative frequency thicknesses range between 5 and 15 μm for all samples. However, a higher fraction of thicker channels is observed for 70 μm. While in 35 μm parts, the maximum value of the wall-thickness is equivalent to λ, in the case of 70 μm parts the maximum values lay below 60 μm, suggesting a relative reduction of porosity. Finally, an increase of the relative frequency of bigger channels is also noted for >100 % binder saturation at both selected λ.

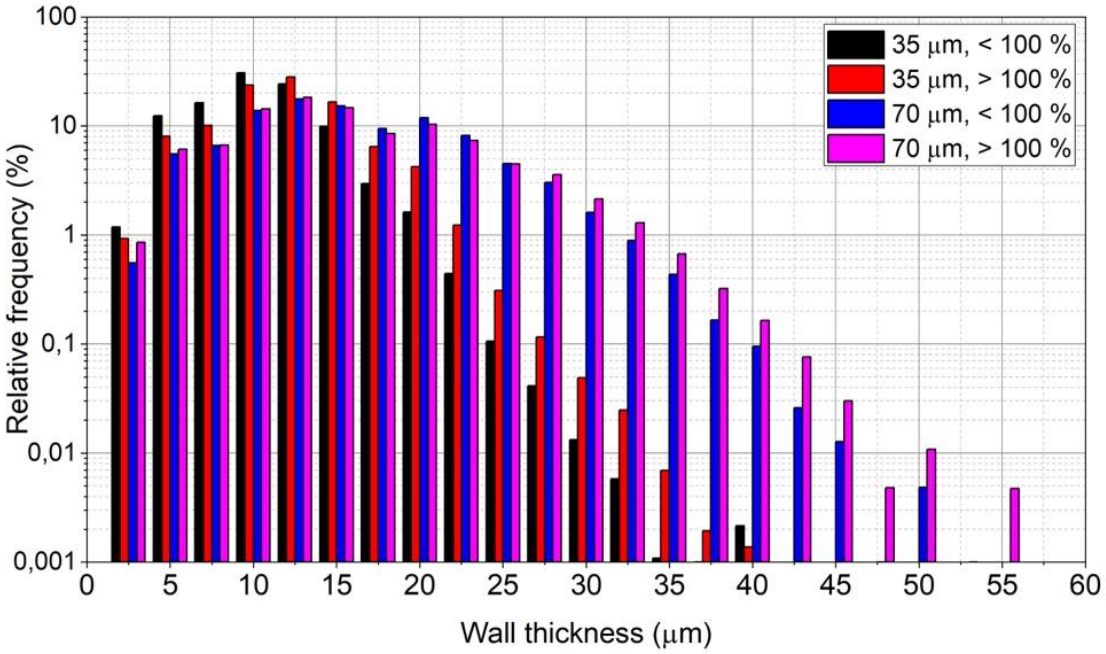

***Figure 5.6**: Porosity wall-thickness analysis of representative printing conditions.*

5.3 Density analysis

Figure 5.7 shows the green and sintered density corresponding to all the printed parts. Binder saturation appears to have significant impact on density. While a >100 % of binder saturation led to densities between 4.7-4.8 g/cm^3, lower binder saturation led to a more variable outcome with densities between 4.2-4.6 g/cm^3. Parts printed at 35 µm exhibited slightly higher sintered densities and lower sensitivity to other printing parameters in comparison to 70 µm parts.

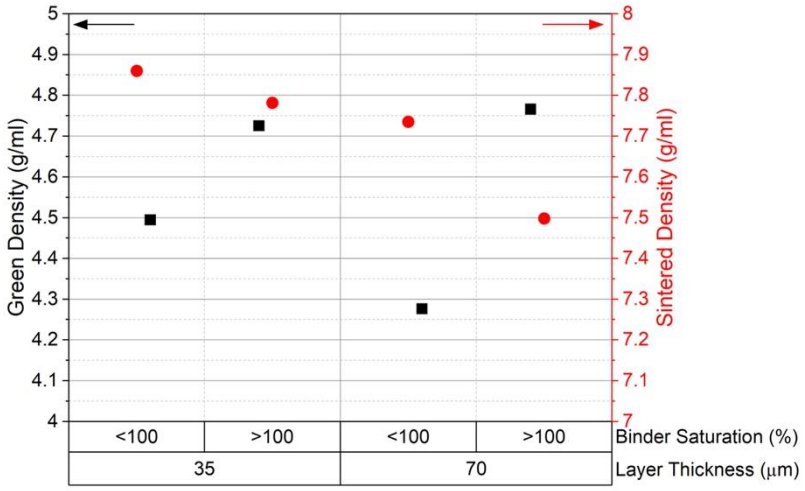

***Figure 5.7**: Green and sintered density with a variety of printing parameters.*

In summary, the microstructural analysis and metrics identification for both binder and porosities local fraction and periodicity allowed to get relative threshold values related to green and sintered density (**Table 5.2**). In particular, binder fraction observed in the cross sections were impacted only by the binder saturation. In contrast, binder amplitude was observed to increase from 0.5 to 1.1% from thinner layers and less binder saturation to coarser layers and larger binder saturations respectively. The binder amplitude is expected to be related to the infiltration of the binder during the printing process. The porosity formed also contributes to a lower infiltration due to the reduction of small channels where the binder can move through capillarity. This is why, a similar dependance to printing parameters is observed for both metrics. As homogeneous microstructures are related to those with minimum binder amplitudes, a layer thickness and binder saturation optimization could be performed considering this metric. The porosity amplitude on the other hand is a measure of the impact of the layering defect. It was observed that the main contributor to the severity of this defect was the employed layer thickness. At thick layers it has been shown that binder saturation has the potential to reduce the amplitude. Previous studies have commented on a possible compaction of the bed through the binder deposition and coalescence. These results would be in agreement. Porosity fraction and amplitude provided minimum values with a corresponding homogeneous microstructure.

***Table 5.2**: Summary of microstructure parameters, green and sintered density.*

	Binder fraction (%)	Binder Amplitude (%)	Porosity Fraction (%)	Porosity Amplitude (%)	Green Density (g/mL)	Sintered Density (g/mL)
35 µm, < 100 %	9	0.5	8	13	4.5 (56)	7.9 (99)
35 µm, > 100 %	19	0.9	11	13	4.7 (59)	7.8 (98)
70 µm, < 100 %	8	0.9	15	28	4.3 (54)	7.7 (96)
70 µm, > 100 %	19	1.1	28	22	4.8 (60)	7.5 (94)

It is important to note that, even more exaggerated heterogeneous microstructures should be generated by using even less optimized print modes to allow more intense metric signals. In this study, the quantification method enabled the identification of binder and porosity metrics with resolution enough for slight periodicity signals.

5.4 Sintered density predictability

Figure 5.8 correlates the green density and the porosity with the sintered density. A total amount of 10 samples were included in the analysis as this number allowed to balance the need to carry out a robust analysis with the time-intensive XCT characterization requirements. The R-square values, measuring the proportion of sintered density variance explained by green density and green porosity, were calculated. A very low correlation between green and sintered density is observed ($R^2 = 0.08$). The application of extreme printing conditions, such as a binder saturation above 100 %, modifies the pore size distribution of the samples. This modification is not collected in a macroscopic property like density. However, porosity in the green part is highly correlated to the sintered density ($R^2 = 0.89$). This high correlation is consistent with the fact that the smallest pores, which cannot be detected by XCT, do not represent a big impediment during sintering.

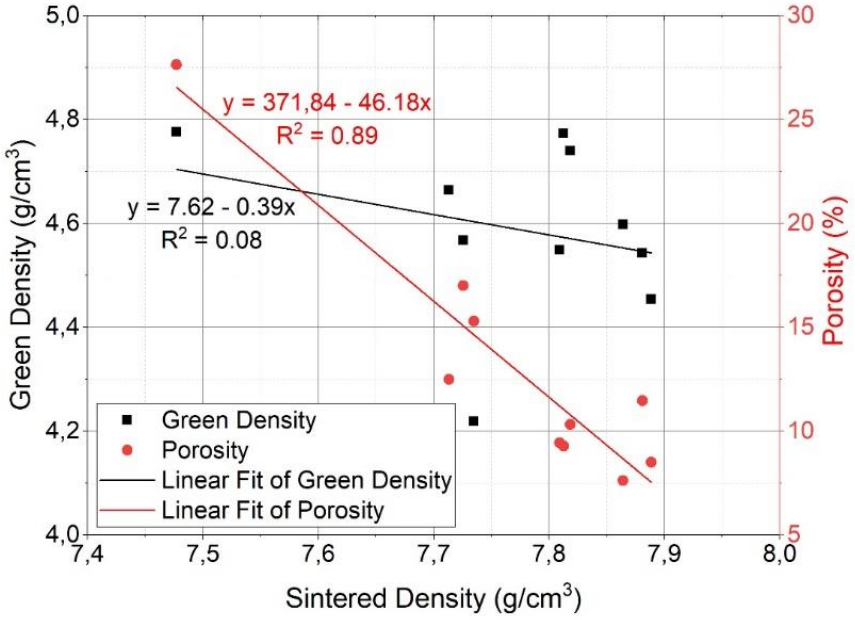

***Figure 5.8**: Green density and green part porosity relationship with sintered density.*

Additionally, the observed reduction on sintered density at a high binder saturation (**Figure 5.8**) is attributed to the detected meso-pores (**Figure 5.7**). To the contrary, >100 % binder saturation is advantageous for the green state properties, leading to higher green densities and green strength and making parts easier to handle. Strategies to reduce the size of meso-pores due to high binder saturation conditions, should be considered along print mode optimization. Also, an improvement of the sintered part quality through increased sintering time and temperature could be addressed, as proposed by Sufiiarov et al. [113]. Other alternatives to improve the sintering process is to use sintering additives or nanoparticles [11], [26]. Moreover, supplementary post-treatment like hot isostatic pressing (HIP) has been widely applied for this purpose [109]. It is also hypothesized that big pores might also be diminished by the modification of printing and curing parameters that control binder deposition and solvents evaporation. Further investigations in this direction would help to mitigate big pores formation without the addition of new process steps and variables.

Finally, amplitude values of binder and pores are key in understanding material properties anisotropy owing to the directional nature of BJ technology. While binder fraction and distribution are expected to significantly impact green strength, porosity amplitude will presumably have a larger impact on the anisotropy of the sintered state samples and their resulting microstructure [95].

5.5 Conclusions and future work

To conclude, the investigation has delivered a novel methodology to characterize green parts´ microstructures based on a periodic signal of the binder and porosity local fraction throughout the build direction. This allowed the identification of the relative metric ranges for a variety of printing parameters, which were selected aiming to assess the methodology sensitivity. Additional conclusions are:

- The developed pixel-wise classification algorithm allows to quantify green parts´ SEM micrographs and to extract relevant binder microstructural characteristics.

- Complementary, XCT characterization allowed the quantification and comparison of porosity across different process parameters combinations. A resolution of 1.6 µm is not able to resolve smaller interparticle pores. However, its potential to be used as a metric to predict the sintering outcome with great accuracy has been proven.

- The binder and porosity distribution metrics, referred to as binder and porosity amplitude, respectively, are intimately related to the layering defect describing the green part microstructure. The optimal print mode selected based on this metrics was a 35 µm layer with a binder saturation below a 100 %.

- Wall thickness analysis allowed a more optimal porosity characterization due to the high interconnectivity values.

- It has been proven that no correlation exists between the green and sintered densities (R^2 = 0.08), while the pore fraction was able to predict the sintered density (R^2 = 0.89).

Finally, future work would involve a deeper characterization of sintered parts and the exploration of the effect of both binder and porosity amplitude with sintered microstructure, anisotropy and resulting part shrinkage.

6

PART GEOMETRY EFFECT ON MICROSTRUCTURE

Binder infiltration mechanisms can be affected by the binder´s viscosity evolution upon heating. The temperatures required to jet the binder through the printhead nozzles and to control the binder´s viscosity during infiltration are very different. Because of this reason, increasing the printable region of a part, i.e., its section, can result in a larger temperature gradient. The current section aimed to investigate this matter.

To that purpose two investigations focused on a variety of part geometries were carried out. The first investigation was intentionally designed to analyze a variety of geometrical features, e.g., section size, section size evolution or feature size. The printed green parts microstructure was revealed following the characterization methods shared in **Sections 4.5.1** and **4.5.2**. From the analysis, several relationships were found. Such relationships showed a potential to build adaptative print modes that modify their parameters according to the geometry being printed.

The second investigation focused on an industrial case study consisting in a complex demo geometry. Microstructural metrics regarding binder and its distribution across a green part were compared to those obtained in a simpler TRS bar. As a result, the conclusions from the first investigation could be leveraged to a real case study

7

EDGE POROSITY ANALYSIS OF BJ SINTERED PARTS

The current chapter focused on the investigation of BJ sintered parts porosity. While most of the previously mentioned heterogeneities in green parts can be mitigated through the sintering process and post-treatments, there is a need to understand their impact over the final part densification and microstructure. The microstructural characterization method developed and mentioned in **Section 4.5.3** was employed to analyze BJ sintered parts.

Three investigations conformed this chapter. The first consisted of an initial exploration of the sintered parts porosity in different regions of the part for a variety of printing parameters combinations. It allowed for a first assessment of the differences between top, bottom, edges and center of BJ sintered parts. In general, the differences found could be reduced through the modification of printing parameters for each contour condition being considered.

The second investigation focused on the porosity distribution evaluation and its evolution across the part. Three printing parameters combinations were employed covering a range of conditions that eased the determination of the optimal print modes for each part region. The mechanisms driving sintered part porosity heterogeneities could be found and a method to mitigate them based on adaptative print modes was proposed.

Finally, an industrial case study investigation was carried out. The study was centered in the furnace part positioning impact over the minimization of porosity in sintered parts. It was found that the heterogeneous distribution of temperature during sintering in a batch furnace could lead to significant differences between final parts porosity. The optimal parts' distribution within the furnace was proposed based on OM porosity metrics. However, the origin of the problematic was linked to the design of the furnace. A further effort is proposed in this matter to ensure the correct distribution of temperature and avoid differences during final part consolidation.

8
CONCLUSIONS

The investigations carried out in this work aimed to accomplish the objectives cited in the **Chapter 3**. Therefore, the general conclusions are divided to address each proposed goal.

1. **Develop automated characterization methods that allow for metrics subtraction and comparison between BJ green parts**:

   - The lack of green part microstructural characterization in BJ 3D printing pointed towards the development of image treatment algorithms for SEM and OM micrographs and XCT volumes allowing the subtraction of relevant metrics for understanding BJ processes.

   - These algorithms were not only developed, but also employed in several studies, which proved their high sensitivity to a variety of BJ parameters, printed geometries, or sintering conditions.

   - The extracted metrics presented a high correlation with relevant process parameters, exhibiting a great potential for process predictability at different stages.

2. **Contribute to the existing knowledge of BJ printing process through the addition of a deep characterization of green parts and their respective sintered parts outcome:**

   - The **Chapter 5** explored the relationship of BJ part with some printing parameters already available in the literature. However, the addition of a new perspective combining commonly seen characterization with the

microstructural readings of the green parts allowed to get new insights into BJ printing mechanisms.

3. **Investigate the impact of part geometry, size, and features on the resulting microstructure:**

    - Part geometry was found to significantly influence the microstructural observations. A relationship was established between a variety of geometrical features and the resulting microstructural metrics.

    - The geometrical influences exploration emphasized the need for adaptative print modes that consider the previously mentioned relationships.

4. **Advance in the understanding of the surface defects relationship with the printing recipe and its link to posterior machinability:**

    - OM microstructural metrics were developed to characterize porosity gradients in BJ sintered parts.

    - Several process parameters were found to promote or hinder the formation of porosity in the sintered state. An optimization of these parameters was proposed.

    - The resulting variability of porosity metrics within the part also evidences the need for adaptative print modes the optimize porosity locally.

9
FUTURE WORK

Based on the findings of this work and the current state of the art, this chapter summarizes future development areas with a high potential to impact BJ current problematics.

The chapter specifically explored four paths of investigation. Firstly, although the layering defect can be minimized in the sintering stage, it still contributes to the green parts heterogeneities and it can also modify the shrinkage ratios in each part axis. A deeper investigation of the binder deposition parameters could help to identify critical parameters influencing porosity formation.

Secondly, the **Chapter 6** showed that the part geometry can modify the microstructural metrics developed in this work. Further studies focusing on alternative print modes that consider such variations could enhance the BJ process robustness and reduce the process variability.

Thirdly, BJ printers do incorporate some methods to track certain sub-systems stability and state, e.g., nozzles health, temperature readings, etc. [148]. Nevertheless, as the technology advances, additional monitoring techniques should be included covering topics like the layer formation defects, powder bed distortion from droplet deposition or binder infiltration. In situ monitoring cameras jointly with computer vision techniques have shown a huge potential in this area [149], [150]. Nonetheless, BJ is still in an early stage in this matter, and more investigations should be carried out to address the specific challenges that the technology faces.

To finish, BJ 3D printing whole process implies a series of steps, each one of them significantly affecting the final part outcome. In this work, it has been shown that sintered density could be linked to the present porosity in green parts. However, changes in the materials employed or the sintering parameters can significantly alter the mentioned

relationship, and thus, complicate the prediction of the final part properties. Consequently, more complex algorithms would be required to be able to generalize such predictions to new material systems incorporated in the technology.

Recently, AI has become a major subject in industry, thanks to its ability to deal with large and complex data [151]. Moreover, it has already been integrated in production facilities with reported benefits from it [152], [153]. It has also demonstrated applicability in other 3D printing technologies to predict final part properties, saving time and money in the materials development process [154], [155].

To the author´s knowledge, BJ has not yet profited from the benefits of AI to deal with the complexity of the technology. Nevertheless, the observed rise of interest in AI, leading to the development of more complex and robust algorithms, is expected to impact soon BJ capabilities. To this end, transversal studies merging AI knowledge with materials and process will surely advance BJ knowledge and industrialization.

Bibliography

[1] T. DebRoy *et al.*, "Additive manufacturing of metallic components – Process, structure and properties," *Prog Mater Sci*, vol. 92, pp. 112–224, 2018, doi: 10.1016/j.pmatsci.2017.10.001.

[2] W. Gao *et al.*, "The status , challenges , and future of additive manufacturing in engineering," *Computer-Aided Design*, vol. 69, pp. 65–89, 2015, doi: 10.1016/j.cad.2015.04.001.

[3] M. L. Montero *et al.*, "Changing the alloy composition of Al7075 for better processability by selective laser melting," *Journal of Materials Processing Tech.*, vol. 238, pp. 437–445, 2016, doi: 10.1016/j.jmatprotec.2016.08.003.

[4] M. Nastac, R. Lucas, A. Klein, and ExOne, "Microstructure and mechanical properties comparison of 316L parts produced by different additive manufacturing processes," in *28th Annual International Freeform Fabrication Symposium*, Austin, Texas, 2017, pp. 332–341.

[5] P. Bajaj, A. Hariharan, A. Kini, P. Kürnsteiner, D. Raabe, and E. A. Jägle, "Steels in additive manufacturing: A review of their microstructure and properties," *Materials Science and Engineering A*, vol. 772, p. 138633, 2020, doi: 10.1016/j.msea.2019.138633.

[6] M. Ziaee and N. B. Crane, "Binder jetting: A review of process, materials, and methods," *Addit Manuf*, vol. 28, pp. 781–801, 2019, doi: 10.1016/j.addma.2019.05.031.

[7] 3DAdept, "Comparing the potential & limitations of binder jetting and MIM. [Accessed: 07 June 2020]: https://3dadept.com/comparing-the-potential-limitations-of-binder-jetting-and-mim/," *3DAdept*, 2019. https://3dadept.com/comparing-the-potential-limitations-of-binder-jetting-and-mim/ (accessed Apr. 07, 2020).

[8] E. M. Sachs, J. S. Haggerty, and P. A. Williams, "US Patent. Three dimensional printinig techniques," 5204055, 1993

[9] G. C. Dumitrescu and I. A. Tanase, "3D Printing – A New Industrial Revolution," *Knowledge Horizons - Economics*, vol. 8, no. 1, pp. 32–39, 2015.

[10] B. Jackson, "HP Metal Jet launches at IMTS 2018, technical specifications and pricing. [Accessed: 07 June 2020]: https://3dprintingindustry.com/news/hp-metal-jet-launches-at-imts-2018-technical-specifications-and-pricing-139440/," *3D Printing Industry*, 2018. https://3dprintingindustry.com/news/hp-metal-jet-launches-at-imts-2018-technical-specifications-and-pricing-139440/ (accessed Apr. 07, 2020).

[11] L. Sun, Y. H. Kim, D. Kim, and P. Kwon, "Densification and properties of 420 stainless steel produced by three-dimensional printing with addition of Si3N4 powder," *J Manuf Sci Eng*, vol. 131, no. 6, pp. 0610011–0610017, 2009, doi: 10.1115/1.4000335.

[12] C. Y. Yap *et al.*, "Review of selective laser melting: Materials and applications," *Applied Physics Reviews*, vol. 2, no. 4. American Institute of Physics Inc., Dec. 01, 2015. doi: 10.1063/1.4935926.

[13] K. Kempen, F. Welkenhuyzen, J. Qian, and J.-P. Kruth, "Dimensional accuracy of internal channels in SLM produced parts," 2014. [Online]. Available: https://www.researchgate.net/publication/262698461

[14] D. S. Shim, G. Y. Baek, J. S. Seo, G. Y. Shin, K. P. Kim, and K. Y. Lee, "Effect of layer thickness setting on deposition characteristics in direct energy deposition (DED) process," *Opt Laser Technol*, vol. 86, pp. 69–78, Dec. 2016, doi: 10.1016/j.optlastec.2016.07.001.

[15] D. G. Ahn, "Directed Energy Deposition (DED) Process: State of the Art," *International Journal of Precision Engineering and Manufacturing - Green Technology*, vol. 8, no. 2. Korean Society for Precision Engineeing, pp. 703–742, Mar. 01, 2021. doi: 10.1007/s40684-020-00302-7.

[16] Z. C. Cordero, D. H. Siddel, W. H. Peter, and A. M. Elliott, "Strengthening of ferrous binder jet 3D printed components through bronze infiltration," *Addit Manuf*, vol. 15, pp. 87–92, 2017, doi: 10.1016/j.addma.2017.03.011.

[17] Y. Wang and Y. F. Zhao, "Investigation of sintering shrinkage in binder jetting additive manufacturing process," *Procedia Manuf*, vol. 10, pp. 779–790, 2017, doi: 10.1016/j.promfg.2017.07.077.

[18] Y. Bai, C. Wall, H. Pham, A. Esker, and C. B. Williams, "Characterizing binder-powder interaction in binder jetting additive manufacturing via sessile drop goniometry," *Journal of Manufacturing Science and Engineering, Transactions of the ASME*, vol. 141, no. 1, p. 011005, 2019, doi: 10.1115/1.4041624.

[19] International ASTM, "ASTM F2792: Standard Terminology for Additive Manufacturing Technologies," *Book of Standard Volumes*, vol. 10, no. 04, pp. 1–3.

[20] P. F. Blazdell and J. R. G. Evans, "Application of a continuous ink jet printer to solid freeforming of ceramics."

[21] H. Kipphan, *Handbook of Print Media: Technologies and Production Methods*, vol. 13, no. 6. 2001. doi: 10.1007/978-3-540-29900-4.

[22] S. Claire, "The Top Binder Jetting Solutions," *3DNatives*, Dec. 2022.

[23] R. K. Holman, M. J. Cima, S. A. Uhland, and E. Sachs, "Spreading and infiltration of inkjet-printed polymer solution droplets on a porous substrate," *J Colloid Interface Sci*, vol. 249, no. 2, pp. 432–440, 2002, doi: 10.1006/jcis.2002.8225.

[24] F. Dini, S. A. Ghaffari, J. Jafar, R. Hamidreza, and S. Marjan, "A review of binder jet process parameters; powder, binder, printing and sintering condition," *Metal Powder Report*, vol. xxx, no. xx, pp. 1–6, 2019, doi: 10.1016/j.mprp.2019.05.001.

[25] T. Do, T. J. Bauder, H. Suen, K. Rego, J. Yeom, and P. Kwon, “Additively manufactured full-density stainless steel 316L with binder jet printing,” in *Proceedings of the ASME 2018 13th International Manufacturing Science and Engineering Conference MSEC2018*, 2018, pp. 1–10. doi: 10.1115/MSEC2018-6681.

[26] P. Kunchala and K. Kappagantula, “3D printing high density ceramics using binder jetting with nanoparticle densifiers,” *Mater Des*, vol. 155, pp. 443–450, Oct. 2018, doi: 10.1016/j.matdes.2018.06.009.

[27] N. B. Crane, J. Wilkes, E. Sachs, and S. M. Allen, “Improving accuracy of powder sintering-based SFF processes by metal deposition from nanoparticle dispersion,” *Rapid Prototyp J*, vol. 12, no. 5, pp. 261–272, 2005, doi: 10.1108/13552540610707022.

[28] G. Hudelson and A. C. Barbati, “Layer spreading and compaction in Binder Jet 3D printing,” 20220355381, Nov. 12, 2021

[29] E. Sachs, G. Hudelson, P. A. Hoisignton, C. B. Renner, K. R. Vaillancourt, and E. R. Moynihan, “Managing powder mobility in Binder Jetting for Additive Manufacturing,” US11.491.716B2, Nov. 08, 2022

[30] D. Gutierrez, M. G. Grau, and M. F. Garcia, “Translating vertices of a model of a 3D printed part,” WO2022/093253A1, May 05, 2022

[31] A. F. Roberts, “Method for compensation for shrinkage and distortion using scans,” US2022/0414904A1, Dec. 29, 2022

[32] P. Yang, T. Nelson, A. Makinde, and D. Robinson, “Hybrid measurement and simulation based distortion compensation system for additive manufacturing,” US202/0245305A1, Jul. 04, 2022

[33] D. Sher, “The year of the binder,” *3D Printing Media Network*, Nov. 02, 2022. https://www.3dprintingmedia.network/the-year-of-the-binder/ (accessed Feb. 20, 2023).

[34] A. Mostafaei, E. L. Stevens, J. J. Ference, D. E. Schmidt, and M. Chmielus, “Binder jetting of a complex-shaped metal partial denture framework,” 2018. [Online]. Available: https://www.sciencedirect.com/science/article/pii/S2214860418300526

[35] S. Mirzababaei and S. Pasebani, “A review on binder jet additive manufacturing of 316L stainless steel,” *Journal of Manufacturing and Materials Processing*, vol. 3, no. 3, p. 82, 2019, doi: 10.3390/jmmp3030082.

[36] D. Sher, “Desktop Health launches cobalt chrome binder jetting for dental labs,” *3D Printing Media Network*, Aug. 16, 2021. https://www.3dprintingmedia.network/cobalt-chrome-binder-jetting-for-dental-labs/ (accessed Feb. 21, 2023).

[37] AMPOWER GmbH & Co. KG., "Binder Jetting - Enabling high volume production," *AMPOWERReport*, Nov. 19, 2019. https://additive-manufacturing-report.com/technology/metal/binder-jetting/ (accessed Feb. 21, 2023).

[38] HP Printing and Computing Solutions S.L., "3D HP Metal Jet S100 printing solution," Oct. 09, 2022. https://www.hp.com/es-es/printers/3d-printers/products/metal-jet.html (accessed Feb. 21, 2023).

[39] P. Henry and L. McKinney, "Desktop Metal begins global shipments of Shop System for mid-volume metal 3D printing manufacturing," *Businesswire*, Nov. 19, 2020. https://www.businesswire.com/news/home/20201119005274/en/Desktop-Metal-Begins-Global-Shipments-of-Shop-System-for-Mid-Volume-Metal-3D-Printing-Manufacturing (accessed Feb. 21, 2023).

[40] T. Mühler, C. M. Gomes, J. Heinrich, and J. Günster, "Slurry-based additive manufacturing of ceramics," *Int J Appl Ceram Technol*, vol. 12, no. 1, pp. 18–25, 2015, doi: 10.1111/ijac.12113.

[41] A. B. Spierings, M. Voegtlin, T. Bauer, and K. Wegener, "Powder flowability characterisation methodology for powder-bed-based metal additive manufacturing," *Progress in Additive Manufacturing*, vol. 1, no. 1–2, pp. 9–20, 2016, doi: 10.1007/s40964-015-0001-4.

[42] A. T. Sutton, C. S. Kriewall, M. C. Leu, and J. W. Newkirk, "Powders for additive manufacturing processes: characterization techniques and effects on part properties," in *27th Annual International Freeform Fabrication Symposium*, 2016, pp. 1004–1030.

[43] H. Miyanaji, N. Momenzadeh, and L. Yang, "Effect of powder characteristics on parts fabricated via binder jetting process," *Rapid Prototyp J*, vol. 25, no. 2, pp. 332–342, 2018, doi: 10.1108/RPJ-03-2018-0069.

[44] A. B. Spierings, N. Herres, and G. Levy, "Influence of the particle size distribution on surface quality and mechanical properties in AM steel parts," *Rapid Prototyp J*, vol. 17, no. 3, pp. 195–202, 2011, doi: 10.1108/13552541111124770.

[45] K. Kassym and A. Perveen, "Atomization processes of metal powders for 3D printing," *Mater Today Proc*, vol. 26, pp. 1727–1733, 2019, doi: 10.1016/j.matpr.2020.02.364.

[46] A. Mostafaei, J. Toman, E. L. Stevens, E. T. Hughes, Y. L. Krimer, and M. Chmielus, "Microstructural evolution and mechanical properties of differently heat-treated binder jet printed samples from gas- and water-atomized alloy 625 powders," *Acta Mater*, vol. 124, pp. 280–289, 2017, doi: 10.1016/j.actamat.2016.11.021.

[47] I. Rishmawi, M. Salarian, and M. Vlasea, "Tailoring green and sintered density of pure iron parts using binder jetting additive manufacturing," *Addit Manuf*, vol. 24, pp. 508–520, 2018, doi: 10.1016/j.addma.2018.10.015.

[48] A. Mostafaei, P. Rodriguez De Vecchis, I. Nettleship, and M. Chmielus, "Effect of powder size distribution on densification and microstructural evolution of

binder-jet 3D-printed alloy 625," *Mater Des*, vol. 162, pp. 375–383, 2019, doi: 10.1016/j.matdes.2018.11.051.

[49] R. Bjørk, V. Tikare, H. L. Frandsen, and N. Pryds, "The effect of particle size distributions on the microstructural evolution during sintering," *Journal of the American Ceramic Society*, vol. 96, no. 1, pp. 103–110, 2013, doi: 10.1111/jace.12100.

[50] S. Mirzababaei, B. K. Paul, and S. Pasebani, "Metal Powder Recyclability in Binder Jet Additive Manufacturing," *JOM*, vol. 72, pp. 3070–3079, 2020, doi: 10.1007/s11837-020-04258-6.

[51] X. Ye, Y. Li, Y. Ai, and Y. Nie, "Novel powder packing theory with bimodal particle size distribution-application in superalloy," *Advanced Powder Technology*, vol. 29, no. 9, pp. 2280–2287, 2018, doi: 10.1016/j.apt.2018.06.012.

[52] Y. Bai, G. Wagner, and C. B. Williams, "Effect of particle size distribution on powder packing and sintering in binder jetting additive manufacturing of metals," *J Manuf Sci Eng*, vol. 139, no. 8, pp. 1–6, 2017, doi: 10.1115/1.4036640.

[53] M. Lanzetta and E. Sachs, "Improved Surface Finish in 3D Printing Using Bimodal Powder Distribution," *Rapid Prototyp J*, vol. 9, no. 3, pp. 157–166, 2003, doi: 10.1108/13552540310477463.

[54] ASTM_International, "ASTM F3049-14: Standard guide for characterizing properties of metal powders used for additive manufacturing processes," *ASTM_International*, 2014.

[55] G. Xu *et al.*, "Investigation on characterization of powder flowability using different testing methods," *Exp Therm Fluid Sci*, vol. 92, pp. 390–401, 2018, doi: 10.1016/j.expthermflusci.2017.11.008.

[56] L. I. Escano *et al.*, "Revealing particle-scale powder spreading dynamics in powder-bed-based additive manufacturing process by high-speed x-ray imaging," *Sci Rep*, vol. 8, no. 1, pp. 1–11, 2018, doi: 10.1038/s41598-018-33376-0.

[57] L. I. Escano *et al.*, "An instrument for in situ characterization of powder spreading dynamics in powder-bed-based additive manufacturing processes," *Review of Scientific Instruments*, vol. 93, no. 4, p. 043707, Apr. 2022, doi: 10.1063/5.0076235.

[58] A. Butscher *et al.*, "Printability of calcium phosphate powders for three-dimensional printing of tissue engineering scaffolds," *Acta Biomater*, vol. 8, no. 1, pp. 373–385, 2012, doi: 10.1016/j.actbio.2011.08.027.

[59] C. Meier, R. Weissbach, J. Weinberg, W. A. Wall, and A. John Hart, "Modeling and characterization of cohesion in fine metal powders with a focus on additive manufacturing process simulations," *Powder Technol*, vol. 343, pp. 855–866, 2019, doi: 10.1016/j.powtec.2018.11.072.

[60] E. Klar and P. K. Samal, *Powder Metallurgy Stainless Steels Applications*. 2018. doi: 10.31399/asm.hb.v07.a0006098.

[61] R. Frykholm, Y. Takeda, B. G. Andersson, and R. Carlstrom, "Solid state sintered 3-D printing component by using inkjet (binder) method," *Journal of the Japan Society of Powder and Powder Metallurgy*, vol. 63, no. 7, pp. 421–426, 2016, doi: 10.2497/jjspm.63.421.

[62] J. Demo, Ed., *Structure, Constitution, and General Characteristics of Wrought Ferritic Stainless Steels*. 100 Barr Harbor Drive, PO Box C700, West Conshohocken, PA 19428-2959: ASTM International, 1977. doi: 10.1520/STP619-EB.

[63] D. N. Wasnik, G. K. Dey, V. Kain, and I. Samajdar, "Precipitation stages in a 316L austenitic stainless steel," *Scr Mater*, vol. 49, no. 2, pp. 135–141, 2003, doi: 10.1016/S1359-6462(03)00220-3.

[64] K. Zissel, E. Bernardo Quejido, T. Deckers, P. Forêt, and E. Hryha, "Binder Jetting-Reusability of 17-4 PH Stainless Steel Powder," in *WorldPM2022*, Lyon: EuroPM, Oct. 2022.

[65] P. Nandwana, A. M. Elliott, D. Siddel, A. Merriman, W. H. Peter, and S. S. Babu, "Powder bed binder jet 3D printing of Inconel 718: Densification, microstructural evolution and challenges," *Curr Opin Solid State Mater Sci*, vol. 21, no. 4, pp. 207–218, 2017, doi: 10.1016/j.cossms.2016.12.002.

[66] J. O. Marston, S. T. Thoroddsen, W. K. Ng, and R. B. H. Tan, "Experimental study of liquid drop impact onto a powder surface," *Powder Technol*, vol. 203, no. 2, pp. 223–236, 2010, doi: 10.1016/j.powtec.2010.05.012.

[67] N. D. Parab *et al.*, "Real time observation of binder jetting printing process using high-speed X-ray imaging," *Sci Rep*, vol. 9, no. 1, pp. 1–10, 2019, doi: 10.1038/s41598-019-38862-7.

[68] A. L. Mundozah, J. J. Cartwright, C. C. Tridon, M. J. Hounslow, and A. D. Salman, "Hydrophobic/hydrophilic static powder beds: Competing horizontal spreading and vertical imbibition mechanisms of a single droplet," *Powder Technol*, vol. 330, pp. 275–283, May 2018, doi: 10.1016/j.powtec.2018.02.032.

[69] M. Lanzetta and E. M. Sachs, "The line formation with alumina powders in drop on demand three dimensional printing," *Proceedings of the 1st International Seminar on: Progress in Innovative Manufacturing Engineering (PRIME 2001)*, vol. 1, pp. 189–196, 2001, doi: 10.1049/iet-sen.2007.0125.

[70] H. Tan, "Three-dimensional simulation of micrometer-sized droplet impact and penetration into the powder bed," *Chem Eng Sci*, vol. 153, pp. 93–107, 2016, doi: 10.1016/j.ces.2016.07.015.

[71] B. D. Cox, "US Patent. Pneumatic Powder Transport System," 2007

[72] K. E. Swier, S. Ringwaid, K. Hulick, and G. Ozturk, "US Patent. Moving Powder in a 3D Printing System," 2020

[73] E. M. Sachs and M. Zero, "US Patent. Metering Build Material in Three-Dimensional (3D) Printing Using a Tool," 2018

[74] G. Jacob, C. U. Brown, and A. Donmez, “The influence of spreading metal powders with different particle size distributions on the powder bed density in laser-based powder bed fusion processes,” 2018. doi: 10.6028/NIST.AMS.100-17.

[75] S. Cao, Y. Qiu, X. F. Wei, and H. H. Zhang, “Experimental and theoretical investigation on ultra-thin powder layering in three dimensional printing (3DP) by a novel double-smoothing mechanism,” *J Mater Process Technol*, vol. 220, pp. 231–242, 2015, doi: 10.1016/j.jmatprotec.2015.01.016.

[76] H. Chen, Q. Wei, Y. Zhang, F. Chen, Y. Shi, and W. Yan, “Powder-spreading mechanisms in powder-bed-based additive manufacturing: Experiments and computational modeling,” *Acta Mater*, vol. 179, pp. 158–171, 2019, doi: 10.1016/j.actamat.2019.08.030.

[77] E. M. Sachs, “US Patent. Powder Dispensing Apparatus Using Vibration,” 2000

[78] S. Shrestha and G. Manogharan, “Optimization of Binder Jetting Using Taguchi Method,” *Jom*, vol. 69, no. 3, pp. 491–497, 2017, doi: 10.1007/s11837-016-2231-4.

[79] H. Miyanaji, “Binder jetting additive manufacturing process fundamentals and the resultant influences on part quality,” University of Louisville, 2018.

[80] L. Sang-Joon, “Powder layer generation for three dimensional printing,” Master’s Thesis, Massachusetts Institute of Technology, 1992.

[81] W. Nan and M. Ghadiri, “Numerical simulation of powder flow during spreading in additive manufacturing,” *Powder Technol*, vol. 342, pp. 801–807, 2019, doi: 10.1016/j.powtec.2018.10.056.

[82] S. Haeri, Y. Wang, O. Ghita, and J. Sun, “Discrete element simulation and experimental study of powder spreading process in additive manufacturing,” *Powder Technol*, vol. 306, pp. 45–54, 2017, doi: 10.1016/j.powtec.2016.11.002.

[83] C. Meier, R. Weissbach, J. Weinberg, W. A. Wall, and A. J. Hart, “Critical influences of particle size and adhesion on the powder layer uniformity in metal additive manufacturing,” *J Mater Process Technol*, vol. 266, pp. 484–501, 2019, doi: 10.1016/j.jmatprotec.2018.10.037.

[84] A. Lores, N. Azurmendi, I. Agote, and E. Zuza, “A review on recent developments in binder jetting metal additive manufacturing: materials and process characteristics,” *Powder Metallurgy*, vol. 62, no. 5, pp. 267–296, Oct. 2019, doi: 10.1080/00325899.2019.1669299.

[85] M. Vaezi and C. K. Chua, “Effects of layer thickness and binder saturation level parameters on 3D printing process,” *International Journal of Advanced Manufacturing Technology*, vol. 53, no. 1, pp. 275–284, 2011, doi: 10.1007/s00170-010-2821-1.

[86] E. Sheydaeian, Z. Fishman, M. Vlasea, and E. Toyserkani, “On the effect of throughout layer thickness variation on properties of additively manufactured

cellular titanium structures," *Addit Manuf*, vol. 18, pp. 40–47, 2017, doi: 10.1016/j.addma.2017.08.017.

[87] M. Doyle, K. Agarwal, W. Sealy, and K. Schull, "Effect of Layer Thickness and Orientation on Mechanical Behavior of Binder Jet Stainless Steel 420 + Bronze Parts," *Procedia Manuf*, vol. 1, pp. 251–262, 2015, doi: 10.1016/j.promfg.2015.09.016.

[88] R. K. Enneti and K. C. Prough, "Effect of binder saturation and powder layer thickness on the green strength of the binder jet 3D printing (BJ3DP) WC-12%Co powders," *Int J Refract Metals Hard Mater*, vol. 84, no. April, p. 104991, 2019, doi: 10.1016/j.ijrmhm.2019.104991.

[89] H. Chen and Y. F. Zhao, "Process parameters optimization for improving surface quality and manufacturing accuracy of binder jetting additive manufacturing process," *Rapid Prototyp J*, vol. 22, no. 3, pp. 527–538, 2016, doi: 10.1108/RPJ-11-2014-0149.

[90] A. Farzadi, V. Waran, M. Solati-Hashjin, Z. A. A. Rahman, M. Asadi, and N. A. A. Osman, "Effect of layer printing delay on mechanical properties and dimensional accuracy of 3D printed porous prototypes in bone tissue engineering," *Ceram Int*, vol. 41, no. 7, pp. 8320–8330, 2015, doi: 10.1016/j.ceramint.2015.03.004.

[91] M. Kafara, J. Kemnitzer, H. H. Westermann, and R. Steinhilper, "Influence of Binder Quantity on Dimensional Accuracy and Resilience in 3D-Printing," *Procedia Manuf*, vol. 21, no. 2017, pp. 638–646, 2018, doi: 10.1016/j.promfg.2018.02.166.

[92] H. Miyanaji and L. Yang, "Equilibrium saturation in binder jetting additive manufacturing processes: theoretical model vs. experimental observations," in *27th Annual International Freeform Fabrication Symposium*, 2016, pp. 1945–1959.

[93] H. Miyanaji, S. Zhang, and L. Yang, "A new physics-based model for equilibrium saturation determination in binder jetting additive manufacturing process," *Int J Mach Tools Manuf*, vol. 124, no. September 2017, pp. 1–11, 2018, doi: 10.1016/j.ijmachtools.2017.09.001.

[94] T. Colton, J. Liechty, A. Mclean, and N. Crane, "Influence of drop velocity and droplet spacing on the equilibrium saturation level in binder jetting," in *30th Annual International Freeform Fabrication Symposium*, 2019, pp. 99–108.

[95] J.-W. Oh, S. Nahm, B. Kim, and H. Choi, "Anisotropy in green body bending strength due to additive direction in the binder-jetting additive manufacturing process," *Korean Journal of Metals and Materials*, vol. 57, no. 4, pp. 227–235, 2019, doi: 10.3365/KJMM.2019.57.4.227.

[96] H. Miyanaji, N. Momenzadeh, and L. Yang, "Effect of printing speed on quality of printed parts in binder jetting process," *Addit Manuf*, vol. 20, pp. 1–10, 2018, doi: 10.1016/j.addma.2017.12.008.

[97] A. Mostafaei, A. M. Elliott, J. E. Barnes, C. L. Cramer, P. Nandwana, and M. Chmielus, “Binder jet 3D printing - process parameters, materials, properties, and challenges,” *Prog Mater Sci*, p. 100684, 2020, doi: 10.1016/j.pmatsci.2020.100684.

[98] M. Ziaee, E. M. Tridas, and N. B. Crane, “Binder-jet printing of fine stainless steel powder with varied final density,” *Jom*, vol. 69, no. 3, pp. 592–596, 2017, doi: 10.1007/s11837-016-2177-6.

[99] H. Nguyen, N. Adrian, J. L. Xin Yan, J. M. Salfity, W. Allen, and Q. C. Pham, “Development of a Robotic System for Automated Decaking of 3D-Printed Parts,” *Proc IEEE Int Conf Robot Autom*, no. i, pp. 8202–8208, 2020, doi: 10.1109/ICRA40945.2020.9197110.

[100] Y. Wu, R. M. German, D. Blaine, B. Marx, and C. Schlaefer, “Effects of residual carbon content on sintering shrinkage, microstructure and mechanical properties of injection molded 17-4 PH stainless steel,” *J Mater Sci*, vol. 37, no. 17, pp. 3573–3583, 2002, doi: 10.1023/A:1016532418920.

[101] B. Levenfeld, A. Várez, and J. M. Torralba, “Effect of residual carbon on the sintering process of M2 high speed steel parts obtained by a modified metal injection molding process,” *Metall Mater Trans A Phys Metall Mater Sci*, vol. 33, no. 6, pp. 1843–1851, 2002, doi: 10.1007/s11661-002-0192-4.

[102] B. Verlee, T. Dormal, and J. Lecomte-Beckers, “Density and porosity control of sintered 316l stainless steel parts produced by additive manufacturing,” *Powder Metallurgy*, vol. 55, no. 4, pp. 260–267, 2012, doi: 10.1179/0032589912Z.00000000082.

[103] T. Do, P. Kwon, and C. S. Shin, “Process development toward full-density stainless steel parts with binder jetting printing,” *Int J Mach Tools Manuf*, vol. 121, pp. 50–60, 2017, doi: 10.1016/j.ijmachtools.2017.04.006.

[104] H.-L. Juan, “Effect of temperature ratio (Ts/Tm) and time on the sintering behavior of metallic 316L stainless steel coupons produced using jet-binder technology,” Master’s Thesis, University of Pittsburgh, 2017.

[105] H. J. Hsu, S. Y. Lee, S. L. Chang, C. H. Lo, and Y. M. Lin, “Shrinkage prediction using finite element analysis and experimental validation using three-dimension slurry printing system,” *International Journal of Advanced Manufacturing Technology*, vol. 91, no. 1–4, pp. 1289–1296, 2017, doi: 10.1007/s00170-016-9842-3.

[106] N. Raghunath and P. M. Pandey, “Improving accuracy through shrinkage modelling by using Taguchi method in selective laser sintering,” *Int J Mach Tools Manuf*, vol. 47, no. 6, pp. 985–995, 2007, doi: 10.1016/j.ijmachtools.2006.07.001.

[107] C. Schmutzler, T. H. Stiehl, and M. F. Zaeh, “Empirical process model for shrinkage-induced warpage in 3D printing,” *Rapid Prototyp J*, vol. 25, no. 4, pp. 721–727, 2019, doi: 10.1108/RPJ-04-2018-0098.

[108] S. L. Lu, G. K. Meenashisundaram, P. Wang, S. M. L. Nai, and J. Wei, "The combined influence of elevated pre-sintering and subsequent bronze infiltration on the microstructures and mechanical properties of 420 stainless steel additively manufactured via binder jet printing," *Addit Manuf*, vol. 34, no. April, 2020, doi: 10.1016/j.addma.2020.101266.

[109] Y. Zhu, Z. Wu, W. D. Hartley, J. M. Sietins, C. B. Williams, and H. Z. Yu, "Unraveling pore evolution in post-processing of binder jetting materials: X-ray computed tomography, computer vision, and machine learning," *Addit Manuf*, vol. 34, no. May, p. 101183, 2020, doi: 10.1016/j.addma.2020.101183.

[110] K. Kimes, K. Myers, A. Klein, M. Ahlfors, E. Stevens, and M. Chmielus, "Binder Jet 3D Printing of 316L Stainless Steel: Effects of HIP on Fatigue," *Microscopy and Microanalysis*, vol. 25, no. S2, pp. 2600–2601, 2019, doi: 10.1017/s1431927619013734.

[111] A. Yegyan, J. Wang, Y. Bai, S. T. Huxtable, and C. B. Williams, "Impacts of process-induced porosity on material properties of copper made by binder jetting additive manufacturing," *Mater Des*, vol. 182, no. 108001, 2019, doi: 10.1016/j.matdes.2019.108001.

[112] H.-G. Min, D.-J. Kang, and J.-H. Park, "Comparison of Tensile and Fatigue Properties of Copper Thin Film Depending on Process Method," *Applied Sciences*, vol. 10, no. 1, p. 388, Jan. 2020, doi: 10.3390/app10010388.

[113] V. Sufiiarov, I. Polozov, A. Kantykov, and A. Khaidorov, "Binder jetting additive manufacturing of 420 stainless steel: Densification during sintering and effect of heat treatment on microstructure and hardness," *Mater Today Proc*, no. xxxx, 2020, doi: 10.1016/j.matpr.2020.01.144.

[114] P. D. Enrique, E. Marzbanrad, Y. Mahmoodkhani, Z. Jiao, E. Toyserkani, and N. Y. Zhou, "Surface modification of binder-jet additive manufactured Inconel 625 via electrospark deposition," *Surf Coat Technol*, vol. 362, no. November 2018, pp. 141–149, 2019, doi: 10.1016/j.surfcoat.2019.01.108.

[115] F. Zanini, E. Sbettega, and S. Carmignato, "X-ray computed tomography for metal additive manufacturing: Challenges and solutions for accuracy enhancement," *Procedia CIRP*, vol. 75, pp. 114–118, 2018, doi: 10.1016/j.procir.2018.04.050.

[116] F. Bernier, R. Tahara, and M. Gendron, "Additive manufacturing powder feedstock characterization using X-ray tomography," *Metal Powder Report*, vol. 73, no. 3, pp. 158–162, 2018, doi: 10.1016/j.mprp.2018.01.002.

[117] A. Thompson, I. Maskery, and R. K. Leach, "X-ray computed tomography for additive manufacturing: A review," *Meas Sci Technol*, vol. 27, no. 7, p. 072001, 2016, doi: 10.1088/0957-0233/27/7/072001.

[118] A. du Plessis, I. Yadroitsava, and I. Yadroitsev, "Effects of defects on mechanical properties in metal additive manufacturing: A review focusing on X-ray tomography insights," *Mater Des*, vol. 187, p. 108385, 2020, doi: 10.1016/j.matdes.2019.108385.

[119] G. Ziółkowski, E. Chlebus, P. Szymczyk, and J. Kurzac, “Application of X-ray CT method for discontinuity and porosity detection in 316L stainless steel parts produced with SLM technology,” *Archives of Civil and Mechanical Engineering*, vol. 14, no. 4, pp. 608–614, 2014, doi: 10.1016/j.acme.2014.02.003.

[120] P. Sperling, N. Achilles, T. Kuhnt, L. Reineke, and B. Barthel, “Evaluation Of Porosity In Metal Binder Jetting Due To Binder Application By Using X-ray CT,” in *WorldPM2022*, Lyon: EuroPM, Oct. 2022.

[121] A. Thompson, N. Senin, I. Maskery, and R. Leach, “Effects of magnification and sampling resolution in X-ray computed tomography for the measurement of additively manufactured metal surfaces,” *Precis Eng*, vol. 53, pp. 54–64, 2018, doi: 10.1016/j.precisioneng.2018.02.014.

[122] F. Zanini, L. Pagani, E. Savio, and S. Carmignato, “Characterisation of additively manufactured metal surfaces by means of X-ray computed tomography and generalised surface texture parameters,” *CIRP Ann Manuf Technol*, vol. 68, no. 1, pp. 515–518, 2019, doi: 10.1016/j.cirp.2019.04.074.

[123] G. Chen *et al.*, “A pore morphological study of gas-atomized Ti-6Al-4V powders by scanning electron microscopy and synchrotron X-ray computed tomography,” *Powder Technol*, vol. 330, pp. 425–430, 2018, doi: 10.1016/j.powtec.2018.02.053.

[124] T. Thiede, T. Mishurova, S. Evsevleev, I. Serrano-Munoz, C. Gollwitzer, and G. Bruno, “3D Shape Analysis of Powder for Laser Beam Melting by Synchrotron X-ray CT,” *Quantum Beam Science*, vol. 3, no. 1, p. 3, 2019, doi: 10.3390/qubs3010003.

[125] J. Villanova *et al.*, “Fast in situ 3D nanoimaging: a new tool for dynamic characterization in materials science,” *Materials Today*, vol. 20, no. 7, pp. 354–359, 2017, doi: 10.1016/j.mattod.2017.06.001.

[126] T. Leißner *et al.*, “3D ex-situ and in-situ X-ray CT process studies in particle technology – A perspective,” *Advanced Powder Technology*, vol. 31, no. 1, pp. 78–86, 2020, doi: 10.1016/j.apt.2019.09.038.

[127] O. Lame, D. Bellet, M. di Michiel, and D. Bouvard, “In situ microtomography investigation of metal powder compacts during sintering,” *Nucl Instrum Methods Phys Res B*, vol. 200, pp. 287–294, 2003, doi: 10.1016/S0168-583X(02)01690-7.

[128] T. Colton and N. B. Crane, “Influence of droplet velocity , spacing , and inter-arrival time on line formation and saturation in binder jet additive manufacturing,” *Addit Manuf*, no. July, p. 101711, 2020, doi: 10.1016/j.addma.2020.101711.

[129] E. Wheat, M. Vlasea, J. Hinebaugh, and C. Metcalfe, “Sinter structure analysis of titanium structures fabricated via binder jetting additive manufacturing,” *Mater Des*, vol. 156, pp. 167–183, Oct. 2018, doi: 10.1016/j.matdes.2018.06.038.

[130] W. Conshohocken, “Standard Test Method for Green Strength for Compacted Metal Powder Specimens 1,” vol. 96, no. Reapproved, pp. 12–14, 2002, doi: 10.1520/B0312-14.2.

[131] ASTM International, "Standard Test Methods for Density of Compacted or Sintered Powder Metallurgy (PM) Products Using Archimedes' Principle," *Astm B962-13*, vol. i, pp. 1–7, 2013, doi: 10.1520/B0962-17.2.

[132] R. Haynes, *Optical Microscopy of Materials*. Boston, MA: Springer US, 1984. doi: 10.1007/978-1-4757-6085-9.

[133] L. Reimer, *Scanning Electron Microscopy: Physics of Image Formation and Microanalysis*, Second., vol. 45. Springer, 1998.

[134] S. Carmignato, *Industrial X-Ray Computed Tomography*.

[135] C. M. Shakarji, V. Srinivasan, V. D. Lee, M. Shilling, and B. Muralikrishnan, "Standards for Evaluating the Influence of Materials on the Performance of X-Ray Computed Tomography in Measuring Geometric Variability," in *Volume 2B: Advanced Manufacturing*, American Society of Mechanical Engineers, Nov. 2020. doi: 10.1115/IMECE2020-24651.

[136] J. Sauvola, T. Seppanen, S. Haapakoski, and M. Pietikainen, "Adaptive document binarization," in *Proceedings of the International Conference on Document Analysis and Recognition, ICDAR*, IEEE, 1997, pp. 147–152. doi: 10.1109/icdar.1997.619831.

[137] S. Bugani, M. Camaiti, L. Morselli, E. Van De Casteele, and K. Janssens, "Investigating morphological changes in treated vs. untreated stone building materials by x-ray micro-CT," in *Analytical and Bioanalytical Chemistry*, Jun. 2008, pp. 1343–1350. doi: 10.1007/s00216-008-1946-7.

[138] E. S. Erdogan and O. Eksi, "Prediction of wall thickness distribution in simple thermoforming moulds," *Strojniski Vestnik/Journal of Mechanical Engineering*, vol. 60, no. 3, pp. 195–202, 2014, doi: 10.5545/sv-jme.2013.1486.

[139] VolumeGraphics, "Spheres and Rays: Wall Thickness Analysis," *Spheres and Rays: Wall Thickness Analysis*, Apr. 03, 2022. https://www.volumegraphics.com/en/stories/spheres-and-rays-wall-thickness-analysis.html (accessed Nov. 20, 2021).

[140] E. Maire, "X-ray tomography applied to the characterization of highly porous materials," *Annual Review of Materials Research*, vol. 42. pp. 163–178, Aug. 2012. doi: 10.1146/annurev-matsci-070511-155106.

[141] R. Varshney and M. Verma, "A Review on Machine Learning Tasks , Algorithms and its Application in Image Processing," pp. 1596–1602, 2018, [Online]. Available: http://ijamtes.org/

[142] D. Sage and M. Unser, "Easy Java Programming for Teaching Image-Processing," in *IEEE International Conference on Image Processing*, 2001.

[143] R. C. Gonzalez and R. E. Woods, *Digital Image Processing, 4e*.

[144] J.-K. Kamarainen, "Gabor Features in Image Analysis," in *International Conference on Image Analysis*, 2012.

[145] J. Yan *et al.*, “LightGBM: accelerated genomically designed crop breeding through ensemble learning,” *Genome Biol*, vol. 22, no. 1, Dec. 2021, doi: 10.1186/s13059-021-02492-y.

[146] G. Ke *et al.*, “LightGBM: A Highly Efficient Gradient Boosting Decision Tree.” [Online]. Available: https://github.com/Microsoft/LightGBM.

[147] N. Lecis *et al.*, “Effects of process parameters, debinding and sintering on the microstructure of 316L stainless steel produced by binder jetting,” *Materials Science and Engineering A*, vol. 828, Nov. 2021, doi: 10.1016/j.msea.2021.142108.

[148] F. Subirada, J. M. Garcia, and S. Garcia Reyerp, “Method and apparatus for assessing nozzle health,” 2010

[149] A. L. Petsiuk and J. M. Pearce, “Open source computer vision-based layer-wise 3D printing analysis,” *Addit Manuf*, vol. 36, p. 101473, Dec. 2020, doi: 10.1016/j.addma.2020.101473.

[150] K. Paraskevoudis, P. Karayannis, and E. P. Koumoulos, “Real-time 3d printing remote defect detection (Stringing) with computer vision and artificial intelligence,” *Processes*, vol. 8, no. 11, pp. 1–15, Nov. 2020, doi: 10.3390/pr8111464.

[151] G. Damioli, V. Van Roy, and D. Vertesy, “The impact of artificial intelligence on labor productivity,” *Eurasian Business Review*, vol. 11, no. 1, Mar. 2021, doi: 10.1007/s40821-020-00172-8.

[152] E. O. Pyzer-Knapp *et al.*, “Accelerating materials discovery using artificial intelligence, high performance computing and robotics,” *NPJ Comput Mater*, vol. 8, no. 1, Dec. 2022, doi: 10.1038/s41524-022-00765-z.

[153] ArcelorMittal Deutschland, “ArcelorMittal Hamburg: Artificial intelligence optimizes wire rod production ,” Dec. 01, 2022.

[154] M. Amirjan, H. Khorsand, M. H. Siadati, and R. Eslami Farsani, “Artificial Neural Network prediction of Cu-Al2O3 composite properties prepared by powder metallurgy method,” *Journal of Materials Research and Technology*, vol. 2, no. 4, pp. 351–355, 2013, doi: 10.1016/j.jmrt.2013.08.001.

[155] S. Sahoo, A. Pare, S. Mishra, S. Soren, and S. K. Biswal, “Prediction of Sinter Properties Using a Hyper-Parameter-Tuned Artificial Neural Network,” *ACS Omega*, Apr. 2022, doi: 10.1021/acsomega.2c05980.